2012

UNDERSTANDING DEGRADATION AND LITHIUM DIFFUSION IN LITHIUM ION BATTERY ELECTRODES

Juchuan Li
University of Kentucky, juchuanli@gmail.com

STUDENT AGREEMENT:

I represent that my thesis or dissertation and abstract are my original work. Proper attribution has been given to all outside sources. I understand that I am solely responsible for obtaining any needed copyright permissions. I have obtained and attached hereto needed written permission statements(s) from the owner(s) of each third-party copyrighted matter to be included in my work, allowing electronic distribution (if such use is not permitted by the fair use doctrine).

I hereby grant to The University of Kentucky and its agents the non-exclusive license to archive and make accessible my work in whole or in part in all forms of media, now or hereafter known. I agree that the document mentioned above may be made available immediately for worldwide access unless a preapproved embargo applies.

I retain all other ownership rights to the copyright of my work. I also retain the right to use in future works (such as articles or books) all or part of my work. I understand that I am free to register the copyright to my work.

REVIEW, APPROVAL AND ACCEPTANCE

The document mentioned above has been reviewed and accepted by the student's advisor, on behalf of the advisory committee, and by the Director of Graduate Studies (DGS), on behalf of the program; we verify that this is the final, approved version of the student's dissertation including all changes required by the advisory committee. The undersigned agree to abide by the statements above.

Juchuan Li, Student

Dr. Yang-Tse Cheng, Major Professor

Dr. Fuqian Yang, Director of Graduate Studies

UNDERSTANDING DEGRADATION AND LITHIUM DIFFUSION IN LITHIUM ION BATTERY ELECTRODES

DISSERTATION

A dissertation submitted in partial fulfillment of the
requirements for the degree of Doctor of Philosophy in the
College of Engineering
at the University of Kentucky

By
Juchuan Li

Lexington, Kentucky

Director: Dr. Yang-Tse Cheng, Professor of Materials Engineering,
University of Kentucky, Lexington, Kentucky

Co-Director: Dr. Fuqian Yang, Professor of Materials Engineering
University of Kentucky, Lexington, Kentucky

2012

ABSTRACT OF DISSERTATION

UNDERSTANDING DEGRADATION AND LITHIUM DIFFUSION IN LITHIUM ION BATTERY ELECTRODES

Lithium-ion batteries with higher capacity and longer cycle life than that available today are required as secondary energy sources for a wide range of emerging applications. In particular, the cycling performance of several candidate materials for lithium-ion battery electrodes is insufficient because of the fast capacity fading and short cycle life, which is mainly a result of mechanical degradation.

This dissertation mainly focuses on the issue of mechanical degradation in advanced lithium-ion battery electrodes. Thin films of tin electrodes were studied where we observed whisker growth as a result of electrochemical cycling. These whiskers bring safety concerns because they may penetrate through the separator, and cause short-circuit of the electrochemical cells. Cracking patterns generated in amorphous silicon thin film electrodes because of electrochemical cycling were observed and analyzed. A two-dimensional spring-block model was proposed to successfully simulate the observed cracking patterns. With semi-quantitative study of the cracking pattern features, two strategies to void cracking in thin-film electrodes were proposed, namely reducing the film thickness and patterning the thin-film electrodes.

We also investigated electrodes consisting of low melting point elements and showed that cracks can be self-healed by the solid-to-liquid phase transformation upon cycling. Using gallium as an example, mechanical degradation as a failure mechanism for lithium-ion battery electrodes can be eliminated.

In order to quantitatively understand the effect of surface modification on electrodes, we analyzed diffusion equations with boundary conditions of finite interfacial reactions, and proposed a modified potentialstatic intermittent titration technique (PITT) as an electro-analytical technique to study diffusion and interfacial kinetics. The modified PITT has been extended to thin-film geometry and spherical geometry, and thus can be

used to study thin-film and composite electrodes consisting of particles as active materials.

KEY WORDS: lithium-ion batteries, mechanical degradation, crack, interfacial kinetics, diffusion

Juchuan Li

03/28/2012

UNDERSTANDING DEGRADATION AND LITHIUM DIFFUSION IN LITHIUM ION BATTERY ELECTRODES

By

Juchuan Li

Dr. Yang-Tse Cheng

Director of Dissertation

Dr. Fuqian Yang

Co-Director of Dissertation

Dr. Fuqian Yang

Director of Graduate Study

Date

Dedicated to my parents

ACKNOWLEDGEMENTS

First, I want to express my deepest acknowledge to my co-advisors, Drs. Yang-Tse Cheng and Fuqian Yang, for their continuous encourage and help during my doctoral research. I enjoyed working with them on multidisciplinary research. Without them, this dissertation would be impossible to finish.

I am also grateful to my committee members, Drs. T. John Balk, Christine Trinkle, Adam Timmons (Chrysler), Steve Lipka (CAER), and Tate Tsang for their time, efforts, and suggestions on my research and dissertation.

I would like to thank my lab mates, especially Rutooj D. Deshpande, Ilona Hoffmann, Yunchao Li, Qinglin Zhang, Jie Pan, Jiagang Xu, Rong Chen, and Guangfeng Zhao, for their support and help on my research. We have made our Ph.D. lives fun and productive.

Researchers at GM R&D are greatly appreciated, including Drs. Mark W. Verbrugge, Xingcheng Xiao, Steve Harris, Yan Wu, and Meng Jiang for their guidance and support given to me. I am also grateful to GM for giving me summer internships and visiting scientist status.

I would also like to thank people who helped my research: Dr. Qingliu Wu, Dr. Alan K. Dozier, Lei Wang, Brian Wajdyk (CeNSE), Nancy Miller, and Dr. Jia Ye (Microscopy Center). Co-authors of my publications at Department of Chemistry are gratefully thanked: Aman Kaur, Dr. mark Meier, Rituraj Borgohain, and Dr. John Selegue.

Thanks to the funding agencies which supported this dissertation: NSF, GM R&D, and UK.

Finally, I would like to thank my parents for their unselfish support.

TABLE OF CONTENTS

LIST OF TABLES

LIST OF FIGURES

Chapter 1. Introduction

Since the commercialization in early 1990s by Sony, Lithium-ion batteries (LIBs) have been widely used in modern society as portable energy sources due to their high operation voltage, high energy and power densities, and stable cycling performance. Particularly, LIBs are used to replace other secondary batteries, including nickel-metal hydride batteries, lead-acid batteries, and alkaline batteries, to power electronic devices, medical devices, portable power tools, and more recently, hybrid and pure electric vehicles [1-3].

A typical LIB consists of a positive electrode, a negative electrode, and a porous separator immersed in ionically conducting liquid electrolyte. With the rapid increase of demands, current commercial LIBs are unable to fulfill the energy and power requirements of products, especially hybrid and pure electric vehicles. Thus, advanced electrode materials with higher specific capacities (mAh g^{-1}) and capacity densities (mAh mL^{-1}) are required. Commercially used negative electrode material, graphite, has already reached its theoretical and engineering limits. There are several elements and alloys possible for negative electrodes of LIBs due to their high theoretical capacities, such as silicon (Si), tin (Sn), and germanium (Ge). These advanced negative electrode materials suffer severe volume expansion and contraction upon lithiation and de-lithiation, which leads to cracking and fracture in electrodes, and further leads to loss of electric conduction and capacity fading of the electrodes.

Numerous efforts have been made to avoid mechanical degradation of LIB electrodes upon extended cycling. Naonstructuring the electrodes has been shown to effectively enhance the cycling performance of LIB electrodes. Low stress generated in nanostructured materials during cycling is believed a reason for better cycle life. Alloying the active materials with inactive elements or other active elements is another method to practically extend the life of the electrodes. The inert elements act as buffer components and absorb mechanical deformation. Various types of conducting additives and binders

are developed for LIB electrodes, which can practically enhance the conductivity of electrodes and connect the powders (or particles) upon small volume change.

In this dissertation, we focus on understanding the mechanical degradation of advanced LIB anodes, electrode/electrolyte interfacial kinetics, and diffusion of lithium in electrodes. The purposes of this dissertation include (1) fundamental understanding of the mechanical behavior, especially degradation mechanisms, of LIB electrodes, (2) developing strategies to avoid degradation and cracking of electrodes, and (3) quantitative measuring and understanding lithium diffusion in electrodes and interfacial reaction kinetics.

Chapter 1 gives a brief introduction of the background and the purpose of this dissertation. Chapter 2 provides the literature review of the state-of-art LIB negative electrodes, their failure mechanisms, and possible solutions. Common electrochemical testing procedures for LIB research are also introduced and discussed. Chapter 3 reports an observation of whisker formation in Sn electrodes as a result of electrochemical cycling. Chapter 4 discusses experimental study of cracking pattern formation in thin-film amorphous-Si electrodes during cycling. A simulation tool for cracking patterns is introduced which captures the essential feature of cracking patterns. We also provide strategies to avoid cracking in thin-film LIB electrodes. Chapter 5 shows the concept of using lithium-active liquid metal as self-healing LIB electrodes by an example of liquid gallium (Ga). Mechanical degradation as a failure mechanism of LIB electrodes can be eliminated by solid-to-liquid phase transformation of electrodes. Chapter 6 proposes a modified potential intermittent titration technique (PITT) as an electroanalytical technique which can be used to determine the interfacial reaction rate and diffusion coefficient simultaneously. Chapter 7 extended this modified PITT to composite electrodes where active particles are of spherical geometry. Chapter 8 summarizes this dissertation with an outline of future research opportunities.

Chapter 2 Literature Review

2.1 Working Mechanisms of Lithium-Ion Batteries

A battery consists one or more cells that convert chemical energy into electrical energy. A battery is usually composed of a positive electrode (cathode) and a negative electrode (anode) separated by ionically conducting and electronically insulating electrolyte. The electromotive force of a battery, E, is determined by the Gibbs free energy by

$$\Delta G = -nFE \tag{2.1}$$

where n is the charge number (n=1 for lithium ions) and F is Faraday's constant. A voltage of a cell is determined by the chemical potential difference between the positive and negative electrodes. For LIBs, the voltage of a cell is determined by the difference of chemical potentials of lithium atoms in positive and negative electrodes. Eq. (2.1) gives the theoretical voltage or open circuit voltage (OCV) of a cell.

The positive electrode materials of LIBs are usually layered-type lithium metal oxides (for example, $LiCoO_2$) [4-6], olivine-type lithium metal phosphates or silicates (for example, $LiFePO_4$ and $LiFeSiO_4$) [5, 6], spinel-type lithium metal oxides (for example, $LiMn_2O_4$), or conversion-type alloys. The negative electrode materials of LIBs are usually composed of various types of graphite [7-9], Si [10, 11], Sn [10, 12, 13], Ge [14, 15], TiO_2 [16], or their alloys or composites. During operation, the lithium-ion containing electrolyte transports lithium ions back and forth.

Half cells are usually used for fundamental research of LIB electrodes. The term *half cell* refers to a cell consisting of a single electrode (either positive or negative) as the working electrode (WE) and pure lithium metal as the counter electrode (CE). In this type of cells, CE is also used as reference electrode (RE), whose electrochemical potential does not change and is set to be zero.

2.2 Lithium Ion Battery Negative Electrodes

Since the late 1980s [17], graphite materials have been used as negative electrodes for LIBs. There are different kinds of graphitic electrode materials, such as natural and artificial graphite, mesocarbon microbeads (MCMB), and highly disordered or amorphous carbons [8, 18, 19]. The theoretical specific capacity (charge per unit mass) of graphite is 372 mAh g^{-1} and the theoretical capacity density (charge per unit volume) is 840 mAh mL^{-1}, calculated from the final product of lithiated graphite, LiC_6. The reaction of graphite during lithiation and de-lithiation can be summarized as

$$Li + 6C \leftrightarrow LiC_6 \tag{2.2}$$

The layered structure of graphite naturally provides space to store lithium atoms. As a result, the volume change of graphite upon cycling is less than 10% [8, 19] and the stress is in the order of several hundred MPa [20], one order of magnitude lower than that of alloy electrodes [21, 22]. Thus, commercial electrochemical-grade graphite delivers stable capacity over several hundred cycles due to low volume change and low stress.

Alternative materials for negative materials of LIBs include pure elements, alloys, metal oxides, and composite materials. There are many elements which have much higher specific capacities than graphite. For example, the theoretical specific capacity of Si is 3579 mAh g^{-1} [23], which is the highest among all the elements for negative electrodes except for pure Li metal itself. Figure 2.1 shows selected elements for LIB negative electrodes [24]. These elements react with Li and form alloys where the atomic ratio of Li to the active element can be as large as 4.4. Besides pure elements, some metal oxides react with Li metal, such as TiO_2 [16], NiO, and $Li_4Ti_5O_{12}$ (LTO) [16, 25, 26], and can also be used as negative electrodes.

The reaction mechanisms, electrochemical behavior, and cycling performance of pure element type negative electrodes are similar. Here, we take Si as an example to demonstrate the main issues and obstacles for their applications. Si has attracted significant attention of researchers mainly because of its highest theoretical capacity. It is

reported that during lithiation, Si and Li form alloys including $Li_{12}Si_7$, Li_7Si_3, $Li_{13}Si_4$, and $Li_{17}Si_5$ [23, 27, 28]. It is well accepted that bulk Si hardly delivers useful capacity [11, 29, 30], mainly because of the large volume expansion of Si during cycling which can be as large as 370% [29, 31], as well as the associated large diffusion-induced stress (DIS) [21, 22]. Dahn *et al.* [27] and Obrovac *et al.* [23] have separately reported that crystalline Si undergoes amorphization during lithiation, and keeps amorphous during cycling unless the electrodes are over lithiated [32]. Sn forms $Li_{17}Sn_4$ upon full lithiation [18, 33], which gives a specific capacity of 992 mAh g^{-1}. Similar to Si, the cycle life of bulk Sn is short (i.e., 10 cycles [12]) because of large volume expansion and high DIS [12, 18].

In order to overcome the issue of pulverization and capacity fading of electrodes, different methods have been applied in order to utilize the advanced negative materials. These strategies can be divided into four categories, including reducing the dimensions of active material, alloying the elements with inert or another active components, utilizing conducting components and binders for composite electrodes, and surface modification of electrode materials.

Nanostructuring the electrode materials is an effective way to enhance the reversible capacity and extend the cycle life of LIBs. Various nanostructured electrodes have been reported to deliver improved performance, including thin films [14, 34, 35], nanowires [36], nanoporous structures [37, 38], nano-patterned electrodes [39, 40], and other nano-shaped materials [41, 42]. Most of the nanostructured electrodes showed improved reversible capacity upon extended cycling. For example, Graetz *et al.* showed improved cycling performance of Si thin-films over nano-crystals [35]. Cui *et al.* demonstrated extended cycle life and high capacity of Si nanowires directly grew on stainless steel current collectors [36]. Cho *et al.* compared cycling performance of Si nano particles ranging from several to tens of nanometers, and demonstrated excellent capacity retention using ~5 nm Si nano particles [30]. Xiao *et al.* studied cycling performance of patterned Si, and showed stable capacity over 40 cycles where the average width of the square patch is about 7.6 μm [39]. A low average diffusion-induced stress in patterned electrodes is believed the reason for improved capacity retention [43]. Similar phenomena were

observed on patterned thin-film Sn-Co-C composite electrodes where the pattern size is about 7.5 μm [40]. It is believed that the enhanced performance of nanostructured materials is mainly due to voids which occupy a large portion of nanostructured electrodes, and provide space for volume expansion during lithiation. Cheng *et al.* showed that the stress level and maximum stress in nano-structure materials is lower than that in bulk materials because of surface effects [44, 45]. Also, the power performance (cycling performance under high rates) of nano-structural electrodes is usually good, because the average diffusion distance for lithium is shortened and a large surface area provides sites for interfacial reactions. On the other hand, there are serious drawbacks for nanostructured LIB electrodes. Most importantly, the large surface area of nanostructured materials requires formation of a large amount of solid electrolyte interphase (SEI) upon lithiation, which consumes lithium ions from the lithium-salt-based non-aqueous electrolyte [46-48]. The formation of SEI is largely irreversible and SEI does not decompose readily into lithium ions upon de-lithiation [46, 47]. As a result, the performance of a full cell using nano-structured electrodes will be limited because of limited amount of lithium ions and electrolyte. A majority of previous academic publications are based on results of half-cells, where pure lithium metal is used as the counter electrode and the amount of lithium ions can be considered infinite. Besides SEI, the packing density, capacity and energy densities of nano-structured electrodes are low due to extra space. The cost of nanostructured electrodes is high due to the usually complicated fabrication procedures.

Alloying the active materials with other active or inert materials is another effective way to extend the cycle life of LIBs. For example, various alloys of Si, M_xSi, are produced which show better performance, where M can be Ag [49], Mg [50, 51], Ca [52], carbon [53-55], Zn [56], as well as transition metals such as Co, Fe, Mn, Ni, and Co [57-61]. Metal oxides also delivers improved cycling performance, such as SiO [62, 63], SnO_x [64-69], and GeO [42]. It is believed that the inert components remain unchanged during cycling, and thus the overall stress of the whole electrode is lowered. Furthermore, inert elements can act as “buffer” components which absorb strain energy of the active

components. On the other hand, inert components add mass and volume to the electrodes, and thus lower the specific capacity and capacity density of the electrodes. Usually the first-cycle Columbic efficiency is low due to irreversible reactions of Li and inert elements.

Binders and conducting additives are necessary for commercial LIB electrodes, where the active materials are in the form of powders. For current commercial LIBs using graphite as the negative electrodes and $LiCoO_2$ as the positive electrodes, polyvinylidene fluoride (PVDF) is used as the binder and carbon black is used as the conducting additives. It has been reported that sodium carboxymethyl cellulose (NaCMC) or lithium carboxymethyl cellulose (LiCMC) can be used as the binder for Si and other high capacity composite electrodes with improved capacity retention [70-72]. However, the reason is still a mystery because CMC salts are essentially brittle. Other kinds of conducting additives, such as carbon nanotubes (CNT) [73, 74], have been shown to improve the performance of composite electrodes.

Recently, surface modifications, particularly surface coating of electrode materials, has been shown to improve the performance of LIB electrodes. The coating materials for LIB electrodes are versatile, including carbon [75-77], metals (i.e., Ag, Sn) [78-80], and metal oxides (i.e., Al_2O_3, TiO_2) [81-83] and other ceramics (i.e., AlF_3, LIPON) [84-86]. The mechanisms of surface modification during cycling are not well understood. Usually, it is believed that surface coating has a strong effect on the surface chemistry, morphology, structure, and properties of surface film (SEI for negative electrodes). Further, surface modification may suppress metal dissolution by reacting with residual trace-amounts of HF in the electrolyte. Surface coatings can also change the interfacial kinetics, improve surface conductivity, and act as mechanical protecting layers.

In general, nano-structuring and alloying are effective methods to enhance the capacity retention and cycling performance of LIB electrodes by reducing the stress level during lithiation and de-lithiation. However, efforts have to be made to overcome the issue of large amount of SEI formation and surface attack from the electrolyte due to the

relatively large ratio of surface area to volume. Surface modification is effective in suppressing the formation of SEI by changing surface chemistry. Practically, in order to produce LIB electrodes with high capacity and power density, good cycling performance, and reasonable packing density, multiple strategies mentioned above are needed. For example, Simon *et al.* electrodeposited Sn on current collectors of Cu nano-rods, and showed improved capacity at more than 500 cycles [41]. It was demonstrated that composite electrode consisting of nano sized Sn and C had stable reversible capacity of 500 mAh g^{-1} up to 200 cycles [87, 88]. More recently, Cui *et al.* reported that double wall Si nanotube delivers capacity of more than 1000 mAh g^{-1} after 6000 cycles of charge/discharge [89].

2.3 Electrochemical Techniques for LIB Research

Electrochemical and electroanalytical techniques can provide useful information about thermodynamics and kinetics of electrochemical systems, including equilibrium potential of reactions and types of reactions occurring in electrodes, reaction kinetics, thermodynamics information, and lithium diffusion in electrodes and electrolytes. Typically, electrochemical techniques require static or dynamic control of voltage or current while monitoring the change of both voltage and current. In this section, major electrochemical techniques used in this dissertation, including cyclic voltammetry and galvanostatic cycling, are introduced and discussed.

2.3.1 Cyclic Voltammetry

Cyclic voltammetry (CV) is one of the most commonly used electrochemical techniques to investigate the chemical reaction types, Nernstian (reversible) or non-Nernstian (irreversible) behavior of redox couples, formation potentials, and reaction mechanisms. CV is convenient and efficient in obtaining qualitative information, though it is usually not a good technique for quantitative studies.

In a CV test, the potential of the system is swept linearly towards a peak position, and then returned to the initial value linearly. The procedure can be repeated multiple times.

During the potential sweep, current is monitored by a potentiostat. An illustration of a CV controlling profile is shown in Fig. 2.2 (a).

The result of CV experiments is usually plotted as current vs. applied potential. An example of Sn vs. Li is shown in Fig. 2.2 (b). The information of this CV test include (a) irreversible reactions (the sharp region near 2.0 V, which is a result of reaction between lithium and residual oxygen, moisture, and other impurities in electrolyte), (b) reversible phase transformations (the peaks in Fig. 2.2 (b), which represents phase transformations of Li-Sn alloys with different compositions), and (c) potential of oxidation and reduction reactions (peak potentials).

2.3.2 Galvanostatic Cycling

Galvanostatic cycling is a very important electrochemical technique for LIB research, which provides charging and discharging profiles for LIBs under practical applications. In a galvanostatic cycling test, a cell is charged and discharged galvanostaticly (constant current) between upper and lower voltage limits.

The upper and lower voltage limits are determined by the Gibbs free energy of the electrode materials and their products during lithiation. For alloy-type negative electrodes, the lower limits are practically 10 to 50 mV, and the upper limits are practically 1 to 2 V, depends on the type of alloys. The lower limits are chosen to be higher than 0 V vs. Li/Li^+ because at low potentials lithium tends to deposit on electrode surface, which eventually causes the growth of lithium dendrites, causing safety issues.

The applied current is directly related to the power output of the electrode. Usually "C-rate" is used to define the cycling rate of LIBs, where xC is defined as $1/x$ hours per charge or discharge. Practically C/10 or C/5 is considered slow cycling, though it is non-equilibrium.

There are three ways of plotting the results of galvanostatic cycling, namely potential-capacity profile, differential potential-capacity profile, and cycling performance. Plenty of examples are given in later chapters of this dissertation.

From galvanostatic cycling, we can obtain information about phase transformations in electrodes under different kinetics, rate performance, structure of the intermetallics during lithiation (crystalline or amorphous), potential range for practical use, and cycle life of LIBs.

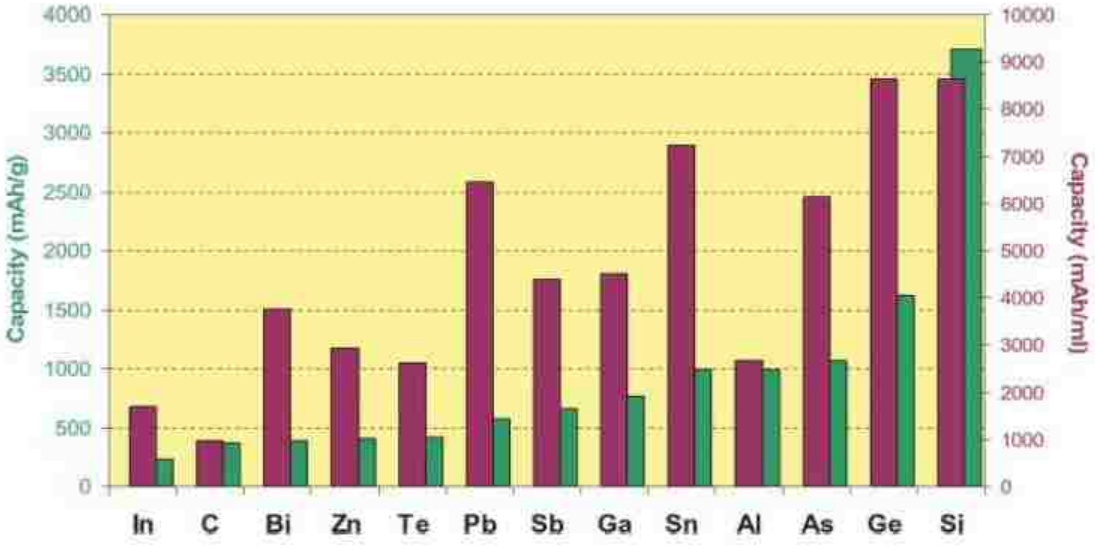

Figure 2.1 Gravimetric and volumetric capacities for selected alloying reactions.

Adapted from Reference [24]. Copyright © The Royal Society of Chemistry 2007.

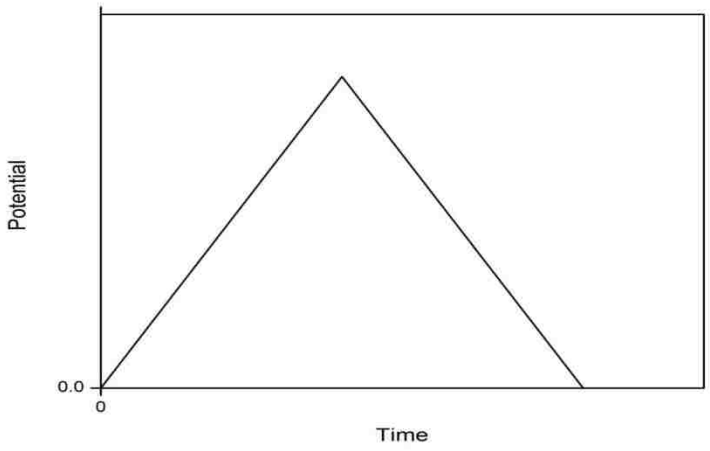

(a)

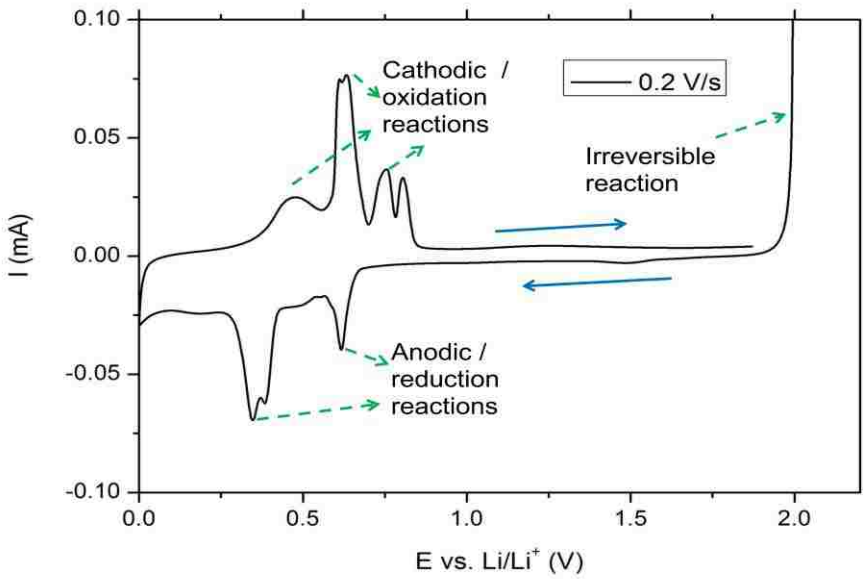

(b)

Figure 2.2 (a) Controlling profile of a CV test. (b) An example of CV of Sn vs. Li.

Chapter 3 Whisker Formation on A Thin Film Tin Lithium-Ion Battery Anode [1]

3.1 Summary

Tin (Sn) is a candidate material for negative electrodes of lithium-ion batteries (LIBs) because of its high theoretical energy capacity. In this chapter, we show an observation of Sn-whisker growth on Sn-thin films after lithiation and de-lithiation. The compressive stress generated by electrochemical lithiation of the Sn-thin films is likely the driving force for the growth of the Sn whiskers. Attention should therefore be paid to the issue of Sn whisker growth for Sn-based electrodes since Sn whiskers may penetrate through the separator, and short-circuit the electrochemical cell.

3.2 Introduction

LIBs are widely used as power supplies for various electronic devices due to their high energy and power densities. The growing demands for electronic devices, portable tools, and hybrid and all-electric vehicles require batteries with higher capacity and longer durability. Commercial graphite anodes used in LIBs have good cycling behavior with a capacity of 372 mAh g^{-1} [8]. Sn is one of the prominent materials for the negative electrodes of LIBs because of its high gravitational and volumetric capacities (992 mAh g^{-1} and 7262 mAh cm^{-3}, respectively [24]). However, the volume change from pure Sn to its fully lithiated phase ($Li_{4.4}Sn$) is approximately 260% [31]. This large volume change results in fracture and pulverization of the active material and poor cycling ability, which hinders its application as an electrode material. The large stress and strain created by volume expansion and contraction are the cause of cracks and fracture of the active materials [90-92].

---

[1] Reproduced from *Journal of Power Sources*, 196 (3): 1474-1477 (2011). Copyright © Elsevier B.V. 2010.

The electrochemical performance of Sn based alloys, such as Sn-Cu [93-95], Sn-Ni [87, 95], Sn-Zn [96], and Sn-Co [97, 98], has been studied. Capacity retention is improved due to the formation of active/inactive structure in these Sn alloys. The cycling performance of materials can also be enhanced by using nano-scale structures [18, 99, 100].

Furthermore, safety is a key issue for LIBs. But, there are few reports on the safety studies of Sn-based electrodes. In this work, we report the first observation of Sn-whisker formation after lithiation and delithiation. The Sn whiskers may be a safety concern for Sn-based LIBs.

3.3 Experimental Section

3.3.1 Thin Film Preparation

Sn thin films were deposited on 0.5 mm thick stainless steel discs by radio frequency (RF) magnetron sputtering using an Advanced Energy system. A pure Sn target (99.998%, Kurt J. Lesker) of 25.4 mm diameter was used in the sputtering. Pre-sputtering was carried out in ultra-high-purity argon (Ar, 99.999%, Scott-Gross) at 50 W for 5 mins to remove any oxides and contaminations on the Sn target surface. Sn sputtering was performed in Ar with a working pressure of 3 Pa and a power of 30 W. The substrate was kept at room temperature of about 23°C during sputtering. The film thickness was recorded by a quartz crystal microbalance thickness monitor (Inficon) during sputtering, and was examined by a Dektak 3030 profillometer (Veeco) after sputtering. Immediately after sputtering, samples were annealed at 200°C under Ar atmosphere for 2 hours to remove internal stresses generated during the sputtering.

3.3.2 Electrochemical Measurements

The electrochemical performance of the as-prepared Sn thin films was evaluated using 2025-type coin cells (Hohsen). The stainless steel substrate served as the current collector to obtain a uniform current distribution. Pure lithium foils (99.9%, Sigma Aldrich) were

cut into proper size and used as the counter electrode. Poly-propylene woven separators (Celgard 3501) were used in the coin cells. 1 M $LiPF_6$ in ethylene carbonate / dimethyl carbonate (EC/DMC, 1:1 by vol.) was used as the electrolyte (Novolyte). Electrochemical performance was conducted using a VMP3 multi-channel potentiostat/galvanostat (Bio-Logic). Galvanostatic cycling of the cells was carried out at a rate of C/10 between 1.2 V and 0.02 V.

3.3.3 Characterization

After cell disassembly, the Sn thin films were cleaned using DMC (99%, Alfa Aesar), and then examined by scanning electron microscope (SEM, Hitachi S-4300 at 3 kV) and field emission transmission electron microscope (FETEM, JEOL 2010F at 200 kV).

3.4 Results and Discussion

Before performing the first galvanostatic cycle, the Sn electrode was rapidly lithiated to 1.2 V relative to pure Li to avoid the anomalous irreversible capacity during initial lithiation of Sn [101]. The initial galvanostatic cycle within the 0.02 V – 1.2 V potential window is shown in Fig. 3.1. The Sn thin film electrode had a reversible capacity of 725 mAh g^{-1} during the first cycle. The irreversible capacity of 155 mAh g^{-1} at the first cycle was mainly due to the formation of solid electrolyte interphase (SEI) on the electrode, which consumed Li ions from the electrolyte [47]. After removing the effect of SEI on the initial lithiation capacity, the calculated Li to Sn atomic ratio is 3.2:1. This ratio suggests a combination of Li-Sn phases which do not have a long-range ordered structure [13]. The theoretical capacity of Sn (992 mAh g^{-1}) is calculated based on the formation of the ultimate phase of lithiation, $Li_{4.4}Sn$. However, it is difficult for Sn to be fully lithiated to the state of 4.4 Li atoms per Sn atom at room temperature, due to the limited diffusivity of Li atoms in Sn and Li_xSn_y phases, and due to the non-equilibrium electrochemical condition. Our results of Sn cycling show that even at a relatively slow rate of C/70, $Li_{3.8}Sn$ formed after full lithiation. This observation is consistent with a previous study [13].

To compare the structural change of Sn-thin films due to the electrochemical cycling, the morphology of 500 nm Sn films before and after electrochemical lithiation, and after delithiation is shown in Fig. 3.2. During sputtering, Sn thin films were not uniform due to the high mobility of Sn atoms. Though the surface of the as-prepared Sn thin film was not uniform, there was no whisker growth observed after the sputtering. Furthermore, no whisker formation was observed after leaving the Sn thin films in ambient environment for 30 days. This indicates that the internal stress was negligible in the Sn-thin films after annealing. However, after lithiation, the formation of long Sn whiskers and large Sn hillocks was observed, as shown in Fig. 3.2 (b). The average number of Sn whiskers per unit area was calculated to be 1306 ± 280 in 1 mm^2. The length of the Sn whiskers ranges from several μm to 30 μm, with a diameter of 150 to 300 nm. In addition, cracks formed on Sn thin films after the first lithiation/delithiation cycle, as shown in Fig. 3.2 (c).

Fig. 3.3 (a) and (b) show the FETEM image of a randomly selected whisker after one cycle of lithiation/de-lithiation. The sharp edges and corners of the whisker in Fig. 3.3 (a) and the periodic atomic structure in Fig 3.3 (b) indicate that the whisker is a single crystal, whose crystal structure was confirmed by selected area electron diffraction (SAED, inset of Fig. 3.3 (a)) to be body-centered tetragonal (β-Sn) with the [01-2] direction along the axis of the whisker. There is an amorphous layer covering the crystalline whisker, which may be the remaining SEI layer [102] after sample cleaning by DMC or an oxide layer [103, 104] formed during the TEM sample preparation. While the majority of the layer is amorphous, a small portion shows aligned structure, suggesting crystallization of SEI as indicated by the circle in Fig. 3.3 (b).

Sn-whisker formation and growth have been extensively studied, and Sn whiskers have been observed on electrodeposited and sputtered Sn thin films [105-107]. Sn whiskers usually form due to stresses which are generated during solid-state reaction of Sn and the Cu substrate to form intermetallic compounds, such as Cu_6Sn_5 [107-109]. Generally, whisker growth is a result of the compressive stress along the thickness direction of the film by a “squeeze out” mechanism [107, 110]. A related phenomena is the stress-induced growth of nanowires caused by hundreds of MPa of compressive stress incurred

during film deposition [111]. Recently, the effect of aging time on Sn-whisker growth from thin films and their anode behaviors in LIBs have been studied [112].

In the present experiment, intermetallics do not form between the Sn thin film and the stainless steel substrate. The formation of Sn whiskers is likely caused by the lithiation-induced stress. During lithiation, Li and Sn form Li_xSn phases, which create large compressive stress in the Sn film because of volume expansion and constrain of the substrate. Our results of stress measurement using a home-built laser-curvature device show that the compressive stress in Sn thin films is about 700 MPa during lithiation. This compressive stress, which is higher than what is usually required for Sn whisker growth, leads to the "squeeze out" of Sn atoms form Sn whiskers during lithiation.

Pure Li metal has several advantages over other anode materials for LIBs, including large specific capacity, and high energy density. However, a detrimental phenomenon that impedes the application of pure Li metal as anodes of LIBs is the morphological change of Li metal and the formation of Li dendrites [1, 113, 114] during electrochemical cycling. The Li dendrites can penetrate through the separator, short-circuit the electrochemical cell, and thus causes serious safety problems. Safety is more prominent in the application of large number of cells, such as hybrid and all-electric vehicles, than individual cells, since the probability of failure of a battery pack consisting of many individual battery cells in series is proportional to the number of cells. Problems with any individual cell could damage the whole power supply.

The shear moduli of pure Sn and pure Li at room temperature are 19.0 GPa [115] and 4.2 GPa [116], respectively. It is expected that the strength of single crystal Sn whiskers is much greater than single crystal and polycrystalline Li dendrites, because the theoretical strength of a single crystal is approximately 1/10 of its shear modulus. Similar to the lithium dendrites, Sn whiskers may also penetrate through the porous polymer separator and cause a short-circuit of the LIB. Actually, the initial interest in study on Sn whiskers was raised by the fact that Sn whiskers formed from solders could short-circuit electronic circuits and destroy electronic devices. The observed formation of Sn whiskers during

lithiation of Sn-thin film electrodes suggests the need for more detailed studies of whisker formation in alloy electrodes consisting of low melting point elements, such as Sn, as well as the effects of whiskers on the safely of LIBs.

3.5 Conclusions

In this chapter, we report the first observation of Sn whisker growth after lithiation of Sn thin film electrodes. The formed whiskers are pure Sn single crystal. The high compressive stress during lithiation is likely the driving force for the whisker growth. Since these whiskers may short-circuit the cells, more detailed studies of lithiation-induced whisker growth and their safety implications are needed for Sn-based electrodes in LIB applications.

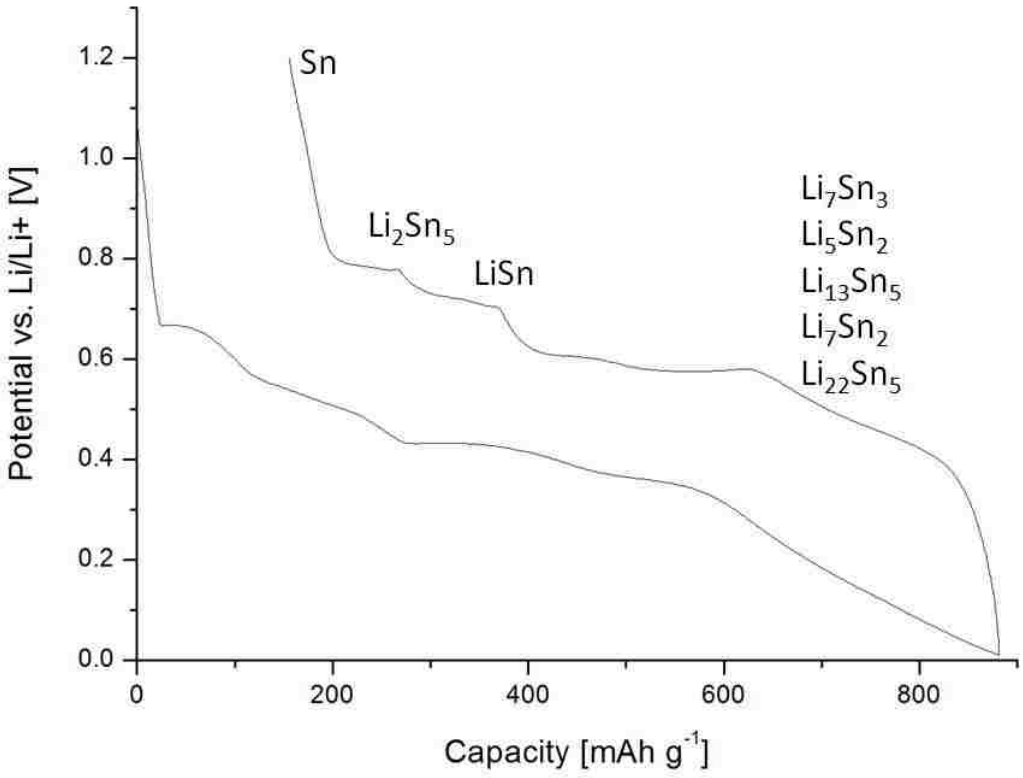

Figure 3.1 First cycle galvanostatic discharge/charge curve of Sn at C/10 rate.

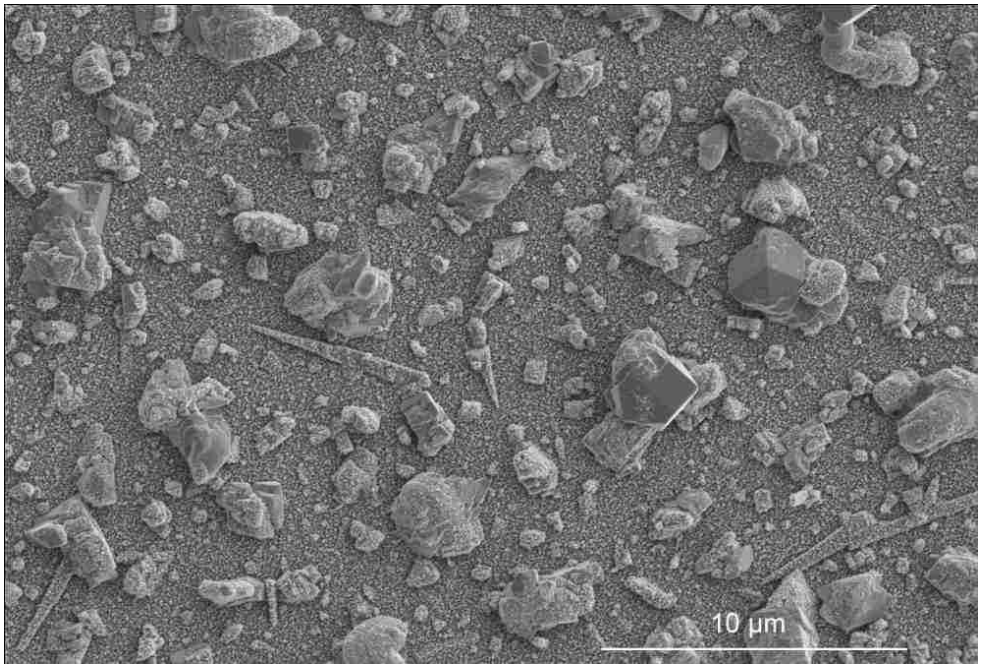

(a)

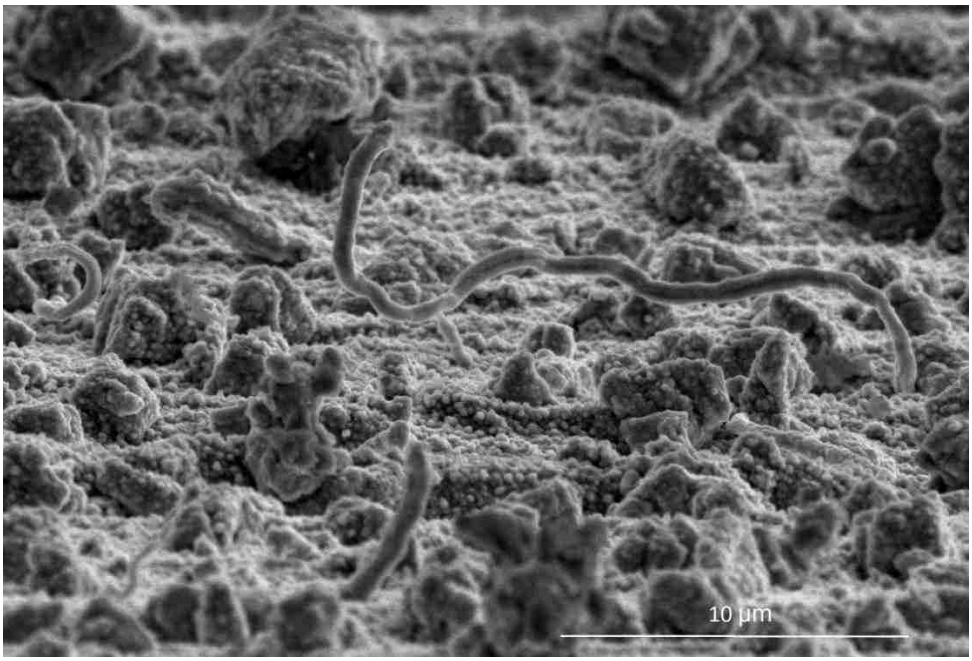

(b)

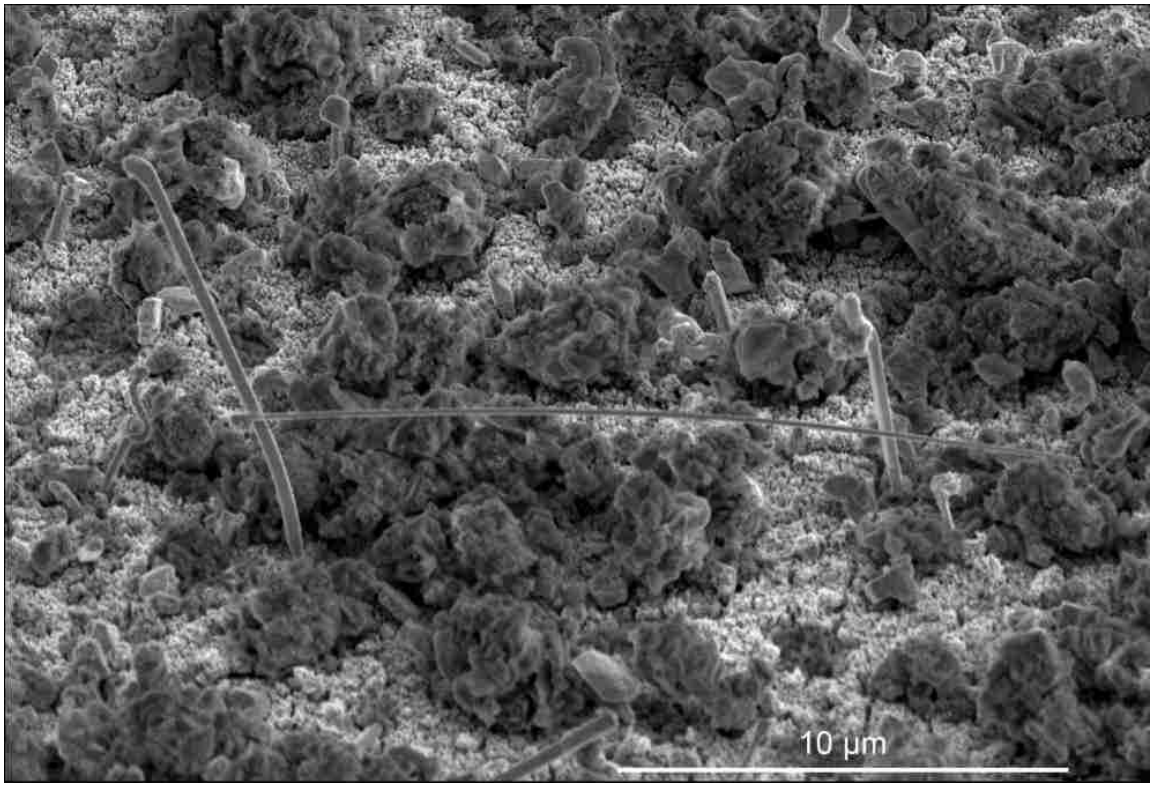

(c)

Figure 3.2 (a) An SEM image of Sn after annealing at 200°C for 2 hrs. (b) Surface morphology of Sn at the stage of full lithiation. The sample stage is tilted at 80°. (c) Surface morphology of Sn after one cycle of Li insertion/extraction. The sample stage is tilted at 60°.

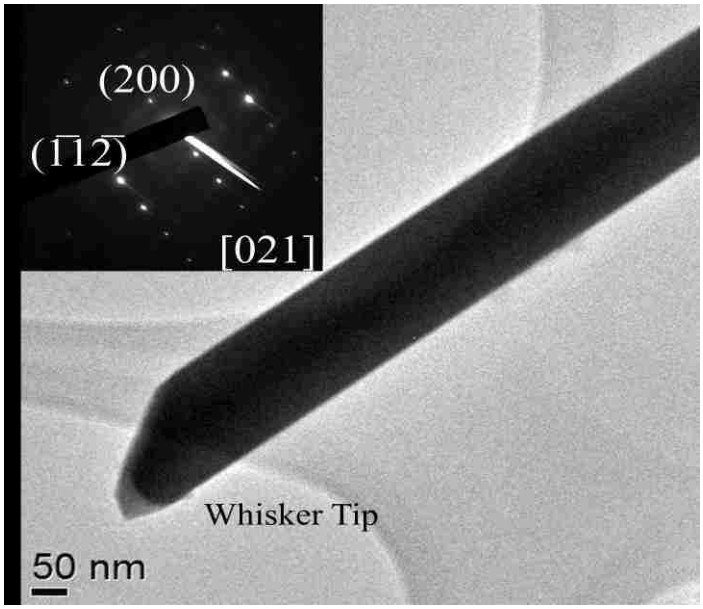

(a)

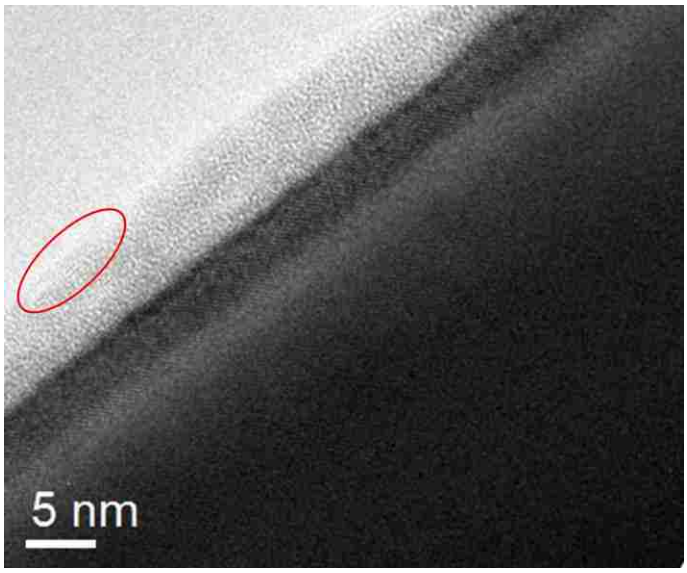

(b)

Figure 3.3 (a) A TEM image of a randomly selected Sn whisker after one cycle of lithiation/delithiation. The inset SAED indicates single crystal whisker with [01-2] direction along the axis of the whisker. (b) Enlargement of the whisker in (a). Red circle indicates aligned structure of the amorphous shell.

Chapter 4 Crack Pattern Formation in Thin Film Lithium-Ion Battery Electrodes [2]

4.1 Summary

Cracking of electrodes caused by large volume change and the associated lithium diffusion-induced stress during electrochemical cycling is one of the main reasons for the short cycle life of lithium-ion batteries using high capacity anode materials, such as Si and Sn. In this chapter, we study the fracture behavior and cracking patterns in amorphous Si thin film electrodes as a result of electrochemical cycling. A modified spring-block model is shown to capture the essential features of cracking patterns of electrode materials, including self-similarity. It is shown that cracks are straight in thick films, but show more wiggles in thin films. As the thickness of film decreases, the average size of islands separated by cracks decreases. A critical thickness bellow which material would not crack is found for amorphous Si films. The experimental and simulation results of this work provide guidelines for designing crack free thin-film lithium ion battery electrodes during cycling by patterning the electrode and reducing the film thickness.

4.2 Introduction

The rapid development of portable electronics, hand tools, and electric vehicles demands ever higher capacity and more durable rechargeable batteries, in particular, lithium-ion batteries (LIBs). New battery electrode materials with higher capacity than the commercially available graphite and $LiCoO_2$ are being explored extensively. The most promising materials for the anodes of LIBs are Si, Sn, Ge, and their alloys. However, these materials usually show a much shorter cycle life compared to commercial graphite electrodes. The main cause for the poor cycling behavior is fracture of electrodes, which

---

[2] Reproduced from *Journal of The Electrochemical Society*, 158 (6): A689-A694 (2011).

is the result of large volume change and the associated large diffusion-induced stress (DIS) [90, 117].

Cracking during electrochemical lithiation and de-lithiation has been observed in electrode materials such as Si [118], Sn [18, 119], Si-Sn alloys [31], Ni-Sn alloys [119, 120], and Ge [14]. Cracking patterns have also been observed and studied in other fields of inquiries, including deposition of amorphous Si film [121], drying of clays [122] and polymer paints [122], glasses [123], and aging of woods [124]. The ubiquitous and intriguing cracking patterns have generated broad interest in understanding the mechanisms of crack evolution and pattern formation in a number of fields. Several models have been proposed to simulate the cracking behaviors caused by drying and other physical and chemical shrinkage processes [122, 124-126]. Sadhukhan *et al.* proposed a one-dimensional spring chain model to mimic the cracking behavior in drying of polymer on different substrates [127]. Nag *et al.* developed this model to simulate two-dimensional cracking patterns in polymer with additives [122]. Leung *et al.* developed a simple two-dimensional spring-block model which captured the essential features of cornstarch drying successfully [125]. Valette *et al.* developed a three-dimensional model to dynamically simulate the cracking on surface of a desiccating crusted soil [126]. In addition, finite element analysis has been applied to simulate fractures by shrinkage in various objects by several groups [128, 129].

In this chapter, we study crack pattern formation in amorphous Si (a-Si) thin film electrodes as a result of electrochemical lithiation and delithiation cycles. We also present a modified spring-block model to simulate crack pattern formation in thin film LIB electrodes. This work provides guidelines for designing LIB electrodes that do not crack during cycling.

4.3 Experimental Section

4.3.1 Preparation of Thin Films

Amorphous Si thin films were fabricated by sputtering Si onto 0.5 mm thick 430-type stainless steel (SS) disks in a commercial magnetron sputtering system (Advanced Energy). Prior to the sputtering deposition, the SS disks were ground and polished using 50 nm Al_2O_3 colloidal to remove surface scratches which could affect crack formation. A 25.4 mm diameter target of pure Si (99.995%, Kurt J. Lesker) was used for the sputtering deposition. Pre-sputtering was carried out at 100 W for 20 mins to remove oxides on the Si target surface. Si thin films were deposited using a RF power supply operating at 100 W. During deposition, the chamber pressure was kept at 1 Pa of Ar. Film thicknesses ranged from 100 to 1000 nm, as measured by a quartz crystal microbalance (Maxtek) during deposition and by a Dektak profilometer (Veeco 3030) after deposition.

4.3.2 Electrochemical Measurements

After deposition, Si films were assembled in CR2025 coin-type half cells (Hohsen) for electrochemical examination. Pure Li metal (99.9%, Sigma Aldrich) foils were used as the counter electrodes. The electrolyte used was 1 M $LiPF_6$ in ethylene carbonate / dimethyl carbonate (EC/DMC, 50/50 by volume, Novolyte). A computer-controlled multi-channel potentiostat (VMP3, Bio-Logic) was used to conduct the electrochemistry measurements. The coin cells were galvanostatically cycled at a rate of C/10 at room temperature (21°C). The high and low potential cut-offs for cycling the Si thin film electrodes were 2.0 V and 0.002 V relative to pure Li, respectively. Discharging refers to lithium going into Si (i.e., lithiation of Si), and charging refers to Li coming out of Si (i.e., de-lithiation of Si).

4.3.3 Materials Characterization

After cycling, scanning electron microscopy (SEM) imaging was performed using a Hitachi S-4300 with an acceleration voltage of 3 kV.

4.4 Modeling

A computer program was implemented to simulate the cracking phenomena in thin film electrodes. The program is based on the model proposed by Leung *et al.* [125] and was modified to apply a constant strain, ε, as the film contracts to simulate a constant rate of delithiation, which approximates the condition for galvanostatic charging [117]. This model consists of a two-dimensional array of hexagons with each side of the hexagon connected to its partner by a number of elastic springs, as illustrated in Fig. 4.1. The purpose of this 2-D spring-block model is to keep the essential physics of cracking behavior, while avoiding going to the details of materials behavior, which usually complicates models largely.

Initially, the hexagons are separated by a distance of one unit, with the strain ε being expressed as the length change required for a spring to have a neutral length which would have no compressive or tensile force. The magnitude of the constant strain ε in the model can be selected along with three other parameters, volume reduction ΔV, the number of springs per side H, and the ratio of cracking to slipping force $k = F_c/F_s$. The parameter k specifies whether a spring will be broken on a side of the hexagon or if the hexagon will slip to a new position using a threshold rule [125]. This ratio is related to the fracture strength of the active material and adhesion strength between the active layer and the substrate. The model is constructed using dimensionless units so it can be scaled.

Once the initial conditions are set up, the evolution of the system is determined by the following four major steps. (1) The hexagons are displaced randomly by a small distance and a strain ε is applied. (2) The force matrix is computed for all the hexagons, and for all sides of each hexagon. While k is fixed, the thresholds F_c and F_s are lowered until either is exceeded. (3) If F_c is exceeded by the forces on a bundle of springs, one spring with the largest net force is broken. (4) If F_s is exceeded by the net force on a hexagon, the hexagon is moved to an equilibrium position (slipping) where the net force on this hexagon is zero. After this step, the force matrix is recomputed for the system and steps

(2), (3), and (4) are repeated. The entire process takes multiple iterations to reach the final state when the generated cracking pattern does not change further.

The above model is valid if $\varepsilon \ll 1$, as in the case for mud drying [125]. A LIB anode undergoes a large volume change during cycling [130], so that the Leung *et al.* model was modified to keep the overall strain on the system small albeit constant; in other words, the strain $\varepsilon < \Delta V/V$, and does not decrease as the system shrinks. In the condition of constant current controlled cycling [117], there is a constant flux of Li passing through the electrode/electrolyte interface. The constant current charging case is equivalent to surface reaction controlled delithiation with very small electrochemical Biot Number (i.e., $B \ll 1$) [90, 131]. After a period, stress and strain in the electrode reach steady-state values which are independent of time [117]. Although strain is not the same everywhere in the electrode, the average strain is constant. To maintain this constant strain, a fifth simulation step is added: (5) After each iteration over steps (1)-(4) an image of the system is scanned to determine the total amount of shrinkage. From this an average hexagon size is computed and a new neutral spring length is determined to maintain the constant strain level. The new image is captured, and steps (2)-(5) are repeated until the total volume change reaches the pre-set value ΔV.

The number of springs per side H has the same effect as film thickness h, i.e., a large number of springs represents a thick film [125]. It is also found that H and k have the same effect on crack patterns. In other words, a fixed value of kH gives the same cracking pattern. In this work k was fixed to be 0.5 for all simulations, which gave the number of springs per side H of 2, 3, 5, 7, and 10 corresponding to the 200, 300, 500, 700, and 1000 nm thin films in experiments, respectively. Different values of constant strain ε were found to best represent the data for differing thicknesses, with the highest 0.18 being used for the thinnest 200 nm film and the lowest of 0.08 being used for the thickest film. This corresponds to strain being highest at the top of the film where delithiation occurs. By using the area of the cracks in the film plane and comparing it with the

existing volume shrinkage data, the amount of volume reduction ΔV in the model was adjusted to present the in-plane shrinkage observed in experiments.

4.5 Results and Discussion

Fig. 4.2 (a) shows the typical cycling performance of a 500 nm thick a-Si film. It has been reported that phase transformation and crystallization occur during lithiation of a-Si [27]. The final product of lithiation of a-Si is crystalline $Li_{15}Si_4$. After full delithiation, material returns to the amorphous state with some residual $Li_{15}Si_4$ [23, 27]. However, there is no well-defined single-phase region (vertical line) or two-phase region (horizontal line) in the observed potential vs. charge profile, indicating that the reaction does not fully follow the Si-Li equilibrium phase diagram under the condition used in this experiment. The initial lithiation capacity of the 500 nm a-Si film is 3158 mAh g^{-1}. The initial reversible capacity is 2680 mAh g^{-1}, suggesting that the material is lithiated to a state of $Li_{2.8}Si$ which corresponds to 74% of theoretical capacity of Si (3600 mAh g^{-1}). It is generally believed that the initial irreversible capacity is attributed to (1) the formation of a solid electrolyte interphase (SEI) on the surface of active material [47], (2) side reactions with impurities, and (3) partial loss of electronic contact due to expansion and contraction of the electrode material. The second cycle reversible capacity of the a-Si film decreases drastically to 1937 mAh g^{-1} (54% of theoretical capacity). The reversible capacity fades slowly with further cycling. After 30 cycles, the 500 nm thick a-Si film shows a reversible capacity of 1256 mAh g^{-1}, corresponding to 35% of its theoretical capacity. Amorphous Si films with thicknesses of 200 nm and 100 nm show large irreversible capacity during the first cycle, and high reversible capacity retention with cycles (Fig. 4.2 (b)).

Similar observations of severe reversible capacity dropping during several initial cycles of Si electrodes have been reported by other researchers [35, 132-134]. It is believed that this loss of reversible capacity (de-lithiation capacity) at initial cycles is not due to the formation of SEI because the formation of SEI is largely irreversible and does not contribute to the reversible capacity [47].

To understand the mechanisms responsible for severe reversible capacity reduction, cells are disassembled after electrochemical cycling and electrodes are examined by SEM. Fig. 4.3 (a) shows the morphology of the as-deposited 500 nm a-Si thin film and the cracking patterns generated in a-Si films of selected thicknesses after lithiation/delithiation cycles. Before cycling, there is no crack in the a-Si films. After cycling, a-Si thin films break up into individual pieces separated by interconnected cracks. Though not connected with each other, most of the pieces are connected to the substrate, and remain active during lithiation and delithiation cycles. Since the SS substrate is about one thousand times thicker than the a-Si thin film, the curvature change of the substrate during electrochemical cycling is small. During delithiation, the removal of lithium from the Li_xSi phases causes a large tensile stress, which can be as large as several GPa and exceeds the tensile strength of a-Si [21]. Thus, interconnected, through-thickness cracks form in the a-Si thin films after electrochemical cycling.

The generated crack patterns vary with thickness of a-Si thin films. For the 1000 nm thick a-Si thin film (Fig. 4.3 (b)), a branch of primary cracks propagates until reaching another branch, and all of these cracks are long and straight with a few sharp changes in direction. These cracks show a characteristic of crack "growth", rather than crack nucleation. The islands separated by straight and long cracks show simple shapes. The number of crack initiation sites or the density of cracks (total length per unit area) in the final state is relatively small. With decreasing film thickness, cracks show more branches and wiggles, as shown in Fig. 4.3 (c) and 4.3 (d). Although most cracks are interconnected with each other, there are many places where cracks are unable to propagate. With more crack initiation sites, the density of cracks is higher. The islands separated by cracks have more complicated shapes.

Fig. 4.4 shows representative simulation results of crack patterns generated by shrinkage using the modified spring-block model. Although this modified model is relatively simple, it shows a good agreement with experiments, as seen by comparing Fig. 4.4 with Fig. 4.3. When H =10 (representing the 1000 nm film, Fig. 4.4 (a)), cracks are straight with a few sharp changes in direction, and blocks separated by cracks have simple shapes. With

decreasing H (lowering film thickness), cracks show many wiggles and islands separated by cracks show complicated shapes. Furthermore, there are multiple sites in Fig. 4.4 (b) and 4.3 (c) where cracks stop growing at their tips. This spring-block model can be applied to simulate cracking in thin film LIB electrodes of other materials, such as Sn and its alloys, by choosing adequate values for the model parameters. The model parameters can be calibrated by experiments or theoretical calculation of the mechanical properties of electrodes.

A scaling behavior is observed between the average cracked area A and the film thickness h, as shown in Fig. 4.5. This scaling behavior suggests a power-law relation: $A \propto h^n$, in which n was found to be 2.16, close to a recent prediction [125]. This relationship predicts the average area separated by cracks under a specific condition, including mechanical properties of active materials, rigidity of substrate, interface friction, and the film thickness. Because the exponent is a function of film thickness, the cracking pattern is not the same for all thin films. In fact, it shows that as the thickness decreases, the density of cracks increases until a critical thickness below which no crack is found. Therefore, it is reasonable to conclude that the active thin film materials would not crack during lithiation/delithiation if the characteristic size of active material is smaller than the predicted average cracked area A. To understand this phenomenon from a point of view of force equilibrium, a methodology similar to that proposed by Xiao *et al.* [39] is used. To simplify the problem, a square pattern electrode with length of a_{cr} and height of h is shown in Fig. 4.6. Upon delithiation, the active material undergoes a tensile stress of σ_Y^{Si}. However, the active layer cannot yield or fracture freely because of the constrain from the substrate and the friction at the active material/substrate interface τ_{cr}^{int}. Force equilibrium yields $\frac{\tau_{cr}^{int} a_{cr}}{2} = \sigma_Y^{Si} h$, where the interfacial force τ_{cr}^{int} is the minimum of the shear flow stress of the substrate τ_Y^{SS} and the interfacial friction strength τ_f^{int}. For stainless steel τ_Y^{SS} is about 186 MPa. Since the friction strength between metal and silicate composite τ_f^{int} is about 40 MPa [135], the interfacial force is taken to be 40 MPa

as an approximation. The yield strength of lithiated Si is on the order of 1 GPa [21]. The one-dimensional (1-D) critical size for crack initiation can be calculated by

$$a_{cr} = 2\frac{\sigma_Y^{Si}}{\tau_{cr}^{int}}h \tag{4.1}$$

The calculated 1-D cracking size a_{cr} is 10, 25, and 50 μm for 200, 500, and 1000 nm thin films, respectively. Although the relationship between the calculated 1-D critical size for cracking and film thickness does not match perfectly with experiments because of lack of accurate data on yield stress of lithiated Si and the friction between Li_xSi alloy and SS substrate, the linear relationship between 1-D critical cracking size and film thickness gives a relation of $A \propto h^n$ with n =2, close to our prediction 2.16. It has been known that the adhesion strength between active materials and the substrate plays an important role in cycling performance and that cracking could affect the bounding strength [118]. Local buckling and delamination as a result of weak bonding between the active material film and the substrate could also affect the crack patterns [92]. However, since few peeling-off events were observed in this work, we assume that the a-Si layer has good adhesion with the SS substrate during cycling.

From the discussions above, once an interconnected crack pattern is formed, stress in the thin film during cycling is not large enough to generate more cracks. We have observed experimentally that after stabilization of cracking patterns during the initial cycle, crack pattern does not change much with further cycling. However, surface roughness increases with cycling. Comparing Fig. 4.7 with Fig. 4.3 (c), we found that primary cracks do not change much with more cycling because the tensile stress is not large enough to generate new cracks. This observation suggests that pre-generated cracking in electrodes with proper dimensions could prevent further cracking in materials. It has been reported that properly patterned Sn alloy thin film [40] and Si thin film [39] would not crack further with electrochemical cycling. This method, pre-generating cracks in active materials or patterning the electrodes, can be applied to design more durable LIB electrodes which do not crack with cycling.

Furthermore, it is likely that a critical thickness h_c for crack generation exists based on Griffith's fracture criterion of materials [136]. In this theory, crack initiates if the force to drive the crack was greater than the cracking resistant force. Cracking would occur if the stored strain energy was larger than the surface energy required for the new surface after cracking [136]. According to Griffith's energy criterion, there is a critical thickness h_c bellow which crack would not form. This critical thickness h_c can be calculated as [136]

$$h_c \approx 4\sqrt{2}\frac{G_c E}{\sigma^2(1-\gamma^2)} \tag{4.2}$$

where E and ν are Young's modulus and Poisson's ratio, respectively. σ is the stress in thin film, and G_c the cracking resistance force. G_c is directly related to fracture toughness of materials K_{IC} by $G_c = \frac{K_{Ic}}{E'}$, where $E' = E$ for plane stress condition. Although mechanical properties for amorphous Si and its lithiated phases are largely unknown, we can estimate the order of magnitude of the critical thickness h_c for cracking in amorphous Si. Taking K_{IC}=1 MPa $m^{1/2}$ and ν=0.2 for a-Si [137], and σ=2 GPa [21], the calculated critical thickness is on the order of several hundred nm. The actual critical thickness should be smaller because the fracture toughness of Li_xSi is smaller than that of a-Si due to softening effect of lithiation [137]. Fig. 4.8 shows that interconnected cracks do not form in the 100 nm thick Si thin films up to 10 cycles of lithiation/de-lithiation. The critical thickness for crack initiation h_c in a-Si thin film is, therefore, between 100 and 200 nm.

In addition to the scaling behavior between cracking area and film thickness shown in Fig. 4.5, the shape of crack patterns varies with film thickness h. Fig. 4.9 shows the area-perimeter scaling and the fractal dimension of the crack patterns with different film thickness. In this work, the fractal dimension d_f is defined as the power of area to perimeter. For all the films, the cracked areas or islands show a power-law scaling behavior (Fig. 4.9 (a), 4.9 (b), and 4.9 (c)). For films with thickness between 1000 nm and 500 nm, a fractal dimension d_f close to 2 represents simple shape or Euclidean shape, which is a result of crack growth. When the film thickness decrease to 300 and 200 nm,

d_f decreases to 1.74 and 1.57, respectively, representing complicated shapes with concave edges. The complicated shape is formed because many cracks stop propagating before reaching other crack branches.

4.6 Conclusions

We investigated crack patterns generated during electrochemical cycling of amorphous Si thin film electrodes with thickness ranging from 200 to 1000 nm. A modified spring-block model was used to simulate the crack patterns. Cracks generated in thick films are straight with a few sharp direction changes and the area separated by cracks is large. For thin films cracks show more wiggles and the average cracked area is small. After primary cracks form, crack patterns do not change further with electrochemical cycling, while the surface became rougher. The experimental and simulation results suggest two directions of designing electrodes which do not crack. One method is patterned electrodes in which the pattern size is smaller than the average cracked size for that specific film thickness. The other method is to reduce the film thickness to less than the critical thickness of cracking h_c (h_c is between 100 and 200 nm for amorphous Si on stainless steel substrate).

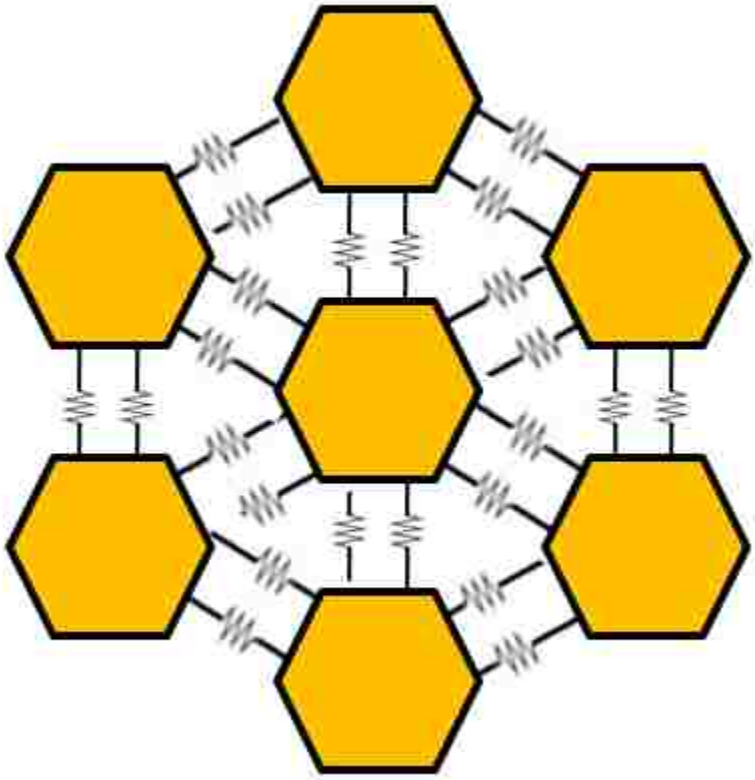

Figure 4.1 An illustration of the 2-D spring-block model. The model consists an array of hexagons, with each side of the hexagon connected to its partner by a number of elastic springs. Here 2 springs at each side are shown.

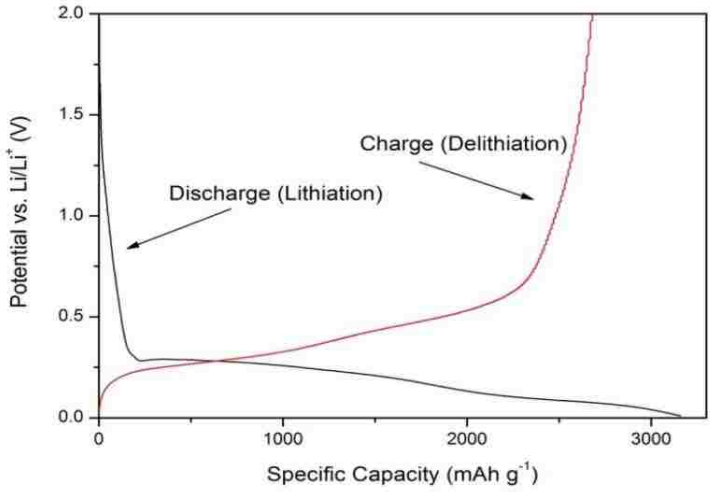

(a)

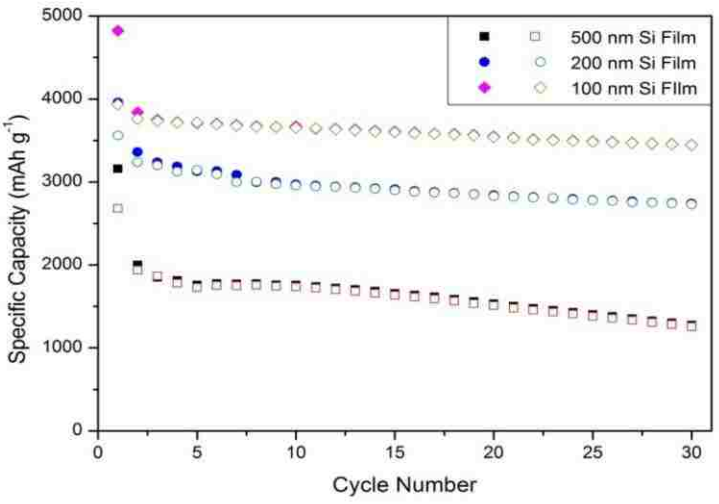

(b)

Figure 4.2 (a) First cycle potential profile for a 500 nm amorphous Si thin film. (b) Cycling performance of 500, 200, and 100 nm thick a-Si thin films. Solid symbols represent discharging and open symbols represent charging.

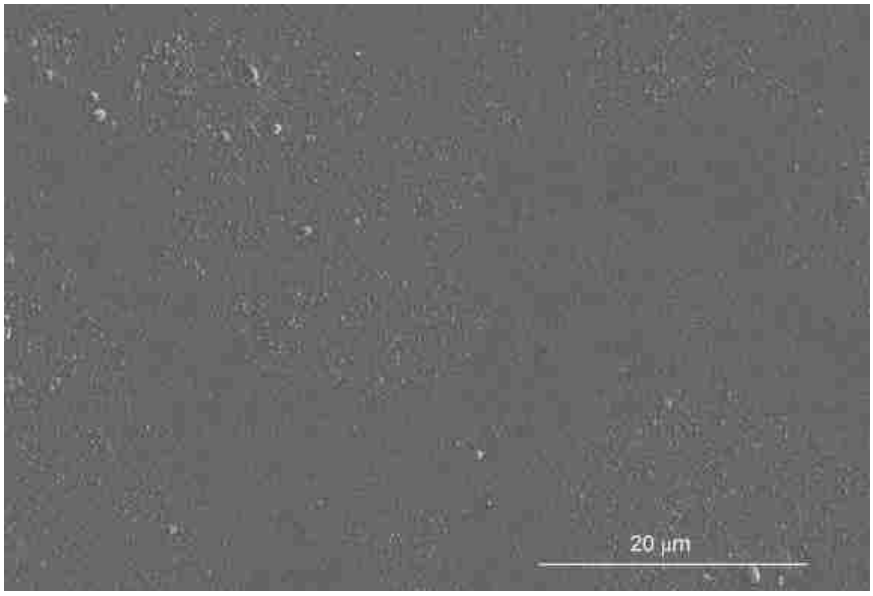

(a)

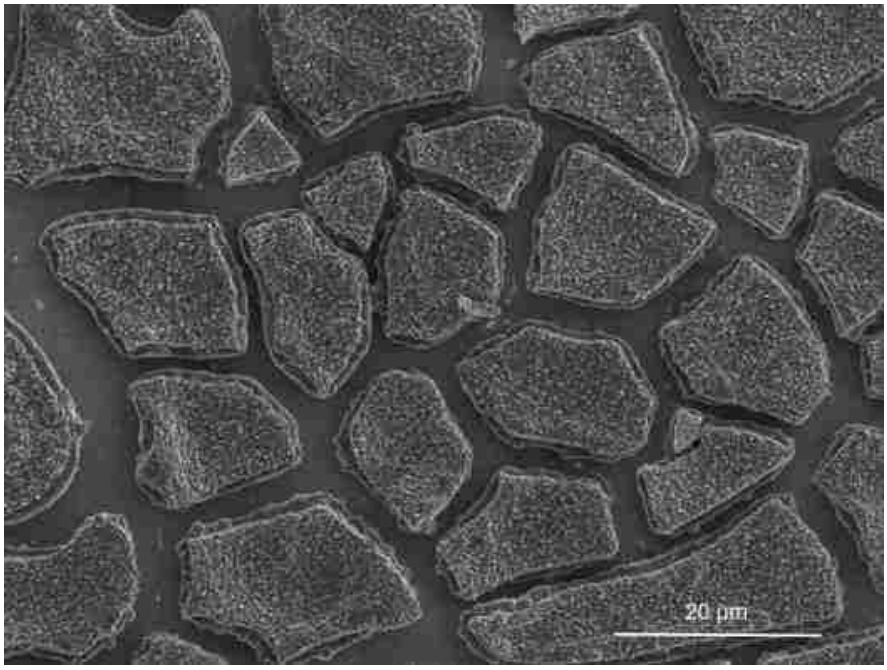

(b)

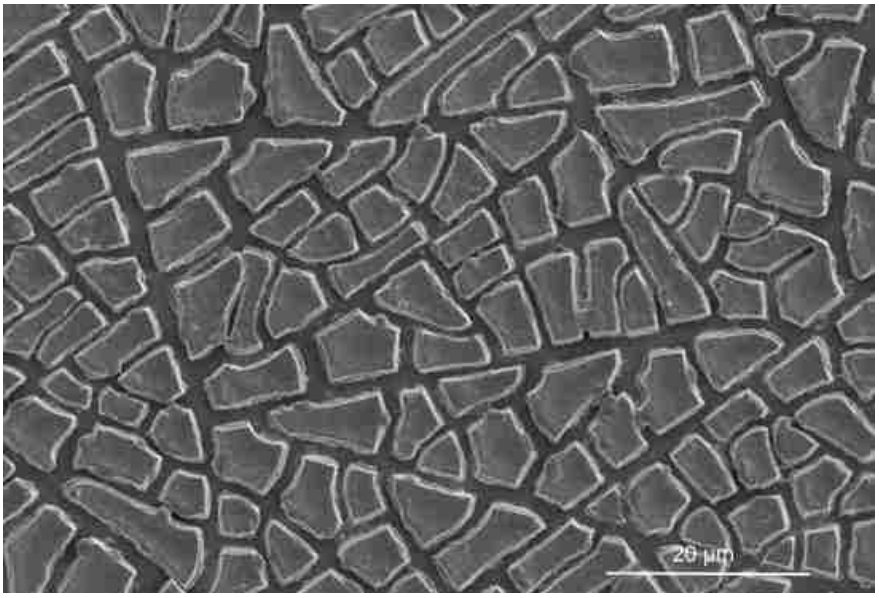

(c)

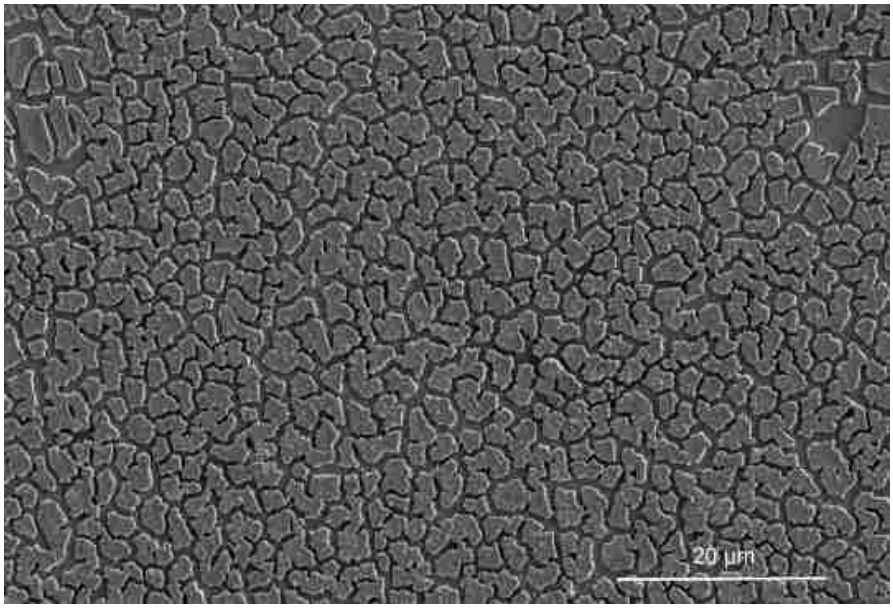

(d)

Figure 4.3 (a) An SEM image of a 500 nm a-Si film before electrochemical tests and cracking patterns formed on a-Si thin films of different thicknesses: (b) 1000 nm thick, after 5 cycles. (c) 500 nm thick, after 5 cycles. (d) 200 nm thick, after 10 cycles.

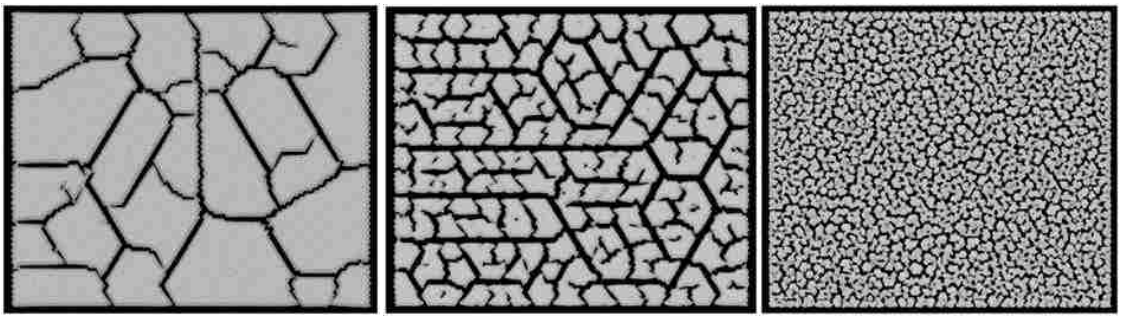

(a) (b) (c)

Figure 4.4 Simulated crack patterns representing selected conditions. The crack to slip ratio k was fixed to be 0.5, and the number of springs per side H varies. (a) H=10, representing 1000 nm thick film. (b) H=5, representing 500 nm thick film. (c) H=2, representing 200 nm thick film.

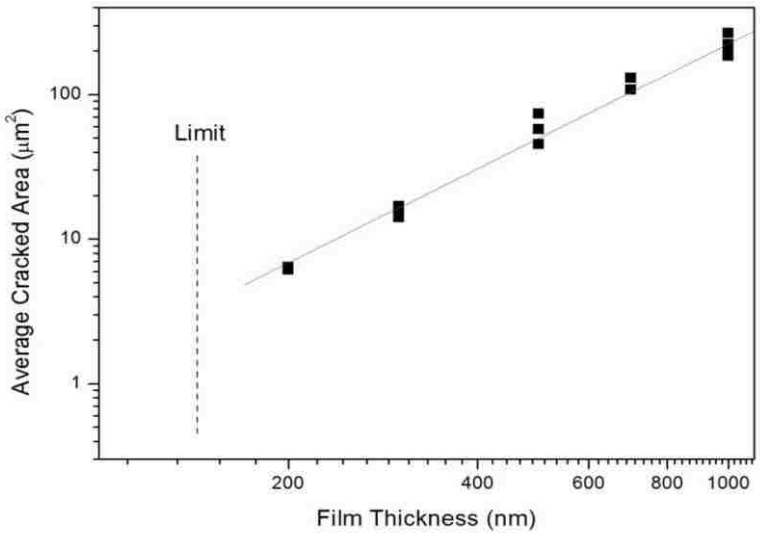

Figure 4.5 A scaling relationship between the average cracked area A and the film thickness h. The slop is found to be 2.16.

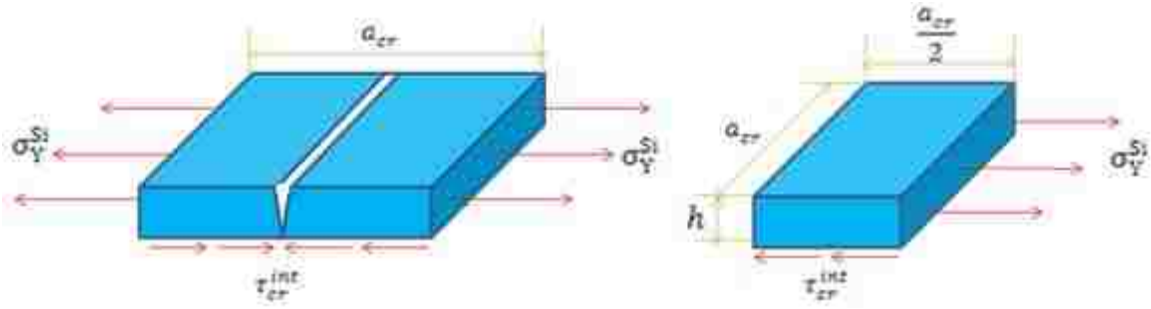

Figure 4.6 Schematic of a fractured piece of a-Si during de-lithiation. There is a tensile stress σ_Y^{Si} in the thin film during de-lithiation, and a friction τ_{cr}^{int} at the interface of active material and substrate. Formation of the pattern could be a result of natural cracking due to cycling, or could be artificially produced to avoid further cracking of electrodes.

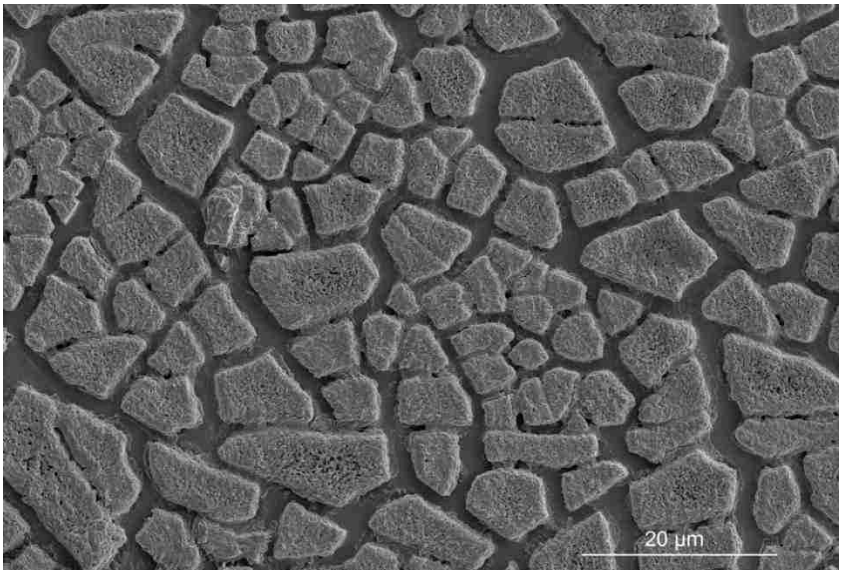

Figure 4.7 An SEM image showing surface morphology of 500 nm thick Si films after 10 electrochemical cycles.

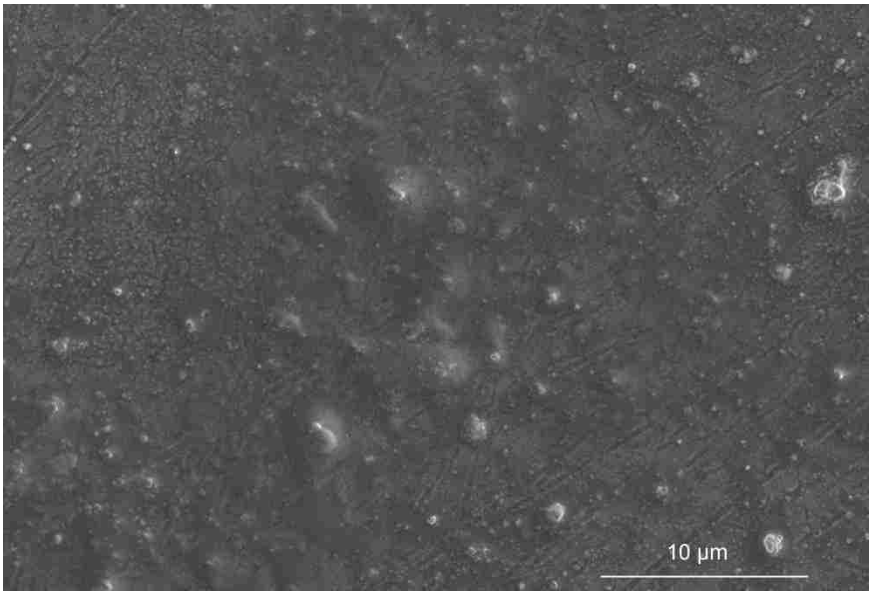

Figure 4.8 An SEM image showing surface morphology of 100 nm thick Si films after 10 electrochemical cycles.

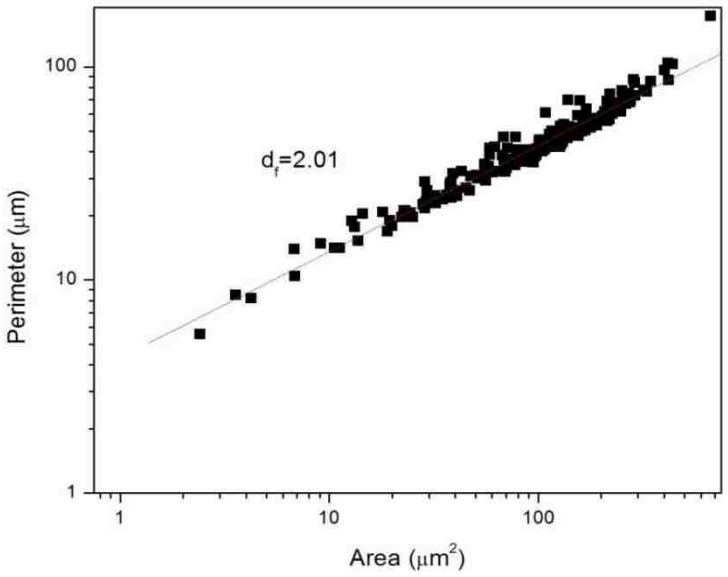

(a)

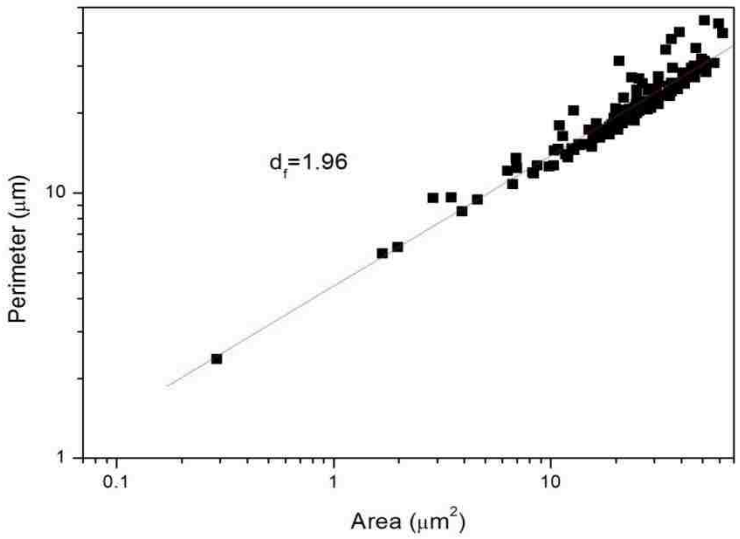
d_f=1.96
Perimeter (μm)
Area (μm²)
1
10
0.1
1
10

(b)

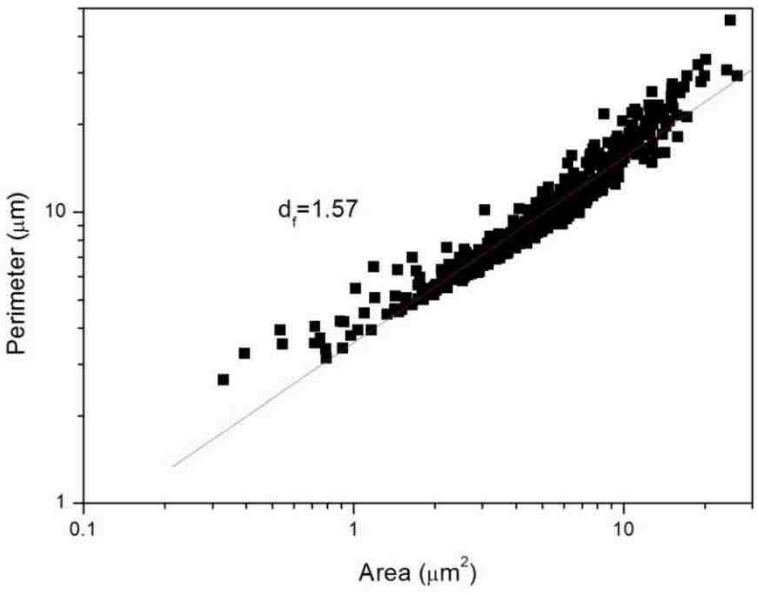
d_f=1.57
Perimeter (μm)
Area (μm²)
1
10
0.1
1
10

(c)

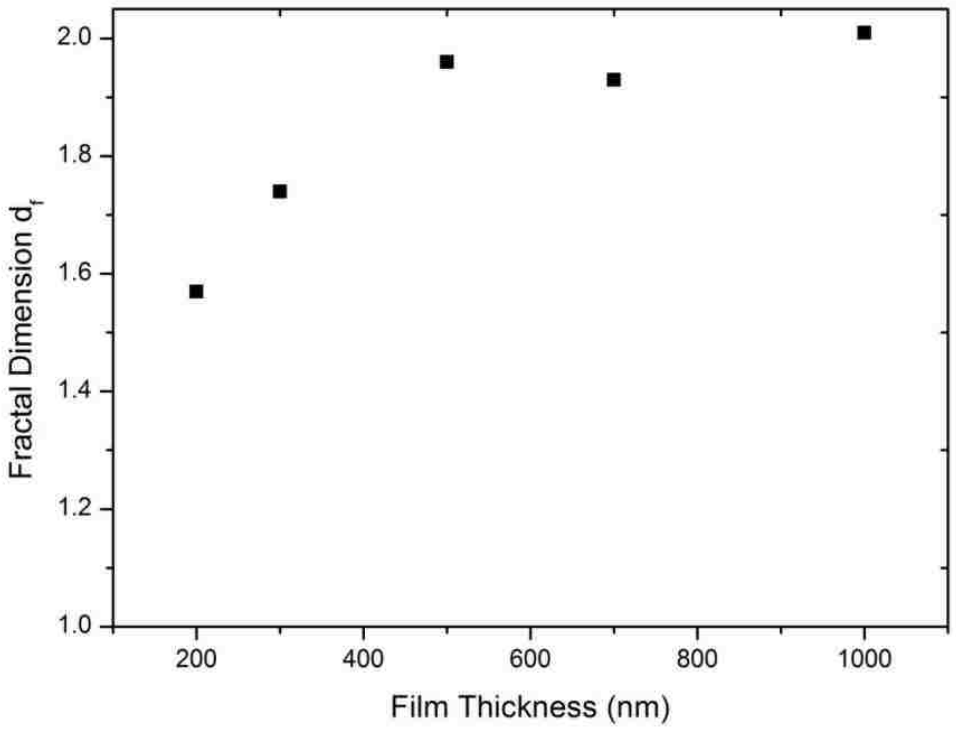

(d)

Figure 4.9 Area-perimeter scaling for islands divided by cracks. The power law fitting gives fractal dimensions d_f, which is defined as the power of area to perimeter. (a) Film thickness is 1000 nm, after 5 cycles. d_f=2.01. (b) Film thickness is 500 nm, after 5 cycles. d_f=1.96. (c) Film thickness is 200 nm, after 10 cycles. d_f=1.57. (d) d_f as a function of film thickness.

Chapter 5 Liquid Metal Alloys as Self-Healing Negative Electrodes for Lithium Ion Batteries [3]

5.1 Summary

Improving the capacity and durability of electrode materials is one of the critical challenges lithium-ion battery technology is facing presently. Several promising anode materials, such as Si, Ge, and Sn, have theoretical capacities several times larger than that of the commercially used graphite negative electrode. However, their applications are limited because of the short cycle life due to fracture caused by diffusion-induced stresses (DISs) and the large volume change during electrochemical cycling. In this chapter, we present a strategy to achieve high capacity and improved durability of electrode materials using low-melting point metallic alloys. With gallium as an example, we show that at a temperature above the melting point of Ga, a reversible solid-liquid transition occurs upon lithiation (lithium insertion) and de-lithiation (lithium extraction) of Ga. As a result, cracks formed in the lithiated solid state can be "healed" once the electrode returns to liquid Ga after delithiation. This work indicates that cracking as a failure mode can be remedied using liquid metal electrodes.

5.2 Introduction

Lithium-ion batteries (LIBs) with high energy capacity and long cycle life are employed to power numerous consumer electronics devices, portable tools, implantable medical devices, and, more recently, hybrid electric vehicles (HEVs) and pure battery electric vehicles (BEVs) [2, 3]. Many elements react with Li to form binary alloys Li_xM (where M is, for example, Si [36], Ge [14], or Sn [18]). Their theoretical (Columbic) capacities are 3 to 12 times higher than that of graphite electrodes, as they host 2 to 4.4 Li atoms per

---

[3] Reproduced from *Journal of The Electrochemical Society*, 158 (8): A845-A849 (2011).

M atom, in contrast to a single Li atom per 6 C atoms. These Li_xM alloys also show a discharge potential close to that of the Li/Li^+ reaction [3]. These materials have, therefore, been considered as potential negative electrodes for LIBs. However, low cycle life due to mechanical degradation [90, 117] and current inefficiencies associated with undesired electrochemical reaction during cycling limits the application of these high capacity electrode materials in LIBs.

Previous studies of the past 15 years that are focused on improving electrode durability can be divided into three categories: (1) alloying the Li-active materials with inactive elements, (2) building nano-structural electrodes, and (3) adding conducting and/or non-conducting buffer components. Alloying Li-active with inactive materials improves battery cycle life significantly, such as alloying Sn with Cu [138] , Co [139], or Ni [140]. However, the total gravimetric and volumetric energy densities are lowered because the inactive elements contribute to extra weight and volume. Nano-structural electrodes, such as thin-film Si [35], Si nano particles [30], Si nanowires [36] and TiO_2 nanowires [141], as well as porous transition metal oxides [142, 143], show improvements in cycle life compared to their bulk-material counterparts. However, nanostructuring reduces volumetric capacity of electrodes because of low packing density of nanowires, nanoparticles, and porous materials. Furthermore, nanostructured electrodes may suffer from increased irreversible capacity degradation due to excessive solid electrolyte interface (SEI) formation[47], and other deleterious reactions with the electrolyte (leading to reduced current efficiency relative to the desired lithiation reaction), because of their large surface area to volume ratio. Last, conducting additives and chemical binders, such as carbon black and polyvinylidene fluoride (PVDF), have been shown to improve the cycle life at the cost of extra mass and volume occupied by the additives.

In this chapter, we demonstrate a strategy of achieving high capacity and durability using low-melting point, lithium active, liquid metals (LMs) as LIB negative electrodes. This idea is based on the premise that fracture and decrepitation in LMs during cycling can be self-healed by liquid-solid-liquid transition. We examine the reversibility of lithiation of the LM pure Ga at 40°C, as a negative electrode for a LIB. Ga hosts 2 Li atoms per Ga

atom upon full lithiation, delivers a theoretical gravimetric capacity of 769 mAh g^{-1} by forming Li_2Ga alloy [144], and shows a discharge potential close to the Li/Li^+ reaction. It has been shown that LiGa alloys [145], CuGa alloys [146], and Ga confined in carbon matrix [147] deliver capacities of about 200 to 400 mAh g^{-1} upon extended cycling.

5.3 Experimental Section

5.3.1 Cell Assembly

Commercial pure gallium (Ga) metal (99.99%, Alfa Aesar) was applied onto 0.025 mm thick 304-type stainless steel (SS) foils (Alfa Aesar) without any binder or conducting additive. The thickness of Ga film on SS substrate was controlled to be about 1 μm, and the mass of Ga was precisely measured by a microbalance (XS205, Mettler Toledo). Samples were assembled into CR 2025-type coin cells (Hohsen) in an argon-filled glove-box (MBraun) with oxygen and moisture contents less than 0.1 ppm. Li metal foils (99.9%, Sigma Aldrich) were used as the counter electrode (CE). One piece of Celgard 3501 separator soaked in the electrolyte solution consisting of 1M $LiPF_6$ dissolved in a mixture of ethyl carbonate and dimethyl carbonate (EC/DMC, volumetric ratio 1:1) (Novolyte) was used in making the coin cells.

5.3.2 Electrochemical Measurements

Cycling performance of coin cells was evaluated using a potentiostat (VersaSTAT 3, PAR). The cells were galvanostaticlly cycled between 2.0 V and 0.005 V at various rates. During cycling, coin cells were kept in an environmental chamber (Test Equity) with precise temperature controlled at 40, 20, and 10°C, according to the experimental needs. The temperature fluctuation is less than ±0.1°C. In this work charging refers to lithiation and discharging refers to delithiation. Electrochemical Impedance Spectrometry (EIS) was conducted using a potentiostat (2273, PAR) at 40°C and 10°C, respectively. Before each EIS measurement, coin cells were cycled 5 times for stabilization, and then held at 0.890 V until the current was less than 10 nA. The amplitude of the ac signal applied to the electrodes was 8 mV and the frequency was varied from 10^5 to 5×10^{-3} Hz.

5.3.3 Materials Characterization

Before characterization, the cycled cells were disassembled and the WE was washed by DMC (99%, Alfa Aesar). *Ex-situ* x-ray diffraction (XRD) was carried out using a D8 Discover (Bruker AXS) system with Cu Kα radiation (wavelength 1.54 nm). Samples were maintained at 40°C during XRD tests. Scanning electron microscopy (SEM) imaging was performed using a Hitachi S-4300 with an acceleration voltage of 3 kV. A high sensitivity energy dispersive x-ray spectrometer (EDS, PGT) was used to conduct chemical analysis.

5.4 Results and Discussion

The melting point of pure Ga is 29.8°C. Electrochemical cycling tests in this work were held at 40°C to ensure the liquid state of pure Ga. Different from the Ga-Li equilibrium phase diagram [148] and observations of Li in Ga at 415°C [144], three intermetallic phases, Li_2Ga_7, LiGa, and Li_2Ga, form during the electrochemical reaction of Ga with Li at 40°C. The potential-capacity profile in Fig. 5.1 clearly shows four narrow single-phase regions, as well as two-phase regions (plateaus). The theoretical Coulombic capacity in going from Ga to Li_2Ga corresponds to 769 mAh per gram of Ga. The electrode used to generate the data of Fig. 5.1 yielded 700 mAh/g, about 91% of the theoretical value, which indicates that the vast majority of the Ga within the electrode was utilized for reaction with Li. The hysteresis in the potential profile of Fig. 5.1 is not well understood at this time; we suspect that although 50 hours were employed for each of the low-current-density charge and discharge experiments, irreversible phenomena still intrude on the results.

The morphology changes of Ga at various stages of cycling were examined by *ex-situ* SEM, as shown in Fig. 5.2. Before cycling, the applied Ga forms a uniform thin layer on the stainless steel substrate (Fig. 5.2 (a)). After full lithiation, the alloy becomes solid and surface roughness increases (Fig. 5.2 (b)). Through-thickness interconnected cracks form in the alloy primarily during delithiation (Fig. 5.2 (c)). After cycling, most cracks

disappear because the alloy returns to pure Ga, which is a LM at 40°C (Fig. 2d). Thus, cracks are self-healed by the solid-to-liquid transformation of the Ga electrode.

Based on and electrochemical results and *ex-situ* XRD results, and consistent with the previous work of Saint *et al.* [145], the electrochemical reaction of liquid Ga with Li at 40°C can be summarized to good approximation as

$$\text{Lithiation:} \qquad Ga(l) \xrightarrow{Li} Li_2Ga_7 \xrightarrow{Li} LiGa \xrightarrow{Li} Li_2Ga \tag{5.1}$$

$$\text{Delithiation:} \quad Li_2Ga \xrightarrow{-Li} LiGa \xrightarrow{-Li} Li_2Ga_7 \xrightarrow{-Li} Ga(l) \tag{5.2}$$

To further understand the effect of a liquid electrode on the electrochemical performance, the discharging voltage-capacity profiles of (a) liquid Ga (40°C) and (b) solid Ga (21°C) at a C/2 rate are compared in Fig. 5.3. For Ga at 40°C, the $GaLi_x$ compounds are solid at this temperature. After the cell reaches the final plateau near 0.9 V, the electrode is a mixture of solid Li_2Ga_7 and liquid Ga. Because Li diffusion in liquid Ga is much faster than in a solid, Li diffusion in solid Li_2Ga_7 is rate limiting at this stage. After reaching the liquid Ga single phase (starting at about 0.95 V), most of the electrode is liquid and Li diffusion is especially fast. Thus, the cell potential increases to the upper potential limit quickly. For the case of solid Ga at 21°C, after reaching the final potential plateau, the electrode is a mixture of solid Li_2Ga_7 and solid Ga, where Li diffusion is relatively slow. Because of the slow diffusion, the boundary between Ga single phase region and Li_2Ga_7-Ga two-phase region is not clearly defined. Hence, the potential rises much more slowly for the case of solid Ga.

The discharging potential-capacity profiles of Ga LM in the second cycle with various rates are compared in Fig. 5.4 (a). Before each discharging, the cells were charged at C/20 rate to ensure full lithiation of Ga. It is seen that as the discharging rate increases, the potential of each two-phase region increases slightly, which is an indication of polarization due to limited diffusivity of Li in lithiated Ga phases. The total capacity decreases with increasing discharging rate. Ga reaches a capacity of 626 mAh g^{-1} at C/5

discharging rate, which is a standard rate to evaluate the performance of electrode materials. Even at a fast rate of 2C, Ga still delivers a considerable discharge capacity of 560 mAh g^{-1}. The formation of LiGa delivers a capacity of 385 mAh g^{-1} and that of Li_2Ga delivers a capacity of 769 mAh g^{-1}, which is the theoretical maximum capacity of Ga.

The capacity versus cycle number for liquid Ga at 40°C is shown in Fig. 5.4 (b). Efficiency was calculated from the ratio of delithiation to lithiation in each cycle. The charging rate was C/20 and the discharging rate was C/5. A gradual decrease of capacity with cycling is apparent. Commercial lithium salt based electrolytes show fast Li diffusivity and moderate application temperature range compare to other types of electrolytes, such as ionic liquids and solid electrolytes. However, there is a drawback of SEI forming on top of electrodes when the WE is charged (lithiated) to below 0.7 V vs. the Li/Li^+ reaction. The SEI consumes electrolyte, lithium, and electrode material. This SEI layer cannot be dissolved during the reversal electrochemistry process and contributes to irreversible capacity loss. For most negative materials, SEI formation completes in the first few cycles and facilitates Li transportation during subsequent cycling. In this work, because the Ga electrode is in liquid state at the beginning of charging and returns to liquid at the end of discharging at each cycle, the SEI may come off the electrode surface and is no longer stable. Thus, fresh SEI forms during every cycle and brings irreversible capacity loss. This is likely the continuous capacity drop with cycling, as indicated in Fig. 5b. To commercially apply liquid metal with low discharging potential, formation of SEI has to be avoided using other methods, such as using electrolytes that do not form SEI.

Fig. 5.5 shows the EIS measurements of Ga/Li coin cells. The measurements were conducted at 0.890 V, which is Ga single phase region (Fig. 5.1). Both plots are composed of a depressed semi-circle at high frequency range, a short straight line with approximately 45° at medium frequency range, and a steeper ling at high frequency range. The depressed semi-circle is attributed to SEI film and charge-transfer process, the 45° straight line is attributed to the Warburg diffusion process, which is lithium diffusion in active materials, and the steeper line is the onset of finite length diffusion. The

Warburg diffusion happens at a frequency range of 125-3 Hz for 40°C, and 10-0.3 Hz for 10°C, which indicates that the charge-transfer process at high temperature is much faster. The diffusion coefficient can be calculated for the Warburg diffusion stage using [149]

$$D = \frac{1}{2}\left[\frac{V_m}{FA\sigma}\left(\frac{dE}{dx}\right)\right]^2 \tag{5.3}$$

where V_m (cm^3 mol^{-1}) is the molar volume of liquid or solid Ga, F is Faraday constant, A is the area of WE, σ is the linear dependence of Z' or Z'' on $w^{-1/2}$ (w is the angular frequency), dE/dx is the composition dependence of potential, respectively. The value of dE/dx is approximately calculated from potential profile of slow cycling (C/50 rate). The diffusion coefficient of Li in liquid Ga is 1.4×10^{-9} cm^2 s^{-1} for 40°C and is 3.7×10^{-11} cm^2 s^{-1} for solid Ga at 10°C. The two orders of magnitude difference in the diffusion coefficients consistent with the discussion of the voltage-capacity profiles in Fig. 5.3.

5.5 Conclusions

In this chapter, we demonstrate the concept of using low-melting point metal/alloys as lithium-ion battery electrodes. A conceptual picture consistent with all of the experimental observations is given in Fig. 5.6 for self-healing liquid metal electrodes. The liquid metal electrode undergoes crystallization upon lithiation and transforms to a solid electrode. During delithiation the solid phases are transformed to the liquid state. Cracking forms in the electrode mostly during delithiation and can be self-healed by the solid-to-liquid transformation. Since many low melting point alloys exist and can potentially store large quantities of Li, the liquid metal approach demonstrated by liquid Ga may be generalized to many systems of technological significance.

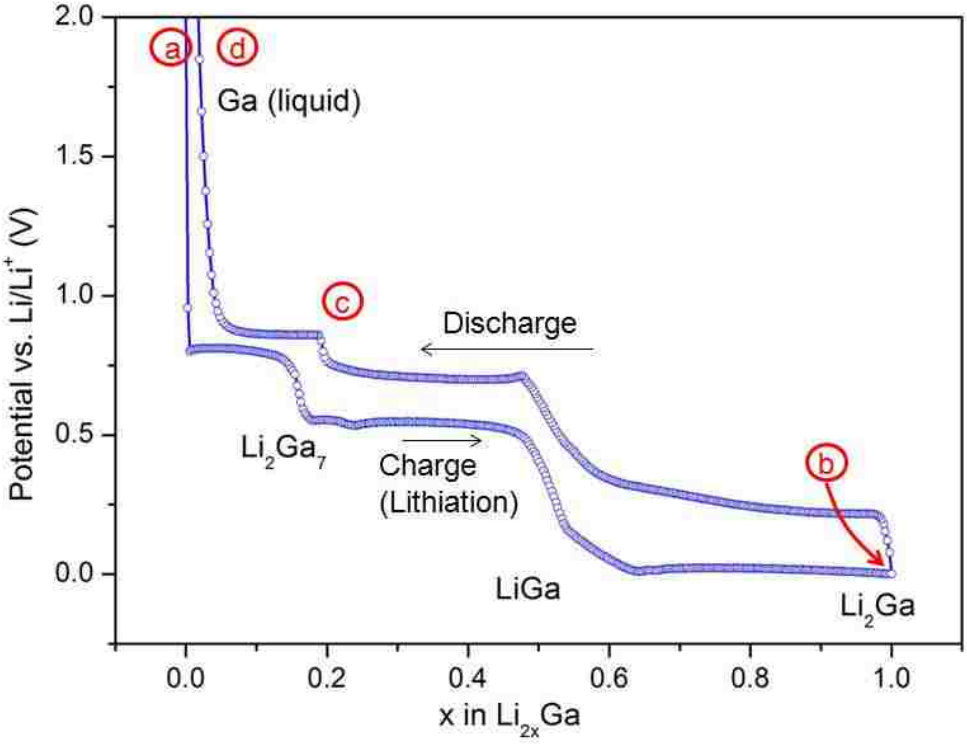

Figure 5.1 Galvanostatic voltage-capacity profile of Ga at 40°C. The cycling rate was C/50. The letters a, b, c, and d correspond to different states for the SEM images of Fig. 5.2.

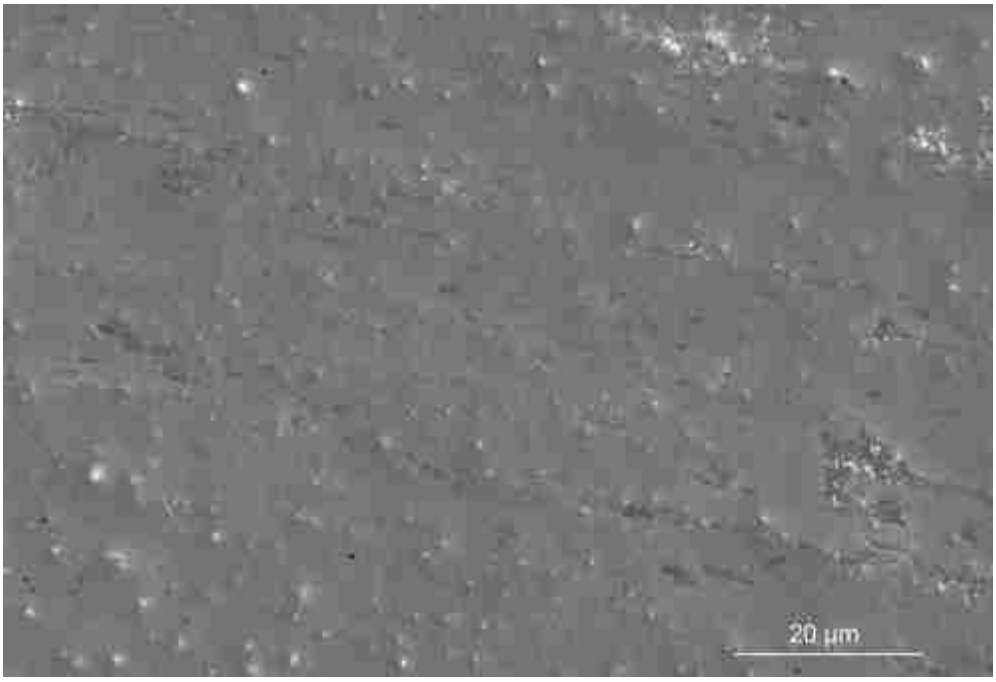

(a)

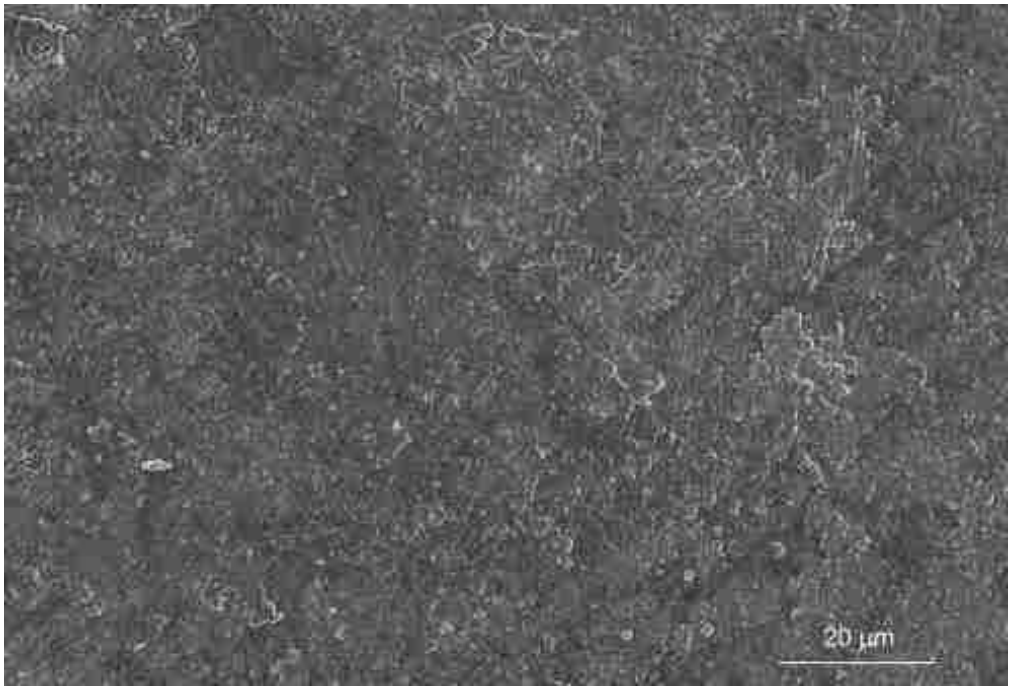

(b)

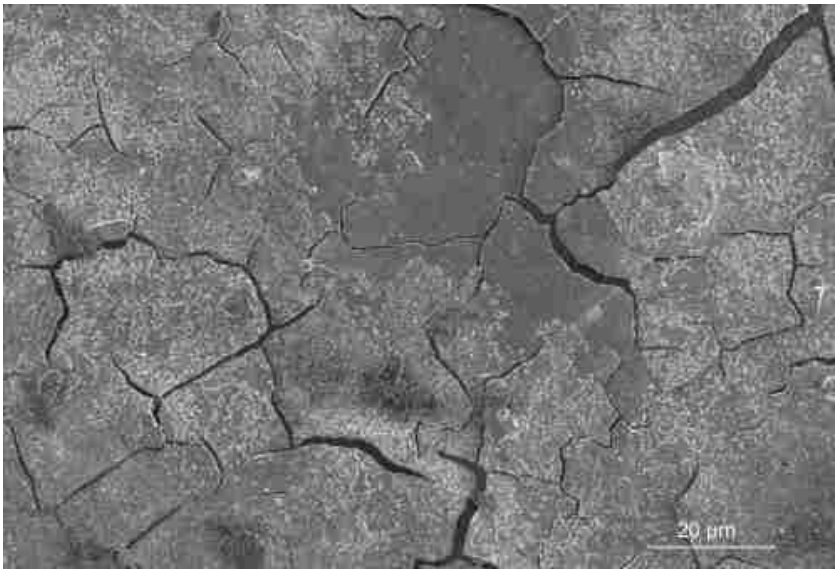

(c)

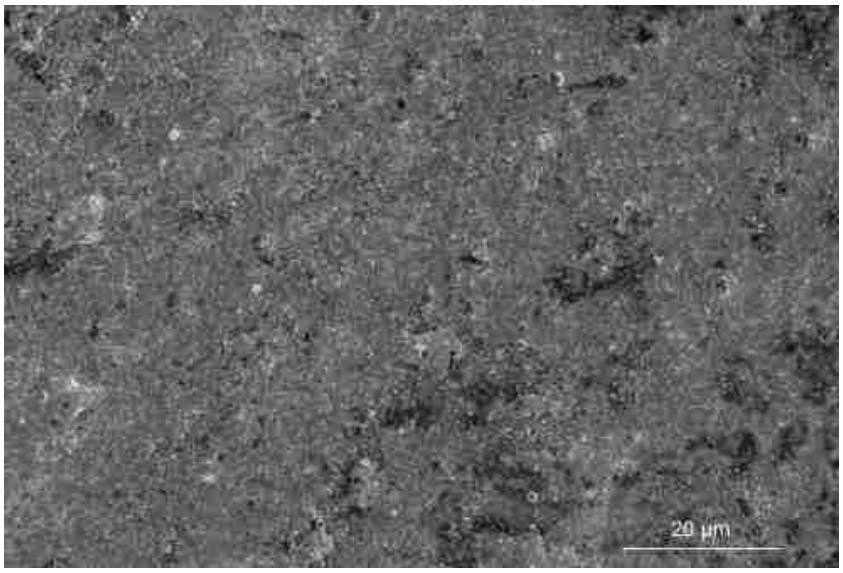

(d)

Figure 5.2 Morphology changes of Ga with cycling. Figures are taken from different states of cycling depicted in Fig. 5.1: (a) Ga before cycling, (b) after full lithiation, (c) cracks formation in Ga-Li alloy during delithiation, and (d) cracks are self-healed by the solid-liquid transformation.

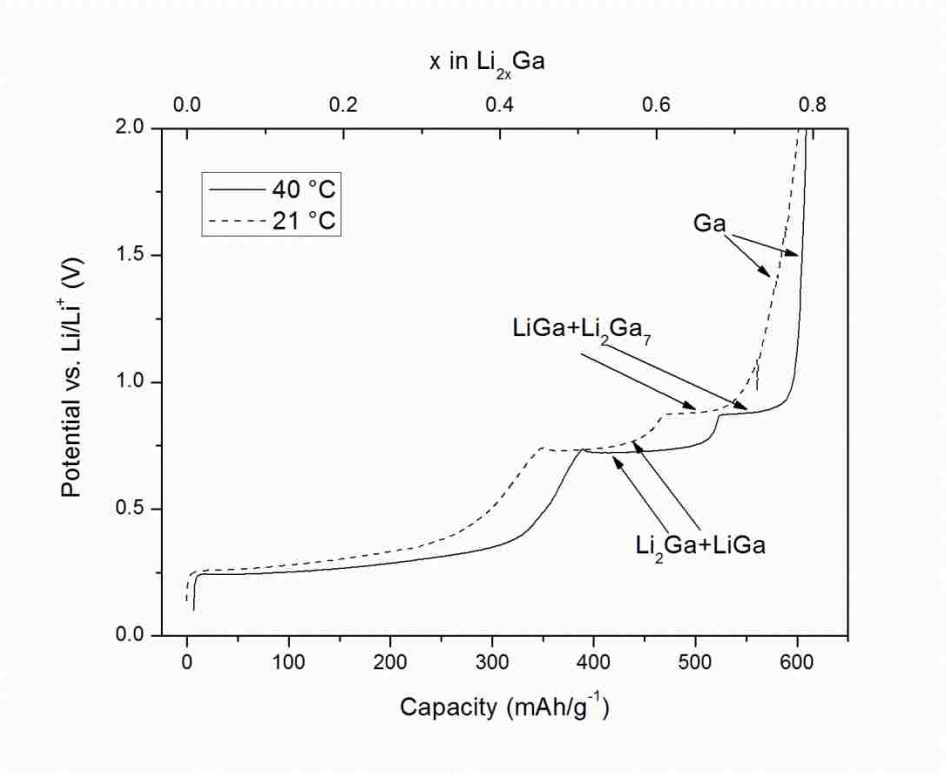

Figure 5.3 Discharging voltage-capacity profiles of liquid Ga (40°C) and solid Ga (20°C) at C/2 rate.

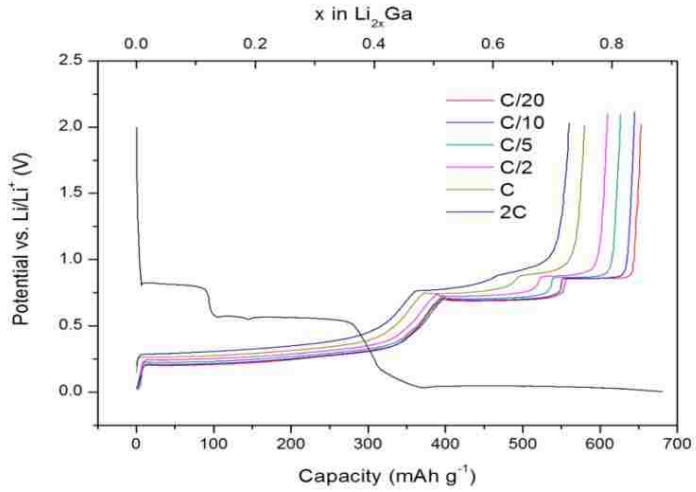

(a)

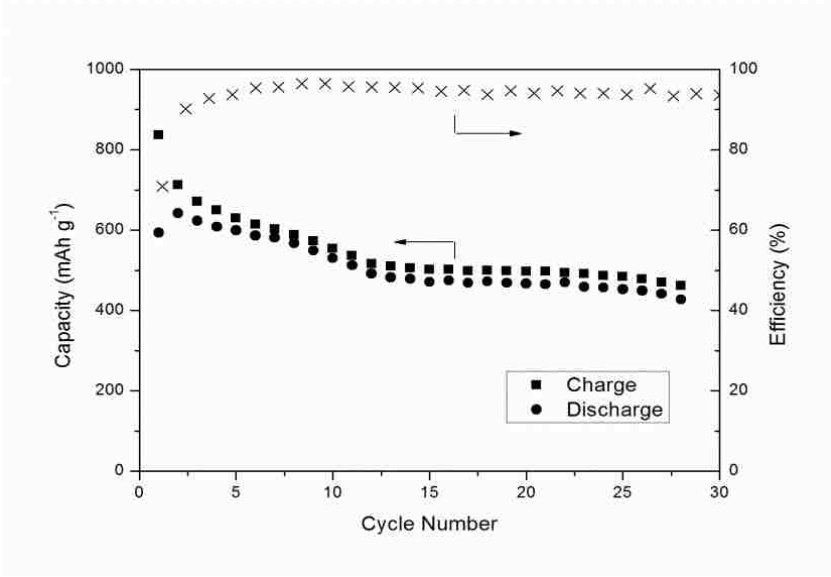

(b)

Figure 5.4 Electrochemical data for the liquid Ga electrode. (a) Rate dependence of discharging voltage-capacity profiles of Ga at 40°C. The cell was charged to 0.005 V at C/20 rate before each discharging. (b) Capacity versus cycle number for liquid Ga at 40°C. The charging rate was C/20, and the discharging rate was C/5.

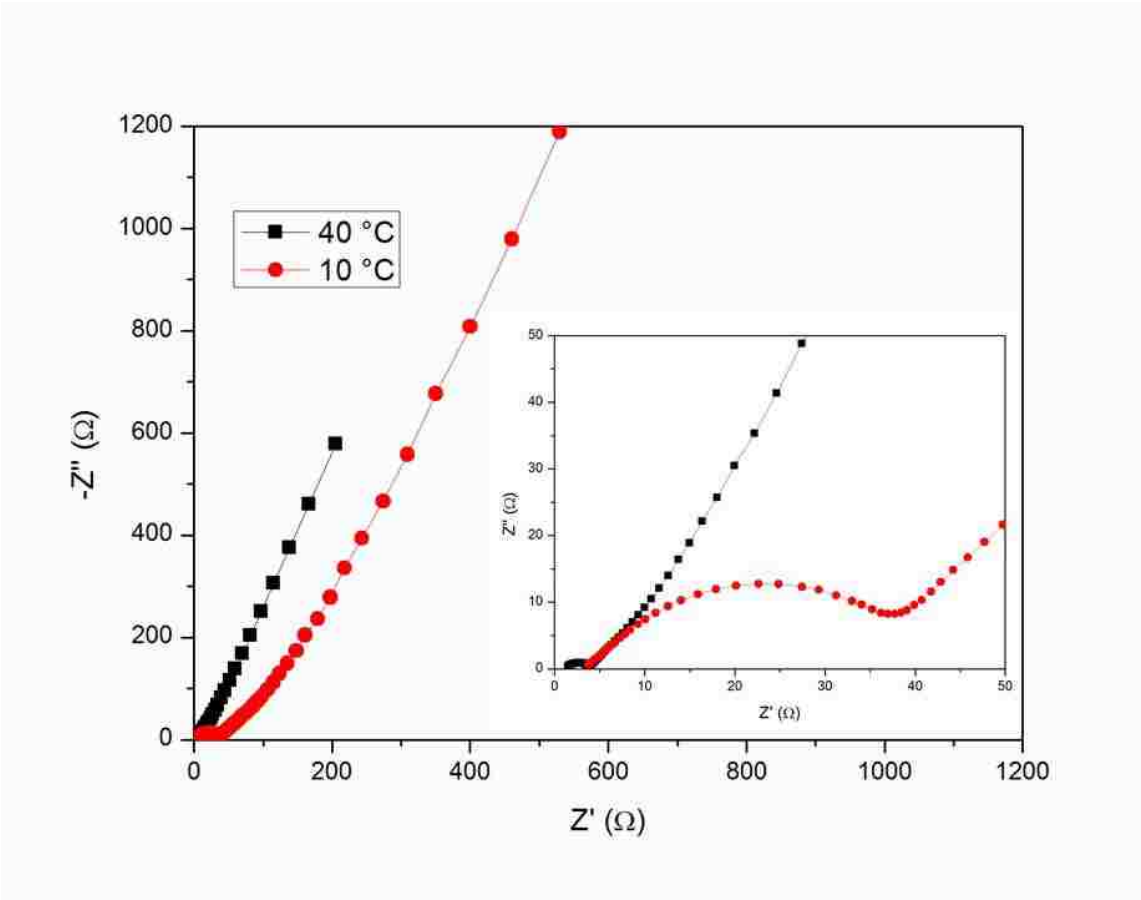

Figure 5.5 Nyquist plot of EIS of liquid (40°C) and solid (10°C) Ga at 0.890 V vs. Li/Li^+. Inset shows the magnified impedance spectra at high frequency.

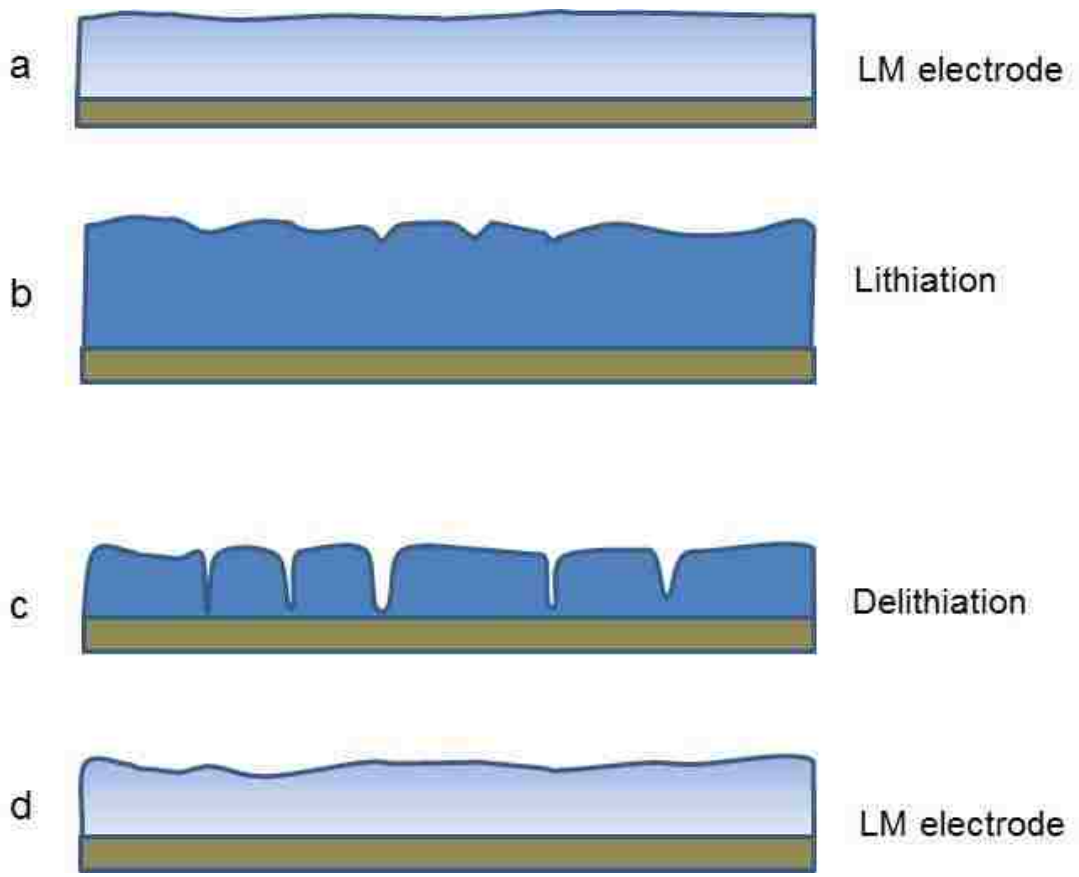

Figure 5.6 Schematic of morphology changes in liquid electrode during cycling. (a) Liquid metal electrode on a solid substrate before electrochemical cycling. (b) Liquid solidifies and expands during lithiation. (c) Cracking occurs in solid mainly during delithiation. (d) Electrode returns to the liquid state during delithiation. Cracks are self-healed by the solid-to-liquid phase transformation.

Chapter 6 Potentiostatic Intermittent Titration Technique (PITT) for Electrodes Governed by Diffusion and Interfacial Reaction [4]

6.1 Summary

The Potentiostatic Intermittent Titration Technique (PITT) is one of the widely used methods for determining the diffusion coefficient in electrochemical materials, such as lithium diffusion in lithium-ion battery electrodes. The conventional PITT analysis neglects interfacial resistance and assumes the system is diffusion controlled. For real electrode systems, however, surface reaction, as well as diffusion, may be rate limiting. In this chapter, we analyze PITT measurements for material systems with finite surface reaction rates. For small amplitude potential steps, we derive analytic solutions for the measured transient current associated with PITT, taking into account the effects of finite surface reaction rates. Using the analytic solutions, the diffusion coefficient, surface reaction rate, and the exchange current density can be determined simultaneously. An example of lithium diffusion in amorphous silicon thin-film electrodes is used to demonstrate the enhanced PITT approach.

6.2 Introduction

The potentiostatic intermittent titration technique (PITT) is a powerful technique to study the thermodynamic and transport properties of materials encountered in electrochemical processes. Because voltage and current can be controlled and measured precisely, PITT has become a commonly used electro-analytical method. Specifically, PITT has been used to measure the diffusion coefficient, D, of solutes in host materials, as well as to obtain quasi-equilibrium voltage-capacity profiles of battery electrodes after it was first developed by Wen *et al.* to study LiAl alloys [149, 150]. Recently, PITT has been widely

---

[4] Reproduced from *The Journal of Physical Chemistry C*, 116 (1): 1472-1478 (2012).

applied to characterize lithium diffusion in various lithium-ion battery (LIB) electrode materials, especially graphite negative electrodes [151, 152] and transition metal oxide positive electrodes [153-159].

The original PITT theory was developed based on a thin-film geometry with diffusion across the thin electrode dimension [150]. Diffusion of only one species was allowed and nucleation of new phases was not considered. Furthermore, the surface reaction rate was assumed to be infinitely fast; i.e., surface reaction resistance was not considered. In practice, it has been challenging to apply PITT to electrochemical systems because many systems do not satisfy all of the assumptions. Thus, several researchers have modified PITT to be applicable to various electrochemical systems. For instance, Markevich *et al*. analyzed the PITT theory in a phase-transformation region which involves slow nucleation, and pointed out that D determined by PITT is less accurate than that by the galvanostatic intermittent titration technique (GITT) [160]. Levi *et al.* studied the PITT of lithium-graphite in the two-phase regions using a two parallel diffusion paths model [161] and a moving boundary model [162]. In addition to phase transformation, it has been realized that the resistance to surface reaction may affect the overall electrochemical behavior. For example, Montella considered possible limitations by insertion reaction kinetics, and developed analytic solutions for PITT [163]. Levi *et al.* developed approximate analytic solutions for PITT by considering Ohmic drop using a generalized dimensionless kinetic parameter ($R_d/R_{external}$) [164], and applied this technique to lithium diffusion in polymer electrode using a two-step refinement method [165]. Churikov *et al.* considered phase transformation and surface resistance for lithium diffusion in multiple spheres, and calculated D of lithium in $LiFePO_4$ by numerical fitting of parameters to experimental data [166]. More recently, Delacourt *et al.* applied PITT to determine the lithium diffusion coefficient in $LiFeSO_4F$ by using an analytic solution of diffusion in spheres with surface reaction resistance [159].

In this chapter, we consider the influence of resistance to surface reaction in analyzing the diffusion of species within a host material during PITT for small potential-step excitations, and we provide analytic solutions to the concentration distribution and

resulting current response. Using this simple analytic model of PITT, one can determine the diffusion coefficient and surface reaction rate (yielding the exchange current density) simultaneously. Using lithium diffusion in thin film amorphous silicon as an example, we show that the diffusion coefficient can be underestimated without considering the finite surface reaction rate. This enhanced PITT model is expected to be applicable to many systems wherein diffusion and surface reaction resistance are both important phenomena.

6.3 Thermodynamics and Electrochemistry

We consider the electrochemical reaction at the electrolyte-electrode interface

$$\mathrm{Li}^{+} + \mathrm{e}^{-} \rightleftharpoons \mathrm{Li}^{0}\big|_{\mathrm{host}} \tag{6.1}$$

representing the lithiation and delithiation of alloy-type LIB electrodes. Using the Butler-Volmer relation, we express the current density i at the electrode surface driven by the surface overpotential η_S [167, 168]

$$i = i_0 \left[e^{\frac{(1-\beta)F\eta_S}{RT}} - e^{\frac{-\beta F\eta_S}{RT}} \right] \tag{6.2}$$

where i_0 is the exchange current density, β is the symmetry factor, F is the Faraday's constant, R is the gas constant, and T is the temperature. The surface overpotential is given by $\eta_S = V - U$, were V is the applied surface potential of the electrode and U is the equilibrium potential. Our primary objective is to measure the Li diffusion coefficient and ensure accuracy by correcting for the intrusion of interfacial resistance on the measurement. Thus, we consider a treatment wherein the potential is stepped from its initial equilibrium value to reach an effective steady state (to be denoted by subscript S) at the new potential value. Since the overpotential in a PITT experiment of the type we consider is small, Eq. (6.2) can be linearized about small η_S giving rise to what is commonly referred to as linear kinetics [167]:

$$i = i_0 \frac{F}{RT}(V - U) \tag{6.3}$$

For sufficiently long times, the current and overpotential tends to zero and $U \to U_S = V$. For the PITT analysis, we consider small potential steps over which the lithium concentration within the host material does not deviate substantially from its initial value. Although i_0 and U are both concentration dependent, they can be approximated, using Taylor expansion about the final (equilibrated, steady state) concentration C_S, as

$$i_0 = i_0|_S - \left.\frac{\partial i_0}{\partial C}\right|_S (C_S - C) + O(C - C_S)^2$$

$$U = U|_S - \left.\frac{\partial U}{\partial C}\right|_S (C_S - C) + O(C - C_S)^2$$

Discarding terms of order $(C - C_S)^2$ and higher, represented by $O(C - C_S)^2$, we obtain the following expression of the current-potential-concentration reaction:

$$i = \left[\mathrm{i_0}|_\mathrm{S} - \left.\frac{\partial \mathrm{i_0}}{\partial \mathrm{C}}\right|_\mathrm{S} (\mathrm{C_S} - \mathrm{C})\right] \frac{\mathrm{F}}{\mathrm{RT}} \left[\mathrm{V} - \left(\mathrm{U}|_\mathrm{S} - \left.\frac{\partial \mathrm{U}}{\partial \mathrm{C}}\right|_\mathrm{S} (\mathrm{C_S} - \mathrm{C})\right)\right] \tag{6.4a}$$

Again, discarding terms of $O(C - C_S)^2$ and higher, and noting $U_S = V$ per the discussion above, we obtain

$$i = -\frac{F}{RT}(i_0|_S) \left.\frac{\partial U}{\partial C}\right|_S (C - C_S) \tag{6.4b}$$

A similar perturbation analysis can be employed to show that for small potential excitations, Fick's law prevails for the Li flux relation. The intercalate flux at the electrode surface is thus given by

$$N = \frac{i}{F} = -D \frac{\partial C}{\partial x}, \qquad x = 0 \tag{6.5}$$

where D is the chemical diffusion coefficient associated with the concentration C_S. Using Eq. (6.4) and (6.5), we can write the interfacial boundary condition as

$$\frac{\partial C}{\partial x} + B\frac{(C - C_S)}{l} = 0, \qquad x = 0 \tag{6.6}$$

where $B \equiv -\frac{li_0|_S \frac{\partial U}{\partial C}\Big|_S}{DRT}$ is the electrochemical Biot number, a dimensionless parameter that is the ratio of diffusion resistance to that of the surface reaction [90, 131], similar to the dimensionless parameters Λ [163, 164, 169], α [170, 171], and j_0 [172] from literature. For a PITT experiment such as what we investigate, B is a fixed value. A large B represents a fast surface reaction compared to diffusion and *vice versa*. Eq. (6.6) is mathematically equivalent to the "radiation boundary condition" in heat transfer problems [173] and surface evaporation to a well stirred environment [174].

6.4 Analytic Solutions

To describe the diffusion of the guest within the host material consistent with the previous discussion, we recognize that for small overpotential excitations and deviations in C, the diffusion equation can be linearized [175] . Thus, we employ Fick's Second Law

$$\frac{\partial C}{\partial t} = D\frac{\partial^2 C}{\partial x^2} \tag{6.7}$$

to describe the solid-state lithium diffusion through the thickness of a slab during the PITT analysis.

Initially, lithium is in equilibrium within the electrode:

$$C = C_0, \qquad 0 \le x \le l, t = 0 \tag{6.8a}$$

The electrode is connected to the current collector at one end ($x = l$) and lithium cannot transport through the electrode and current collector interface. Thus, we have a boundary condition

$$\frac{\partial C}{\partial x} = 0, \qquad x = l, t \ge 0 \tag{6.8b}$$

Using the analogy between heat conduction [173] and diffusion [174], the analytic solutions of concentration profile can be acquired. The solution may comprise error functions or trigonometric series, for short or long times, respectively.

The analytic solution of Eq. (6.7), with initial condition (6.8a) and boundary condition (6.6) and (6.8b), is [173]

$$\frac{C(x,\mathrm{t})-C_0}{C_S-C_0}=1-2B\sum_{n=1}^{\infty}\frac{\cos\left[\lambda_n\left(1-\frac{x}{l}\right)\right]}{(\lambda_n^2+B^2+B)cos\lambda_n}\exp\left(-\lambda_{\mathrm{n}}^2\frac{Dt}{l^2}\right) \tag{6.9}$$

where λ_n (n=1, 2, 3,…) are the positive roots of $\lambda tan\lambda = B$. This solution converges quickly for long times, i.e., $\frac{Dt}{l^2} \gg 1$. The solution can also be expressed in terms of error functions that converge rapidly for short time ($\frac{Dt}{l^2} \ll 1$) [173]:

$$\frac{C(x,t)-C_0}{C_S-C_0}=\mathrm{erfc}\frac{x}{2\sqrt{Dt}}-\exp\left(B\frac{x}{l}+B^2\frac{Dt}{l^2}\right)\mathrm{erfc}\left(\frac{x}{2\sqrt{Dt}}+B\sqrt{\frac{Dt}{l^2}}\right)+\mathrm{erfc}\frac{2l-x}{2\sqrt{Dt}}$$
$$-\exp\left(B\frac{2l-x}{l}+B^2\frac{Dt}{l^2}\right)\mathrm{erfc}\left(\frac{2l-x}{2\sqrt{Dt}}+B\sqrt{\frac{Dt}{l^2}}\right) \tag{6.10}$$

Dimensionless concentration profiles in the electrode for various B values at short times $\frac{Dt}{l^2} \ll 1$ are plotted in Fig. 6.1. When the electrochemical Biot number is large, i.e. B=100 in Fig. 6.1 (a), the surface reaction is fast compared to the diffusion process. The concentration just inside the surface reaches C_S quickly. The concentration profile is similar to the case of infinitely fast surface reaction, as in the original PITT theory developed by Wen *et al* [149, 150].

When the surface reaction rate is comparable with diffusion, i.e. B=5 in Fig. 6.1 (b), the concentration near the surface increases slowly to C_S. The characteristics of the concentration profile are between that which is obtained for constant concentration and constant flux boundary conditions. When the surface reaction is rate-limiting, i.e. B=0.05 in Fig. 6.1 (c), the concentration inside the electrode increase slowly (note the small

range of concentration in Fig. 6.1 (c)). In this case, the problem statement tends to that of constant flux [90, 117, 149, 163]. This can be further demonstrated by examining concentration profiles at longer time.

The electric current is related to the concentration gradient of solute at the electrode-electrolyte interface, as described by Fick's First Law. Neglecting higher-order terms, the short time ($\frac{Dt}{l^2} \ll 1$) transient current under potentiostatic operation corresponds to

$$I(t) = \frac{DQ}{l^2} B \exp\left(B^2 \frac{Dt}{l^2}\right) \operatorname{erfc}\left(B\sqrt{\frac{Dt}{l^2}}\right) \tag{6.11}$$

where we have employed the relation $C_S - C_0 = Q/(zFSl)$ [149]. Here Q is the total charge transferred during the applied potential step $\int_0^\infty Idt$, S is the surface area of the electrode, and z is the charge number of the electro-active species (z=1 for Li^+).

Comparing Eq. (6.11) with the traditional expression for the electric current under PITT operation (Eq. (15) in Reference [149]), we note that the electrochemical Biot number, as well as the diffusion coefficient, enters in the equation for the electric current. Furthermore, when the surface reaction is infinitely fast compared to diffusion, or when B approaches infinity, we have

$$\lim_{B\to\infty} I(t) = \lim_{B\to\infty} \frac{DQ}{l^2} B \exp\left(B^2 \frac{Dt}{l^2}\right) \operatorname{erfc}\left(B\sqrt{\frac{Dt}{l^2}}\right) = \frac{Q}{l}\sqrt{\frac{D}{\pi t}} \tag{6.12}$$

This is the same as the current response to constant surface concentration condition (Eq. (15) in Reference [149]).

Using Eq. (6.11), we plot the dimensionless transient current response vs. $(\frac{Dt}{l^2})^{-1/2}$ with for various B in Fig. 6.2. When B is infinitely large, the transient current for short time is a straight line with the slope equal to $\sqrt{\frac{1}{\pi}}$, consistent with the constant surface

concentration condition. As B decreases, the range of the linear region and the slope of the current vs. $(\frac{Dt}{l^2})^{-1/2}$ both decrease. Since the diffusion coefficient D is determined by the slope of the linear region in the original PITT theory, the diffusion coefficient D may be underestimated using the linear fitting method when B is finite or interfacial resistance is large, which is consistent with previous publications [163, 176].

The concentration profile in the electrode with different B at long times $\frac{Dt}{l^2} \gg 1$ is plotted in Fig. 6.3. When the surface reaction rate is facile relative to the diffusive process (B=100 in Fig. 6.3 (a)), the concentration just inside the surface reaches the maximum concentration quickly, and the concentration profile is close to constant concentration condition. The concentration in the electrode increases quickly and the dimensionless concentration reaches 0.9 when $\frac{Dt}{l^2}$ is greater than 1.1. Similar trends in concentration profiles can be found in Fig. 4 of Ref. [163], which illustrated the concentration evolution under diffusion controlled processes [163]. When surface reaction is comparable to the diffusion, i.e. B=5 in Fig. 6.3 (b), the concentration in the electrode increases slowly. The concentration just below the surface is smaller than unity at $\frac{Dt}{l^2}$=2, and the entire dimensionless concentration does not reach 0.9 until $\frac{Dt}{l^2}$ is greater than 1.4. When surface reaction is the rate-limiting process (B=0.05 in Fig. 6.3 (c) and 6.3 (d)), the concentration inside the electrode increases slowly. This is similar to the concentration profiles for galvanostatic (constant flux) operations [90, 117, 149, 163]. Under this condition, concentration in the electrode increases quasi-uniformly to reach the maximum value (Fig. 6.3 (d)).

Substituting Eq. (6.9) into equation (6.5) and neglecting the higher-order terms, we find that the transient current at large time ($\frac{Dt}{l^2} \gg 1$) can be expressed as

$$I(t) = \frac{2QD}{l^2} \frac{B^2}{(\lambda_1^2 + B^2 + B)} \exp\left(-\lambda_1^2 \frac{Dt}{l^2}\right) \tag{6.13}$$

Rearrangement of Eq. (6.13) yields

$$\ln[I(t)] - \ln\left(\frac{2QD}{l^2}\right) = \ln\left[\frac{B^2}{(\lambda_1^2 + B^2 + B)} exp\left(-\lambda_1^2 \frac{Dt}{l^2}\right)\right] \quad (6.14)$$

Fig. 6.4 shows the plot of $\ln[I(t)] - \ln\left(\frac{2QD}{l^2}\right)$ vs. $\frac{Dt}{l^2}$ for various B values. The slope of the line is $-\frac{\pi^2}{4}$ when B is infinite. With decreasing B, the slope of the linear fit of the curve decreases. The intercept of the line is 0 only when B is infinity. With decreasing B, the intercept of the line is negative. Thus, D can be underestimated by using the slope or intercept of $\ln[I(t)]$ vs. t plot without considering the effect of surface reaction rate (cf. equation (16) in Reference [149]), in agreement with previous publications [163, 176].

As $B \to \infty$, $\lambda_n \to \frac{2n-1}{2}\pi$, and we have

$$\lim_{B\to\infty} I(t) = \lim_{B\to\infty} \frac{2QD}{l^2}\left[\frac{B}{B+1}\exp\left(-\lambda_{\mathrm{n}}^2 \frac{Dt}{l^2}\right)\right] = \frac{2QD}{l^2}\exp(-\frac{\pi^2}{4}\frac{Dt}{l^2}) \quad (6.15)$$

Eq. (6.15) is the same as current response to constant concentration condition at long time (Eq. (16) in Reference [149]).

According to Eq. (6.14), D and B can be determined simultaneously from the linear plot of $\ln I$ vs. t by solving three equations:

$$-\lambda_1^2 \frac{D}{l^2} = \text{slope}$$

$$\ln[\frac{2B^2QD}{(\lambda_1^2 + B^2 + B)l^2}] = \text{intercept on the } \ln I \text{ axis when } t = 0$$

$$\lambda_1 tan\lambda_1 = B \quad (6.16)$$

6.5 Experimental

6.5.1 Sample Preparation

Amorphous Si thin films were deposited on Cu foil by means of E-beam evaporation. The Si working electrode (WE) was assembled into CR2032 coin cell with pure lithium

metal (Alfa Aesar) as the counter electrode (CE). One piece of Celgard 3501 separator soaked with electrolyte (1 M $LiPF_6$ salt in 1:1 ratio of ethylene carbonate:dimethyl carbonate) was used in the coin cell.

6.5.2 Electrochemical Characterization

Electrochemical tests were conducted using a Bio-Logic potentiostat (VMP3) at room temperature. Before the PITT experiment, the coin cell was galvanostatically cycled four times between 1.0 and 0.3 V in order to form a substantially stable SEI layer and remove the influence of side reactions that are prevalent during the first couple cycles. The lower voltage limit of 0.3 V was chosen to ensure shallow cycling and prevent cracking in the Si thin films [177], which may affect diffusion behavior. Within each half cycle, the capacity was measured to be less than 20% of the theoretical capacity of Si. The PITT experiment was carried out during discharging from 0.395 V to 0.390 V. Voltage was applied on the cell until the current fell below the equivalent of 1 mA g^{-1} (about C/3600). The 1000 and 100 nm thick Si films were used for short time and long time evaluation of PITT, respectively.

6.6 Results and Discussion

The diffusion coefficients D calculated by different methods are compared in Table 6.1. For testing the short time non-linear fitting method, PITT data were obtained during $t <$ 400 s (Fig. 6.6) using a 1,000 nm thick Si film. For testing the long time linear fitting method, PITT data were collected during $t >$ 600 s (Fig. 6.7) using a 100 nm thick Si film. The data points displayed are much fewer than the actual experimental data points so that the data and the fit can be discerned. For short times, D is calculated by a least-square nonlinear fitting method (Curve Fitting Toolbox in Matlab) according to Eq. (6.11) and linear fitting according to Eq. (15) in Reference [149]. For long times, D is calculated by solving Eq. (6.16) with parameters obtained from Fig. 6.7. As shown in Table 6.1 the diffusion coefficient of lithium in amorphous silicon at 0.390 V varies from 1.0×10^{-13} to 1.4×10^{-13} $cm^2\,s^{-1}$. The electrochemical Biot number B is calculated to range from 45 to 50,

which shows that both surface reaction and diffusion contribute to the system behavior. The lithium diffusion coefficient in amorphous Si using the traditional PITT theory are calculated to range from be 0.7×10^{-13} to 1.1×10^{-13} cm^2 s^{-1}, close to values reported previously [178-180]. The lithium diffusion coefficient calculated by either Eq. (6.10) or Eq. (6.16) is larger than that calculated by the traditional short and long time linear fitting methods. The results suggests that the diffusion coefficient may be underestimated using the traditional methods when surface reaction rate is not infinitely fast or B is finite. Because the electrochemical Biot number is relatively large here, the system is biased to diffusion control, and the diffusion coefficients obtained considering the surface reaction rate are close to those using traditional methods. The diffusion coefficient calculated using traditional methods may be much smaller if the surface reaction is slow or if, more generally, B is smaller, such as can be the case for graphite electrodes [90].

Furthermore, the exchange current density $i_0|_S$ can be calculated from the definition of the electrochemical Biot number in Eq. (6.6). Note that the dependence of equilibrium potential on concentration, $\left.\frac{\partial U}{\partial c}\right|_S$, can be obtained separately by slow (quasi-equilibrium) cycling. In this work, we applied C/300 cycling of Si vs. Li to obtain the equilibrium potential profile. The exchange current density of silicon electrodes during lithiation at 0.390 V is calculated to range from 0.07 to 0.13 mA cm^{-2}. It is interesting to note that this is nearly the same value as was obtained in the GITT experiment reported in Fig. 5 of Reference [181] for a lithiated carbon electrode (approximately 0.1 mA cm^{-2} for fractional occupancies of lithium ranging from 0.3 to 0.75) [181].

The surface reaction rate can be affected by the charge-transfer processes at the surface of the LIB electrodes. For negative electrodes of LIBs, it can also be affected by the presence of the solid electrolyte interphase (SEI). Properties of the SEI, including the chemical composition, thickness, stability, and mechanical properties, vary with electrode materials and the electrochemical environment. Surface modification, such as atomic layer deposition (ALD) coating and surface fuctionalization, may change the surface reaction rate. In general we expect the surface reaction resistance to affect the

electrochemical behavior of electrodes, as well as the transient current response to potential steps.

6.7 Conclusions

We analyze the diffusion equation suitable for PITT when surface reaction resistance is important and derived analytic solutions for the concentration and transient current response. This treatment allows one to capture the additional influence of reaction resistance, relative to the conventional PITT analysis, in a single dimensionless group: the electrochemical Boit number B, representing the ratio of diffusion resistance to that of the surface reaction. We show that the diffusion coefficient D can be underestimated using the traditional linear (I vs. $t^{-1/2}$ for short time) and exponential fitting ($\ln I$ vs. t for long time) methods without considering the influence of a finite surface reaction rate. Using this new method, we show that one can determine the diffusion coefficient and surface reaction rate simultaneously from a PITT measurement, as well as the exchange current density. We implement the modified PITT to examine lithium diffusion in amorphous silicon thin-film electrodes. The modified PITT is applicable to lithium-ion battery electrodes, as well as other electrochemical systems wherein the measurement of diffusion and kinetic parameters characterizing surface reaction resistance (e.g., the exchange current density) are of interest.

6.8 Appendix

6.8.1 List of Symbols

B	electrochemical Biot number
C	molar concentration
D	diffusion coefficient of the solute

e^-	electron
F	Faraday's constant
I	current
i	current density
i_0	exchange current density
Li^+	lithium ion
l	thickness of electrode
Q	total charge transferred during a potential step
S	surface area of electrodes
t	time
U	equilibrium potential
V	surface potential
x	thickness position

z	charge number of the electro-active species
β	symmetry factor
η_S	Surface overpotential
λ_n	nth positive roots of $\lambda tan\lambda = B$
τ	dimensionless time

6.8.2 Derivation of The Electrochemical Biot Number Using Equivalent Circuit

The electrochemical Biot number B can also be derived from a point of view of equivalent circuit, which was used to estimate the interfacial kinetics occurring on ion-insertion electrodes [163, 164]. Neglecting the limitations of mass transport in the electrolyte, the resistance of an lithium-ion battery typically consists of three parts: the charge transfer resistance R_{ct}, the resistance due to Ohmic drop R_{Ω}, and the diffusion resistance R_{d}.

The interfacial charge-transfer resistance can be expressed as [163, 169]

$$R_{\mathrm{ct}} = -\frac{1}{FA\dfrac{\partial \nu}{\partial U}} \tag{6.17}$$

where F is Faraday's constant, ν is the lithium ion insertion reaction rate, A is the surface area of the electrode, and U is the surface equilibrium potential. $\frac{\partial \nu}{\partial U}$ is particle derivative of insertion reaction rate ν with respect to surface equilibrium potential U.

The diffusion resistance can be expressed as [163, 169]

$$R_{\mathrm{d}} = -\frac{l}{FAD\left.\frac{\partial C}{\partial U}\right|_S} \tag{6.18}$$

where l is the thickness of the electrode, D is the diffusion coefficient, and C is the concentration in the electrode. The insertion reaction rate ν is related to the Bulter-Volmer equation (Eq. 6.2) by

$$i = F\nu = i_0\left[e^{\frac{(1-\beta)F(V-U)}{RT}} - e^{\frac{-\beta F(V-U)}{RT}}\right] \tag{6.19}$$

where i is the current density, i_0 is the exchange current density, β is the symmetry factor, R is the gas constant, and T is the temperature. The surface overpotential is given by $V-U$, were V is the applied surface potential of the electrode. Assuming that the overpotential is small, we can expand Es. (6.19) and obtain

$$\nu = i_0|_S\,\frac{V-U}{RT} \tag{6.20}$$

Thus,

$$R_{ct} = \frac{i_0|_S}{FART} \tag{6.21}$$

Using Eq. (6.18) and (6.21), the electrochemical Biot number B, which is defined in Eq. (6.6) in the main text, can be written as

$$B \equiv -\frac{li_0|_S\left.\frac{\partial U}{\partial C}\right|_S}{DRT} = \frac{R_d}{R_{ct}} \tag{6.22}$$

where we have used $\left.\frac{\partial U}{\partial C}\right|_S = 1/\left.\frac{\partial C}{\partial U}\right|_S$. The electrochemical Biot number is, therefore, the same as the dimensionless parameter $\Lambda = \frac{R_d}{R_{ct}+R_\Omega}$ used by Montella [163] and Vorotyntsev et al [164], if the resistance due to Ohmic drop R_Ω is 0. As a result, if R_Ω is 0,

the expressions of transient current Eqs. (6.11) and (6.13) are equivalent to Eqs. (39) and (43) in Reference [163].

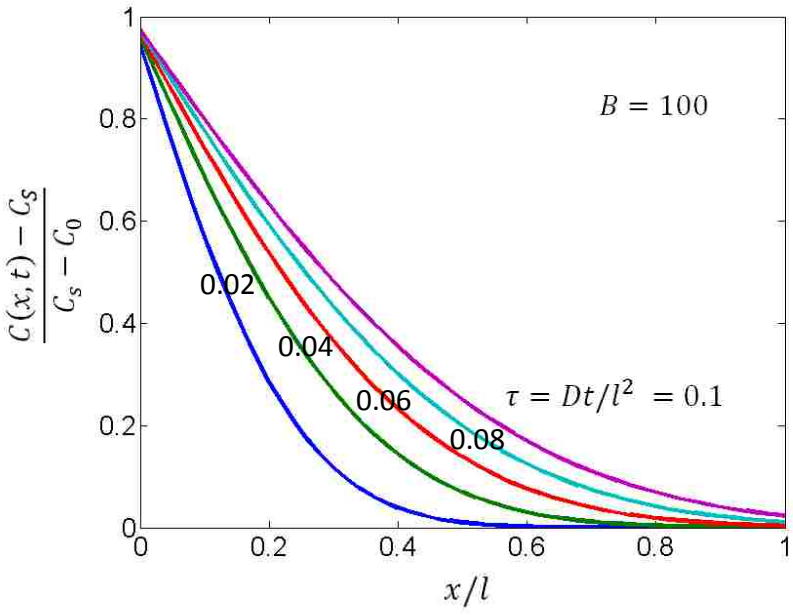
$B = 100$
$\tau = Dt/l^2 = 0.1$
0.02
0.04
0.06
0.08
$\frac{C(x,t) - C_S}{C_s - C_0}$
x/l

(a)

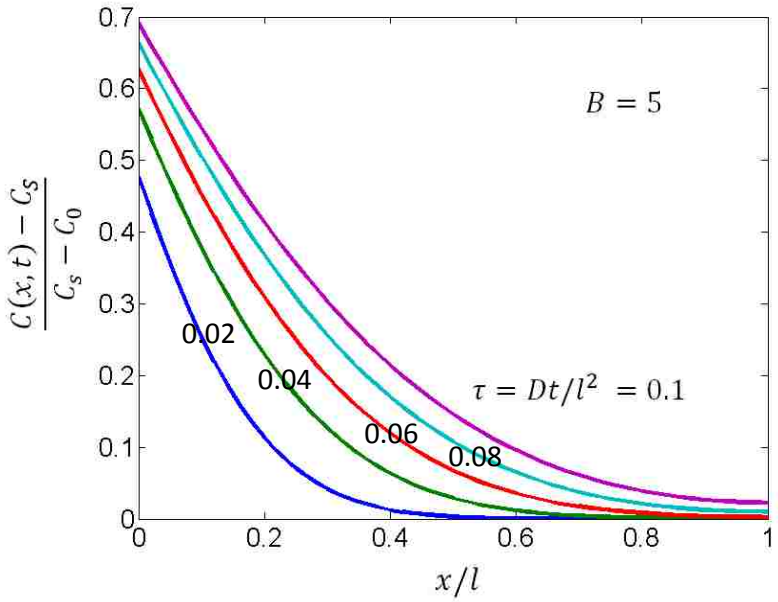
$B = 5$
$\tau = Dt/l^2 = 0.1$
0.02
0.04
0.06
0.08
$\frac{C(x,t) - C_S}{C_s - C_0}$
x/l

(b)

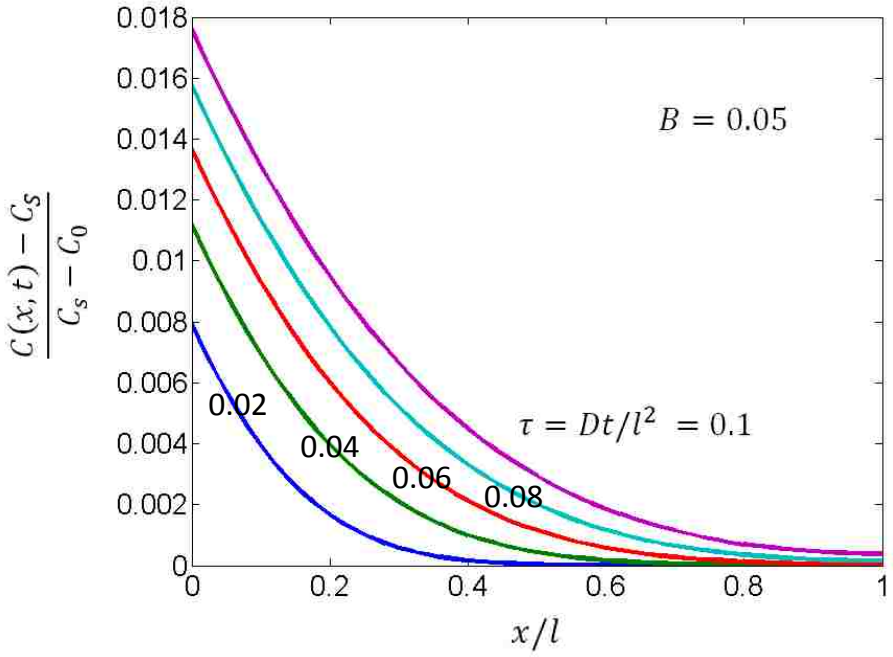

(c)

Fig. 6.1 Concentration profiles under PITT operation at short times, i.e. $\frac{Dt}{l^2} \ll 1$, for different electrochemical Biot numbers. (a) B=100. (b) B=5. (c) B=0.05.

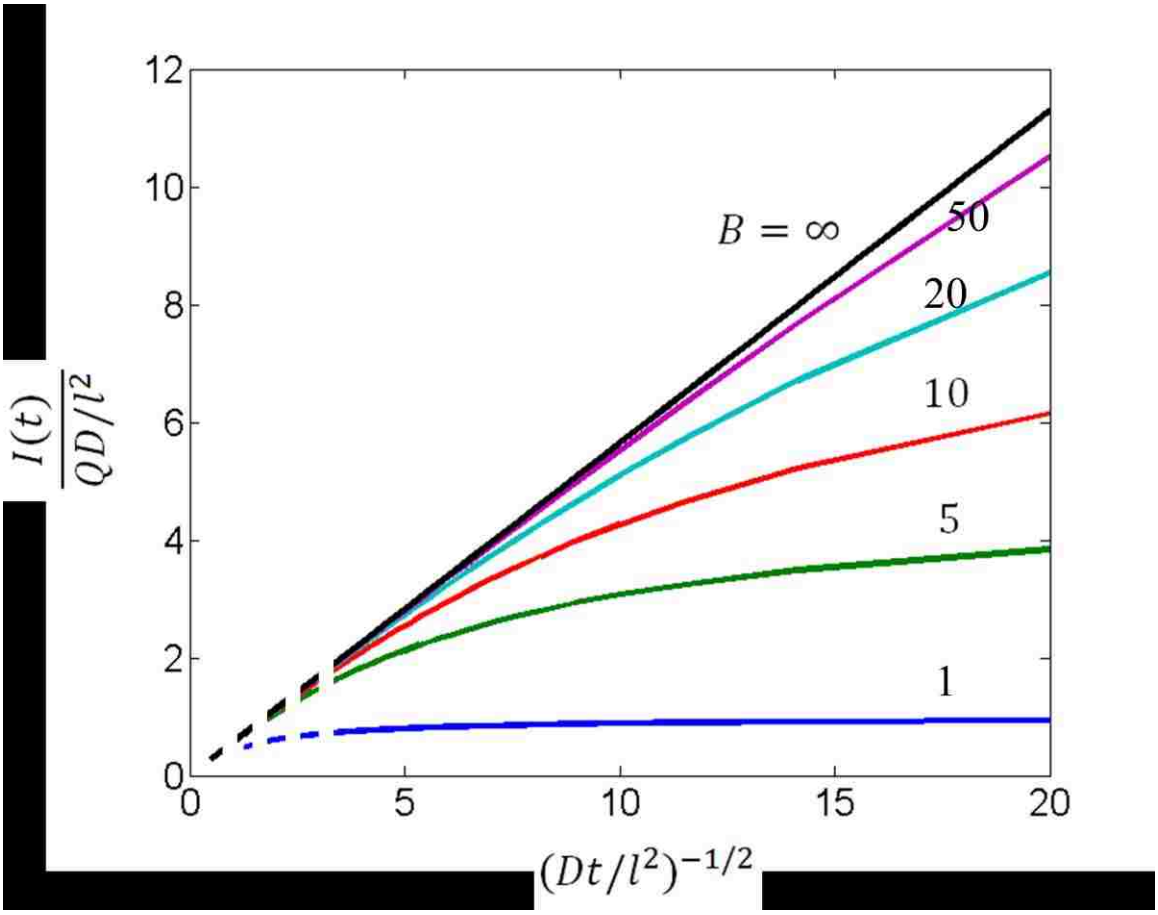

Fig. 6.2 Dimensionless transient current vs. time at short times with various electrochemical Biot numbers.

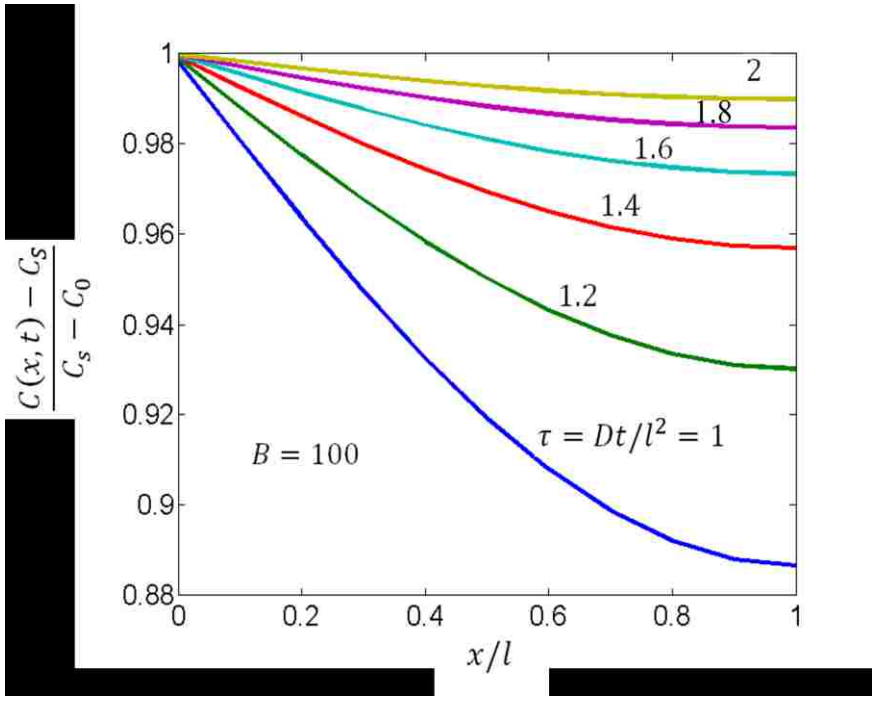
$\frac{C(x,t)-C_S}{C_s-C_0}$
1
0.98
0.96
0.94
0.92
0.9
0.88
0
0.2
0.4
0.6
0.8
1
x/l
2
1.8
1.6
1.4
1.2
$B = 100$
$\tau = Dt/l^2 = 1$

(a)

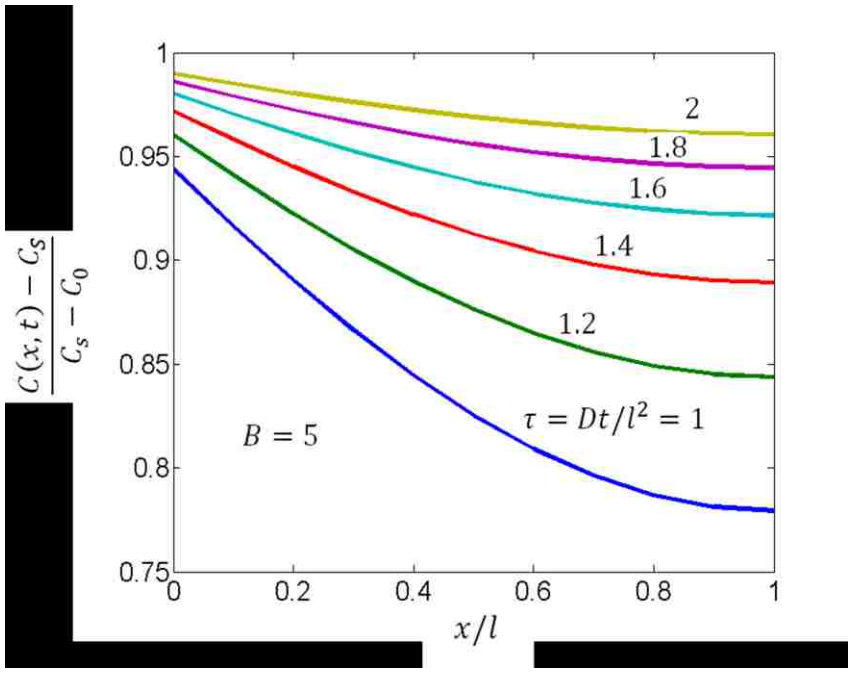
$\frac{C(x,t)-C_S}{C_s-C_0}$
1
0.95
0.9
0.85
0.8
0.75
0
0.2
0.4
0.6
0.8
1
x/l
2
1.8
1.6
1.4
1.2
$B = 5$
$\tau = Dt/l^2 = 1$

(b)

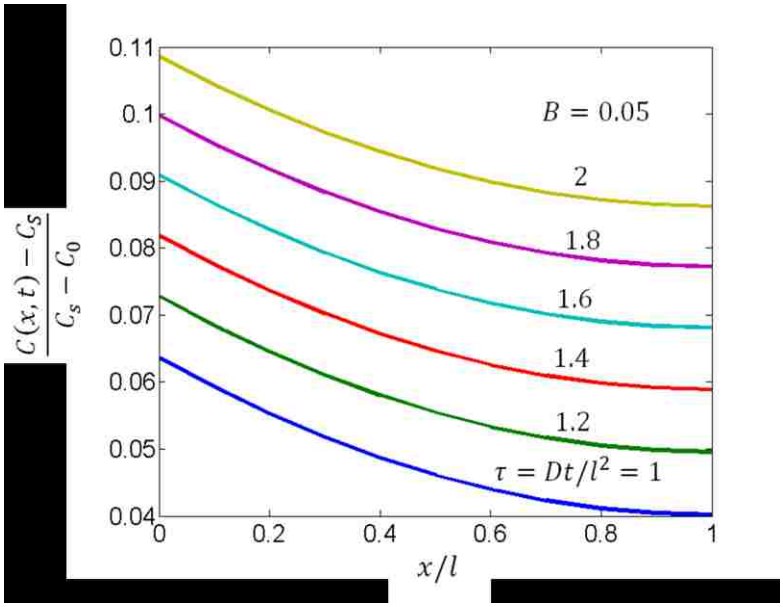

(c)

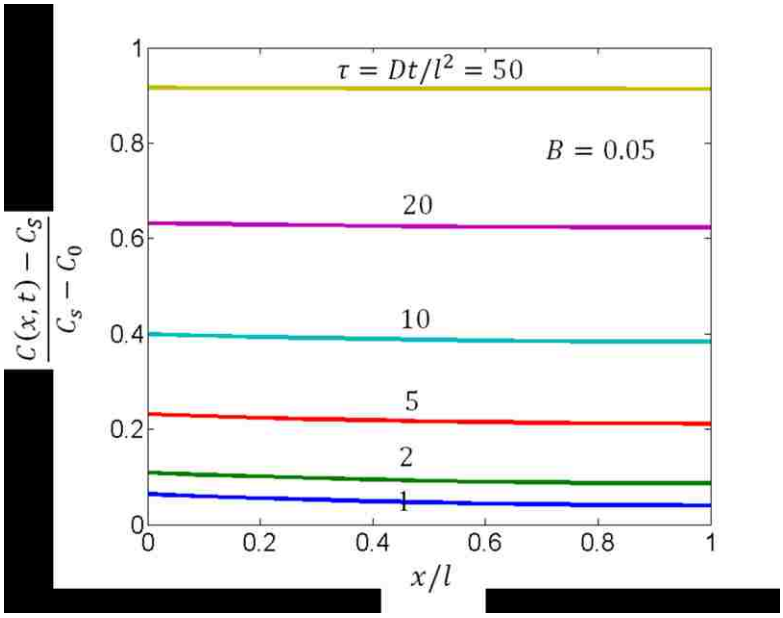

(d)

Fig. 6.3 Concentration profiles under PITT operation at long times, i.e. $\frac{Dt}{l^2} > 1$, for different electrochemical Biot numbers. (a) B=100. (b) B =5. (c) B =0.05.

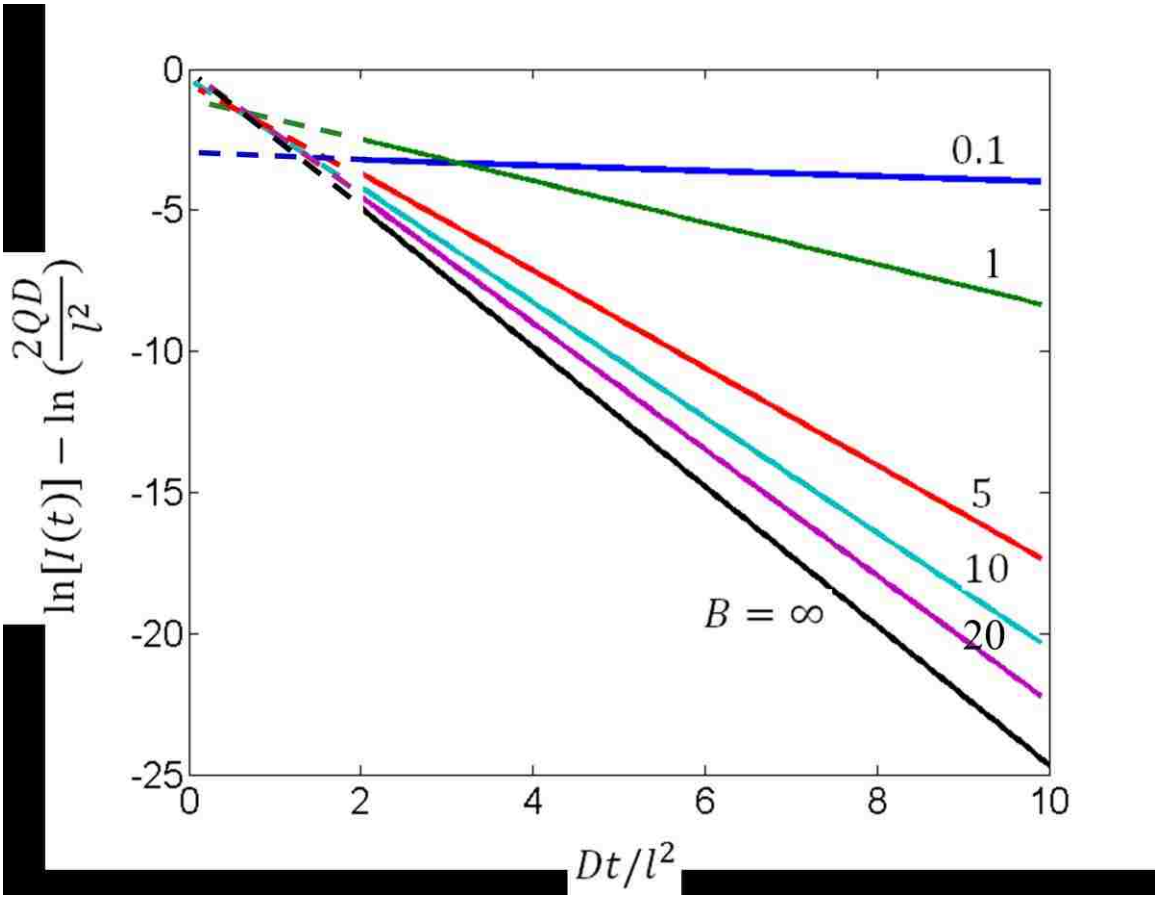

Fig. 6.4 Dimensionless transient current vs. time at long times with various electrochemical Biot numbers.

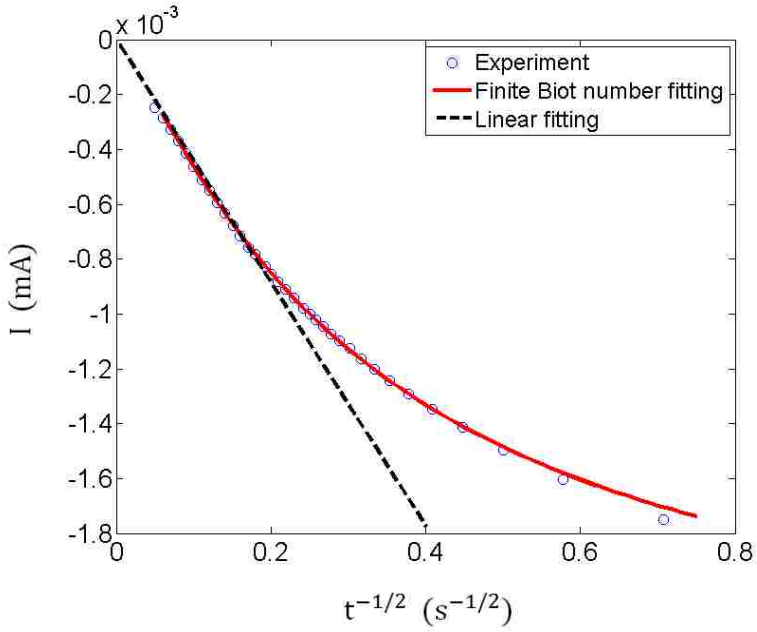

Fig. 6.5 Plot of transient current vs. $t^{-1/2}$ at short time.

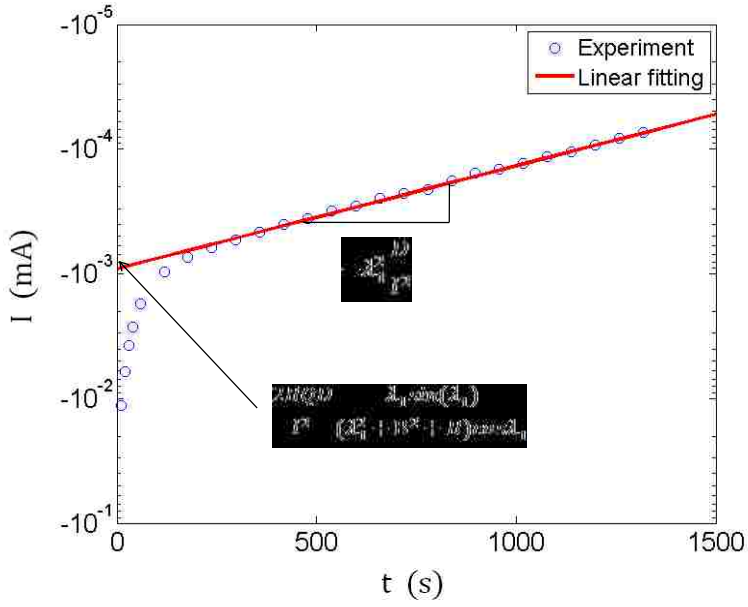

Fig. 6.6 Exponential dependence of current on time at long time.

Table 6.1 Diffusion coefficient of Li in silicon calculated by different methods.

Method	D ($cm^2\ s^{-1}$)	B
Short time (Eq. 6.10)	1.4×10^{-13}	49.4
Short time linear fitting (Eq. 15 in Ref. [149])	1.1×10^{-13}	
Long time (Eq. 6.17)	1.0×10^{-13}	45.7
Long time (Eq. 16 in Ref. [149], slope)	7.7×10^{-14}	
Long time (Eq. 16 in Ref. [149], intercept)	7.7×10^{-14}	

Chapter 7 Potentiostatic Intermittent Titration Technique (PITT) for Electrodes Governed by Diffusion and Interfacial Reaction

7.1 Summary

The potentiostatic intermittent titration technique (PITT) is an electroanalytical method that has been widely used to study diffusion of solutes (such as lithium) in electrode materials. Here, we extend the conventional PITT method to account for finite interfacial reaction kinetics and derive analytic equations for electric current under PITT operations. Using the modified PITT, the lithium diffusion coefficient in host materials and the interfacial reaction kinetics can be determined simultaneously. We demonstrate this modified PITT by an example of lithium diffusion in graphite (mesocarbon microbeads, MCMB) and show the improvements of the modified PITT theory over the conventional PITT for investigating the kinetics of electrodes comprising spherical particles.

7.2 Introduction

The potentiostatic intermittent titration technique (PITT), originally proposed by Huggins *et al.* for studying Li diffusion in Li-Al alloy [149, 150], has been widely used in studying diffusion and thermodynamics of lithium-ion batteries (LIBs), especially for measuring the lithium diffusion coefficients in LIB electrodes. [157, 159, 161, 162, 166, 182-185] In developing the original theory, several assumptions were made for the electrochemical system, including:

(1) Diffusion of only one species occurs in the system and the diffusion coefficient is a constant within the applied potential range.

(2) Diffusion occurs across the thinnest dimension of a dense electrode with a slab geometry.

(3) There is no interfacial reaction resistance at the electrode-electrolyte interface.

(4) There is no phase transformation related kinetics.

For solid-state electrochemical systems such as LIBs, experiments have to be designed carefully to meet all the assumptions above. For example, dense thin-film electrodes need to be used, allowing Li diffusion along the thickness direction (assumption 2 above). The applied voltage range should be small, insuring diffusion in a single phase region with a constant diffusion coefficient (assumptions 1 and 4 above).

In order to apply PITT to a large range of experimental conditions, researchers have applied modifications to the original PITT theory. For example, Levi *et al.* modified PITT to study the lithium-graphite system in two-phase regions using a parallel path diffusion model [161] and a moving boundary model. [162] Churikov *et al.* proposed an approach to describe the transport process during PITT operation considering surface reaction and phase transformation, and studied Li diffusion in $LiFePO_4$ by simulating experimental data. [166] Montella discussed PITT with slow interfacial kinetics and Ohmic drop on electrodes using an equivalent circuit approach. He introduced a dimensionless parameter Λ, which is the ratio of diffusion resistance to the resistance of charge transfer and Ohmic drop, [163] and discussed the effects of Λ on errors in determining the diffusion coefficient. [176] Deiss discussed the voltage dependence of the PITT measured diffusion coefficients and proposed that this dependence may be a result of neglecting the interfacial kinetics. [186] Levi *et al.* developed approximate analytic solutions for PITT by considering Ohmic drop using an equivalent circuit approach and introduced a dimensionless kinetic parameter ($R_d/R_{external}$). [164] They applied their technique to lithium diffusion in polymer electrodes with a two-step refinement method. [165] Recently, we proposed a modified PITT for electrodes governed by diffusion and interfacial reaction kinetics, and applied this method to study Li diffusion in amorphous Si thin film electrodes. [187]

Since most of the practically used electrodes are made of powders, the original PITT theory for slab geometry may not be applicable to lithium diffusion along the radial direction of the particles. Deiss noticed this problem and suggested that the diffusion

coefficients obtained for composite electrodes using the original PITT theory may be incorrect. [186] More recently, Delacourt *et al.* applied PITT to determine the lithium diffusion coefficient in $LiFeSO_4F$ particles by using an analytic solution of diffusion in spheres. [159]

In this chapter, we develop a PITT model for lithium diffusion in spherical particles with finite electrode-electrolyte interfacial reaction rates. With the analytic solutions for transient current, the diffusion coefficient and interfacial reaction kinetics can be simultaneously measured. With graphite (mesocarbon microbeads, MCMB) as an example, we show that this modified PITT can be used to study the lithium diffusion in LIB electrode materials consisting of spherical particles.

7.3 Theory

7.3.1 Governing Equations and Analytic Solutions

We consider a diffusion process in an electrode consisting of homogeneous spherical particles of radius R. Lithium diffusion in the lithium salt based liquid electrolyte is often much faster compared to the diffusion in electrode materials [188], and we assume that the diffusion process is identical in each single particle under electrochemical operation. Assuming that the diffusion coefficient D is a constant during the diffusion process and there is no phase transformation kinetics involved, assumptions that are valid for small potential changes in single phase regions, the diffusion equation for a sphere is given by [174]

$$\frac{\partial C}{\partial t} = D\left(\frac{\partial^2 C}{\partial r^2} + \frac{2}{r}\frac{\partial C}{\partial r}\right) \tag{7.1}$$

where C is concentration, and r is the radial position ($0 < r < R$). The initial and boundary conditions corresponding to PITT operation, i.e., potentiostatic variation within a small range, are

$$C = C_0, \qquad \text{for } t = 0 \text{ and } 0 < r < R \tag{7.2a}$$

$$C = \text{finite}, \qquad \text{for } t > 0 \text{ and } r = 0 \tag{7.2b}$$

$$\frac{\partial C}{\partial r} + \frac{B}{R}(C - C_S) = 0, \qquad \text{for } t > 0 \text{ and } r = R \tag{7.2c}$$

Here, C_0 represents the initial concentration in the particle, and C_S is the steady-state concentration after PITT operation (concentration just outside the particle). The boundary condition (Eq. 2c) is discussed in detail in Ref [187]. The electrochemical Biot number, $B \equiv -R(i_0|_S)\partial U/\partial C|_S/(DR_gT)$, is a dimensionless parameter that represents the ratio of interfacial reaction rate to the diffusion rate. [90, 131, 187] Here i_0 is the exchange current density, U is the equilibrium potential, R_g is the gas constant, T is the temperature, and the subscript S reflects values associated with the end of the potential step experiment. The range of the electrochemical Biot number is $0 < B < \infty$. A large B value represents systems governed by diffusion, and small B represents systems where interfacial kinetics is slow. This boundary condition is mathematically equivalent to the surface evaporation [174] and radiation boundary condition in heat transfer problems. [173]

The solution for the diffusion equation (Eq. (7.1)) subject to the initial and boundary conditions (Eq. (7.2)) is [173, 174]

$$\frac{C - C_0}{C_S - C_0} = 1 - \frac{2B}{r/R}\sum_{n=1}^{\infty}\frac{\sin(\lambda_n r/R)}{(\lambda_n^2 + B^2 - B)\sin(\lambda_n)}\exp\left(-\lambda_n^2\frac{Dt}{R^2}\right) \tag{7.3}$$

where λ_n is the n^{th} positive root of $\tan(\lambda_n) = \lambda_n/(1 - B)$. The concentration function can also be obtained using Laplace and inverse Laplace transforms and can be expressed in terms of error functions, which converge fast at short times ($Dt/R^2 \ll 1$):

$$\frac{C-C_0}{C_S-C_0}=\frac{BR}{(B-1)r}\left\{\left(\operatorname{erfc}\frac{R-r}{2\sqrt{Dt}}-\operatorname{erfc}\frac{R+r}{2\sqrt{Dt}}\right)\right.$$

$$-\exp\left[(B-1)\left(1-\frac{r}{R}\right)+\frac{Dt}{R^2}(B-1)^2\right]\operatorname{erfc}\left[\frac{R-r}{2\sqrt{Dt}}+(B-1)\sqrt{\frac{Dt}{R^2}}\right]$$

$$+\exp\left[(B-1)\left(1+\frac{r}{R}\right)+\frac{Dt}{R^2}(B-1)^2\right]\operatorname{erfc}\left[\frac{R+r}{2\sqrt{Dt}}\right.$$

$$\left.\left.+(B-1)\sqrt{\frac{Dt}{R^2}}\right]\right\}c \qquad (7.4)$$

The dimensionless concentration profiles at short times ($Dt/R^2 \ll 1$) with various B values are calculated according to Eq. (7.4) and plotted in Fig. 7.1. When the system is diffusion controlled, such as B=50 in Fig. 7.1 (a), the concentration just inside the surface increases quickly to the final concentration C_S, showing the characteristics of a system governed by a constant surface concentration boundary condition. [117] When the system is controlled by both diffusion and interfacial kinetics, the concentration profile exhibits features between constant concentration and constant flux boundary conditions, as shown in Fig. 7.1 (b). When the system is controlled by interfacial kinetics, such as B=0.005 in Fig. 7.1 (c), the concentration just inside the electrode increases slowly with time (notice the small range of the concentration in Fig. 7.1 (c)).

The dimensionless concentration profiles at long times ($Dt/R^2 \gg 1$) with various B values are plotted in Fig. 7.2. We used the first 50 terms of the infinite series in Eq. (7.3) to calculate the concentration profiles. When interfacial reaction is facile comparing to diffusion, such as B=50 in Fig. 7.2 (a), the concentration just inside the particle is close to 1 at $Dt/R^2 = 1$. The overall concentration increases quickly, and reaches 0.9996 at $Dt/R^2 = 0.9$. For system controlled by both diffusion and interfacial kinetics, such as B=5 in Fig. 7.2 (b), the concentration profiles show characteristics between a constant flux and a constant concentration boundary condition. When the interfacial reaction is slow compare to diffusion, such as B=0.05 in Fig. 7.2 (c), the concentration in the

particle increases almost uniformly, showing the characteristics of constant surface flux boundary condition. Diffusion profiles for the slab geometry have similar trends and can be found in the literature. [90, 117, 163, 187]

7.3.1 Transient Current for PITT

The local current for each particle I_p is related to the concentration gradient at the particle surface by Fick's First Law

$$I_p = -zFAD\frac{\partial C}{\partial r}, \qquad r = R \tag{7.5}$$

where z is the charge number of the ions, F is Faraday's constant, and A is the surface area of the electrode. For the electrode considered in this analysis, the current distribution throughout the electrode is assumed uniform. Thus, the current for the electrode is related to the local current of each particle by

$$I = \eta\frac{V_{\text{elec}}}{V_{\text{ball}}}I_p \tag{7.6}$$

where V_{elec} is the volume of the electrode (including active materials and pores), V_{ball} is the average volume of a single particle, and η is the volume fraction of active materials (AM) in the electrode. Assuming the particles are perfect spheres with identical size, the total current under PITT operation can be obtained by substituting the expression of concentration (Eq. (7.2) or (7.3)) and Eq. (7.5) into Eq. (7.6) and using the relationship $(C_S - C_0) = Q/(zFV_{\text{elec}}\eta)$.

7.3.1.1 Current at Short times ($Dt/R^2 \ll 1$)

The current under PITT at short times is

$$I(t) = -\frac{3DQ}{R^2}\left\{-\frac{B}{(B-1)}\left(1-\operatorname{erfc}\frac{R}{\sqrt{Dt}}\right)\right.$$

$$+\frac{B^2}{(B-1)}\exp\left[\frac{Dt}{R^2}(B-1)^2\right]\operatorname{erfc}\left((B-1)\sqrt{\frac{Dt}{R^2}}\right)$$

$$+\frac{B^2-2B}{(B-1)}\exp\left[2(B-1)+\frac{Dt}{R^2}(B-1)^2\right]\operatorname{erfc}\left(\frac{R}{\sqrt{Dt}}\right.$$

$$\left.\left.+(B-1)\sqrt{\frac{Dt}{R^2}}\right)\right\} \tag{7.7}$$

Here Q is the total charge transferred during the potential step for the whole electrode.

When the interfacial resistance is negligible or interfacial reaction is infinitely fast, i.e., $B \to \infty$, the current becomes

$$\lim_{B\to\infty} I(t) = -\frac{3DQ}{R^2}\left(\frac{R}{\sqrt{\pi Dt}}-1\right) \tag{7.8}$$

For the special case $B = 1$, see Appendix B. The transient current for short times is plotted in Fig. 7.3 using Eqs. (7.7) and (7.8). When the interfacial kinetics are facile, the dimensionless current plot at short times is a straight line vs. $\sqrt{Dt/R^2}$ with a slope of $3/\sqrt{\pi}$. Note that the intercept of this line and the x-axis is not 0, and the slope is also different from the response current for slab electrodes. [149, 187] With increasing interfacial reaction resistance, the linearity of this curve decreases. Thus, diffusion coefficients are underestimated using the linear fitting method without considering the effect of interfacial kinetics. The position and shape of this curve are determined by two unknown parameters, D and B, and the diffusion coefficient D and dimensionless parameter B can be obtained by fitting the experimental PITT data using non-linear fitting methods.

7.3.1.2 Current at Long times ($Dt/R^2 \gg 1$)

Similar to Eq. (7.7), the current for PITT at long times is calculated according to Eqs. (7.3), (7.5), and (7.6) as

$$I(t) = 3\frac{2QD}{R^2}\frac{B^2}{(\lambda_1^2 + B^2 - B)}\exp\left(-\lambda_1^2\frac{Dt}{R^2}\right) \tag{7.9}$$

Rearranging Eq. (7.9), we obtain

$$\ln\big(I(t)\big) - \ln\left(\frac{2QD}{R^2}\right) = \ln\left[\frac{3B^2}{(\lambda_1^2 + B^2 - B)}exp\left(-\lambda_1^2\frac{Dt}{R^2}\right)\right] \tag{7.10}$$

For infinitely fast interfacial kinetics, i.e., $B \to \infty$, the current is

$$\lim_{B\to\infty} I(t) = \lim_{B\to\infty}\frac{2QD}{R^2}\frac{3B^2}{(\lambda_1^2 + B^2 - B)}\exp\left(-\lambda_1^2\frac{Dt}{R^2}\right) = \frac{6QD}{l^2}\exp\left(\pi^2\frac{Dt}{R^2}\right) \tag{7.11}$$

Appendix B treats the special case $B = 1$. The current at long times is plotted in Fig. 7.4 using Eqs. (7.10) and (7.11). It is seen that with slowing interfacial kinetics, the slope of the line decreases and the intercept with the y-axis is changing. As a result, the diffusion coefficient can be underestimated if interfacial kinetics resistance is not incorporated.

For long times ($Dt/R^2 \gg 1$), the diffusion coefficient D and dimensionless parameter B can be determined by solving the following equations simultaneously:

$$-\lambda_1^2\frac{D}{R^2} = \text{slope}$$

$$\frac{3B^2}{(\lambda_1^2 + B^2 - B)}\frac{2QD}{R^2} = \text{intercept on the } \ln I \text{ axis}$$

$$\tan(\lambda_1) = \frac{\lambda_1}{1 - B} \tag{7.12}$$

7.4 Experimental

7.4.1 Cell Fabrication

We applied the modified PITT to analyze lithium insertion into graphite (conventional MCMB), an important electrode material that is employed in high energy and high power applications. The electrode consists of 92 wt.% of MCMB and 8 wt.% of binder and conducting additives. The thickness of the electrode is 65 μm and the average diameter of MCMB particles is 18 μm. A piece of sample with diameter of 10 mm was used as the working electrode and was assembled into a 3-electrode cell (HS-3E, Hohsen). The counter electrode and reference electrode are pure lithium metal. The electrolyte used was a solution of 1 M $LiPF_6$ dissolved in 1:1 volume ratio of ethylene carbonate (EC) / dimethyl carbonate (DMC, Novolyte).

7.4.2 Electrochemical Characterization

A potentiostat (VMP3, Bio-Logic) was used to conduct the electrochemical measurements. The equilibrium voltage-capacity profile was obtained by the potentiostatic Coulombic titration technique. The voltage of the cell was stepped between 1.0 V and 0.005 V using 5 mV steps. At each step the potential was held until the current reached 0.09 μA g^{-1}, corresponding to a C/4000 rate. PITT experiments were carried out during charging of the half cell (delithiation of graphite) from 0.100 V to 0.105 V with a cutoff current of 0.09 μA g^{-1} (C/4000).

7.5 Results and Discussion

The quasi-equilibrium voltage-capacity profile of Li-graphite obtained by potentiostatic Coulombic titration is shown in Fig. 7.5, where we observe the typical electrochemical behavior of graphitic carbon, including the clearly defined single phase and two phase regions. [7] The PITT experiment was carried out in the LiC_{12} single phase region. The transient current under PITT operation is plotted in Fig. 7.6 and Fig. 7.7. For short times, D and B values were obtained by a least-square nonlinear fitting method (Curve Fitting

Toolbox in Matlab) according to Eq. (7.7). For long times, D and B values were obtained by solving Eq. (7.12) with parameters obtained experimentally in Fig. 7.7. The Li diffusion coefficients in LiC_{12} and the interfacial kinetics parameter B are summarized in Table 1. The diffusion coefficients of Li in LiC_{12} are in the range of the values reported previously. [160, 171, 189, 190] We note that it has been shown that when the chemical potential of Li is used as the driving force for diffusion, a substantially constant diffusion results Li fractions ranging from 0 to 1 in (LiC_6). [191]

From the definition of B in Eq. (7.2c), the exchange current density can be calculated. Here we obtained $(\partial U/\partial C)|_S$ from the quasi-equilibrium potential profile. The exchange current density of LiC_{12} is calculated to be 0.75 to 0.78 mA cm^{-2}, several times larger than the exchange current densities of graphitic carbon fibers [181] and amorphous Si electrodes reported previously. [187] The modified PITT thus allows simultaneous determination of diffusion coefficient and the exchange current density for Li in LiC_{12}.

Although the Li diffusion coefficient in graphite MCMB determined by the modified and the original PITT is similar because of the fast interfacial kinetics, it should be noted that it is improper to use the original PITT theory (cf. Eqs. 15 and 16 in Ref. [149]) to calculate the diffusion coefficient in powder electrodes, in which Dt/l^2 (l is the thickness of the electrode) is taken as the time constant for diffusion instead of Dt/R^2 (R is the radius of a single particle). The error may become large if the electrode thickness is much larger than the particle size. Eqs (7.8) and (7.11) can be used to calculate the diffusion coefficient in electrodes consisting of spherical particles if the interfacial kinetics is negligible.

The diffusion coefficient can also be affected by interfacial reaction kinetics. The electrochemical Biot number for MCMB electrodes obtained in this work ranges from 53.4 to 62.8, representing relatively fast interfacial kinetics, and is consistent with a previous prediction. [90] The error in PITT determined diffusion coefficients without considering the interfacial kinetics will become significant if the interfacial kinetics is slow compared to diffusion, such as for particles with smaller diameters. [90]

7.6 Conclusions

We examined PITT for spherical particles with finite interfacial reaction kinetics. Using the analytical solutions for the electric current, we show that one can obtain the diffusion coefficient and interfacial kinetics simultaneously. As an example application of this work, we investigate lithium diffusion in graphite (mesocarbon microbeads, MCMB), and we show that the diffusion coefficient, interfacial kinetics, and exchange current density can be determined simultaneously according to Eqs (7.7) and (7.12) for short times ($Dt/R^2 \ll 1$) and long times ($Dt/R^2 \gg 1$), respectively. If the interfacial reactions are facile, the diffusion coefficients can be determined by Eq. (7.8) and (7.11). This modified PITT is expected to be generally applicable for obtaining interfacial charge transfer reaction rates and diffusion coefficients for electrodes comprising substantially spherical particles.

7.7 Appendix

7.7.1 List of Symbols

A	surface area of an electrode
B	electrochemical Biot number
C	molar concentration
C_0	initial concentration
C_S	equilibrated concentration after PITT
D	diffusion coefficient of the solute

F	Faraday's constant
I	current for the electrode
I_{p}	local current at the surface of each particle
i_0	exchange current density
Q	total charge transferred for the electrode during a potential step
Q_{p}	total charge transferred for a single particle during a potential step
r	radial position
R	radii of particles
R_g	gas constant
t	time
T	temperature
U	equilibrium potential
V_{elec}	volume of the electrode

V_{p}	volume of a particle
z	charge number of the electro-active species
β	symmetry factor
η	volume fraction of active materials in the electrode
λ_n	n^{th} positive roots of $\tan(\lambda_n) = \lambda_n/(1-B)$
τ	dimensionless time

7.7.2 Analytic Solutions of Concentration and Current when B=1

At short times ($Dt/R^2 \ll 1$), the analytic solution for concentration with B=1 is

$$\frac{C-C_0}{C_R-C_0} = \frac{R}{r}\left\{\left(1+\frac{r}{R}\right)\mathrm{erfc}\left(\frac{R+r}{2\sqrt{Dt}}\right) - \left(1-\frac{r}{R}\right)\mathrm{erfc}\left(\frac{R-r}{2\sqrt{Dt}}\right) - \sqrt{\frac{Dt}{R^2}}\exp\left[-\left(\frac{R-r}{2\sqrt{Dt}}\right)^2\right] + \sqrt{\frac{Dt}{R^2}}\exp\left[-\left(\frac{R+r}{2\sqrt{Dt}}\right)^2\right]\right\} \tag{7.13}$$

The current for short times becomes

$$I = -\frac{3DQ}{R^2}\left\{1 - \mathrm{erfc}\frac{R}{\sqrt{Dt}} + \sqrt{\frac{Dt}{R^2}} - \sqrt{\frac{Dt}{R^2}}\exp\left[-\left(\frac{R}{\sqrt{Dt}}\right)^2\right]\right\} \tag{7.14}$$

At long times ($Dt/R^2 \gg 1$), the solution for concentration with $B = 1$ is [90]

$$\frac{C-C_0}{C_R-C_0}=1+\frac{2}{x}\sum_{n=1}^{\infty}(-1)^n\frac{\sin[(\frac{2n-1}{2})\pi x]}{[(\frac{2n-1}{2})\pi]^2}\exp\left[-\left(\frac{2n-1}{2}\pi\right)^2\frac{Dt}{R^2}\right] \quad (7.15)$$

The current is

$$I=\frac{3DQ}{R^2}\left[\frac{2}{\frac{\pi^2}{4}}\exp\left(-\frac{\pi^2}{4}\frac{Dt}{l^2}\right)\right]=\frac{24DQ}{R^2\pi^2}\exp\left(-\frac{\pi^2}{4}\frac{Dt}{R^2}\right) \quad (7.16)$$

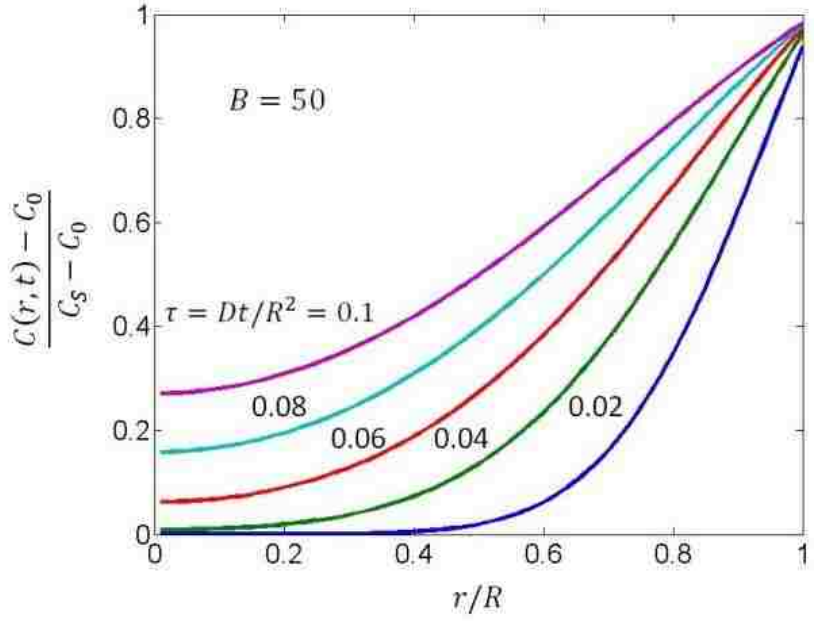
B = 50
τ = Dt/R² = 0.1
0.08
0.06
0.04
0.02
C(r,t) − C0 / Cs − C0
r/R

(a)

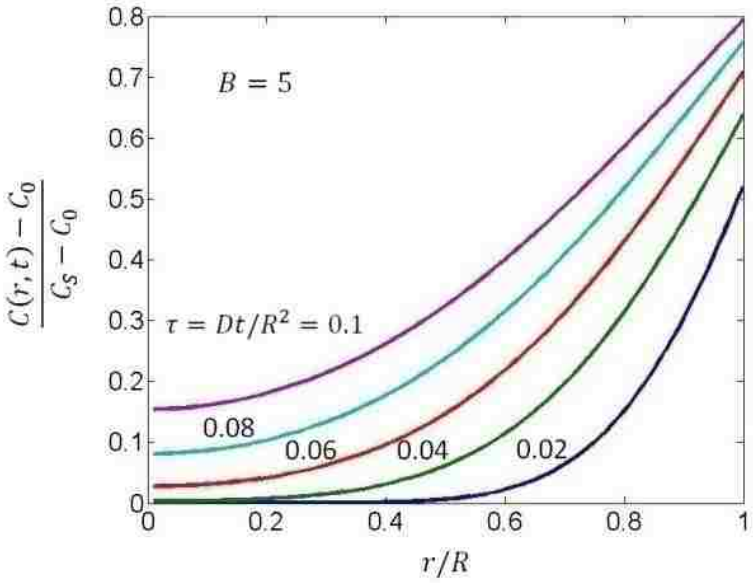
B = 5
τ = Dt/R² = 0.1
0.08
0.06
0.04
0.02
C(r,t) − C0 / Cs − C0
r/R

(b)

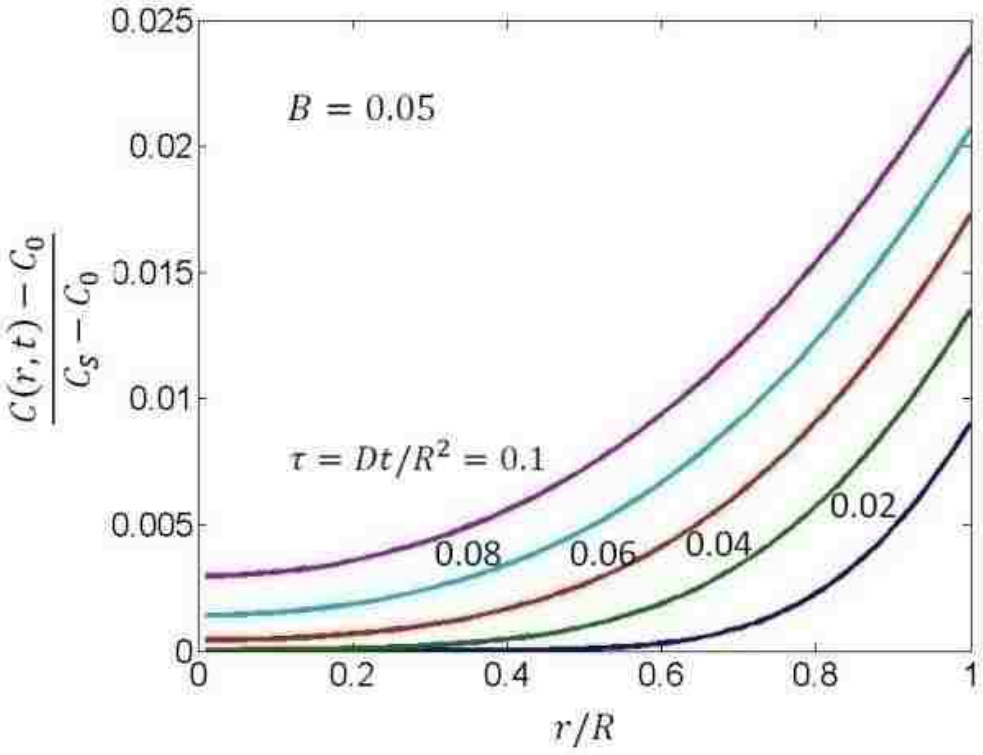

(c)

Fig. 7.1 Concentration profiles in an individual particle under PITT operation at short times ($Dt/R^2 \ll 1$) for different electrochemical Biot numbers. (a) B=50. (b) B=5. (c) B=0.05.

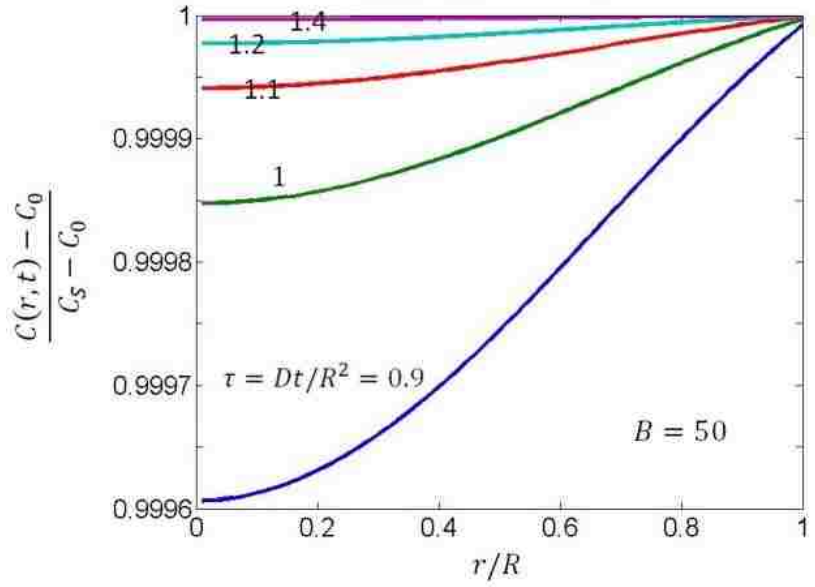
1
0.9999
0.9998
0.9997
0.9996
1.4
1.2
1.1
1
$\tau = Dt/R^2 = 0.9$
$B = 50$
0
0.2
0.4
0.6
0.8
1
r/R
$\frac{C(r,t) - C_0}{C_s - C_0}$

(a)

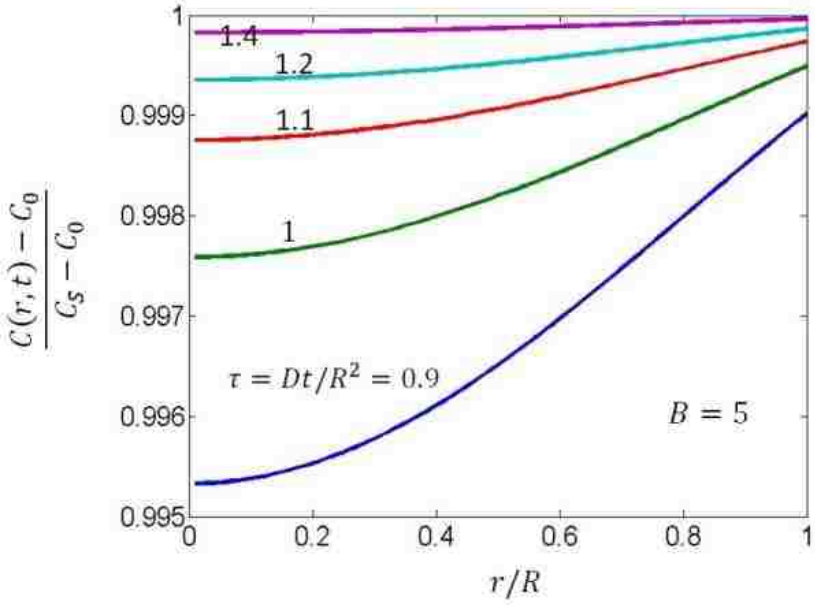
1
0.999
0.998
0.997
0.996
0.995
1.4
1.2
1.1
1
$\tau = Dt/R^2 = 0.9$
$B = 5$
0
0.2
0.4
0.6
0.8
1
r/R
$\frac{C(r,t) - C_0}{C_s - C_0}$

(b)

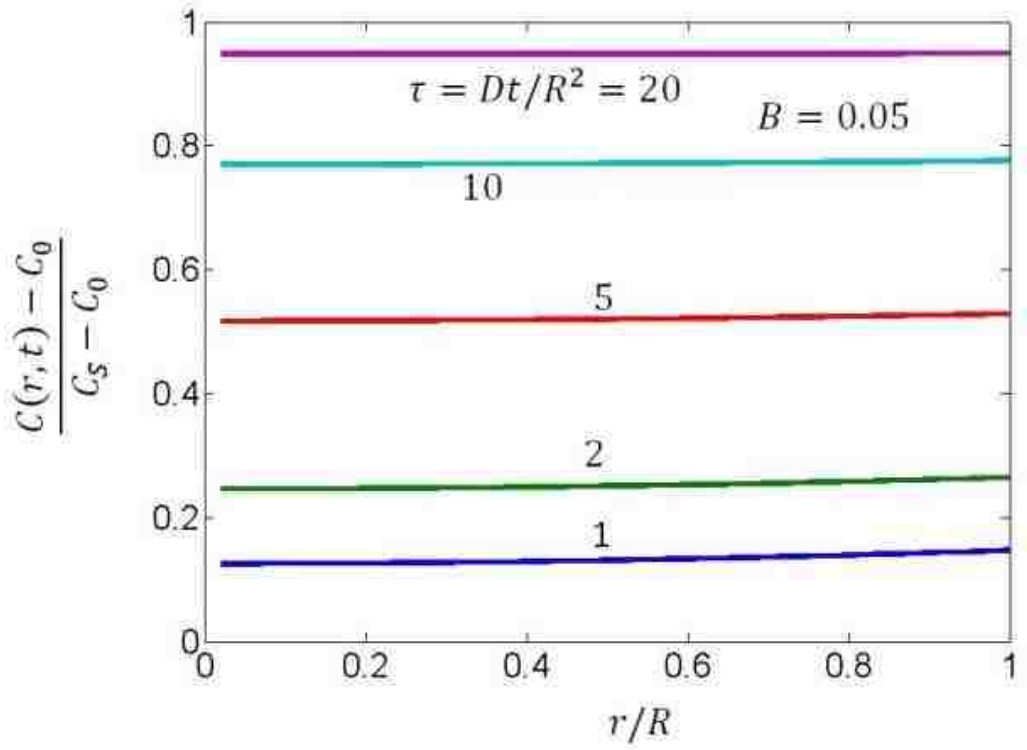

(c)

Fig. 7.2 Concentration profiles in an individual particle under PITT operation at long times ($Dt/R^2 \gg 1$) for different electrochemical Biot numbers. (a) B=50. (b) B=5. (c) B=0.05.

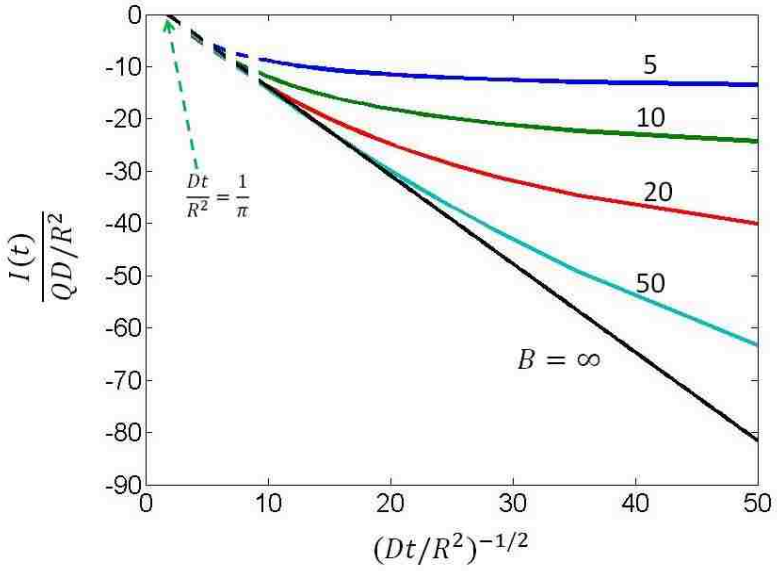

Fig. 7.3 Dimensionless transient current vs. time at short times ($Dt/R^2 \ll 1$) with various electrochemical Biot numbers.

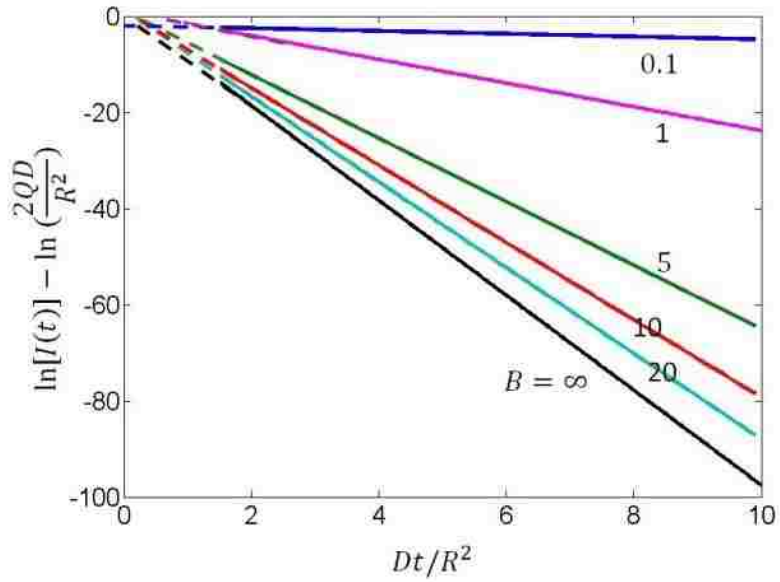

Fig. 7.4 Dimensionless transient current vs. time at long times ($Dt/R^2 \gg 1$) with various electrochemical Biot numbers.

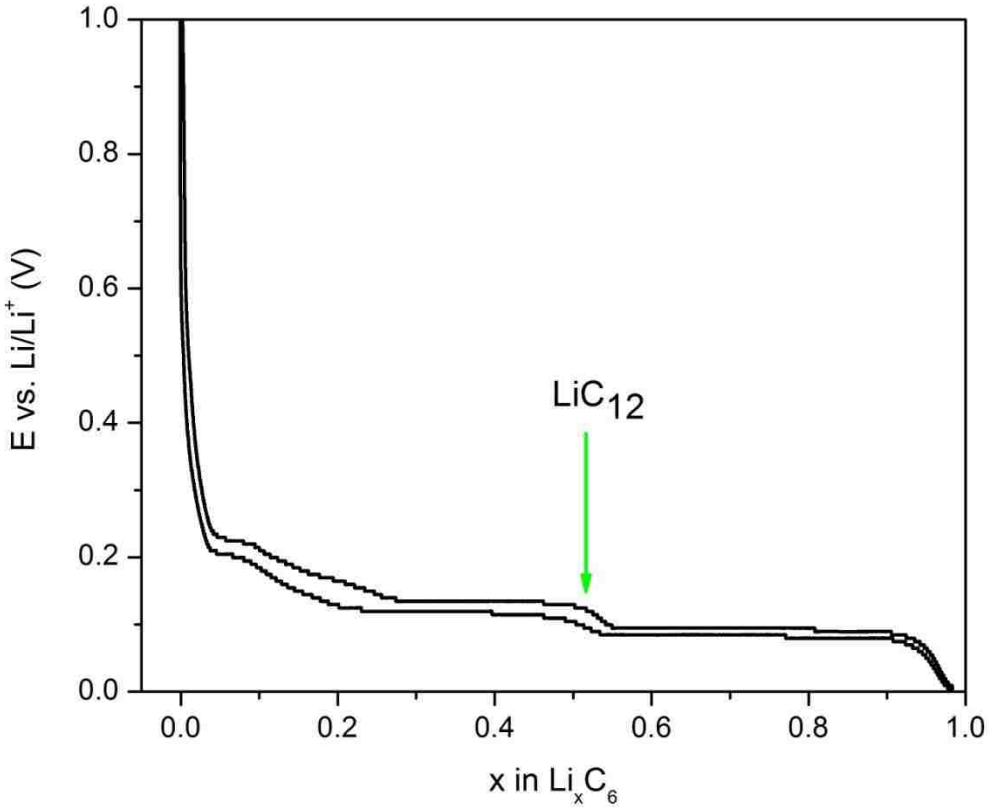

Fig. 7.5 Quasi-equilibrium potential-composition profile of Li-graphite (MCMB) obtained by potentiostatic Coulombic titration.

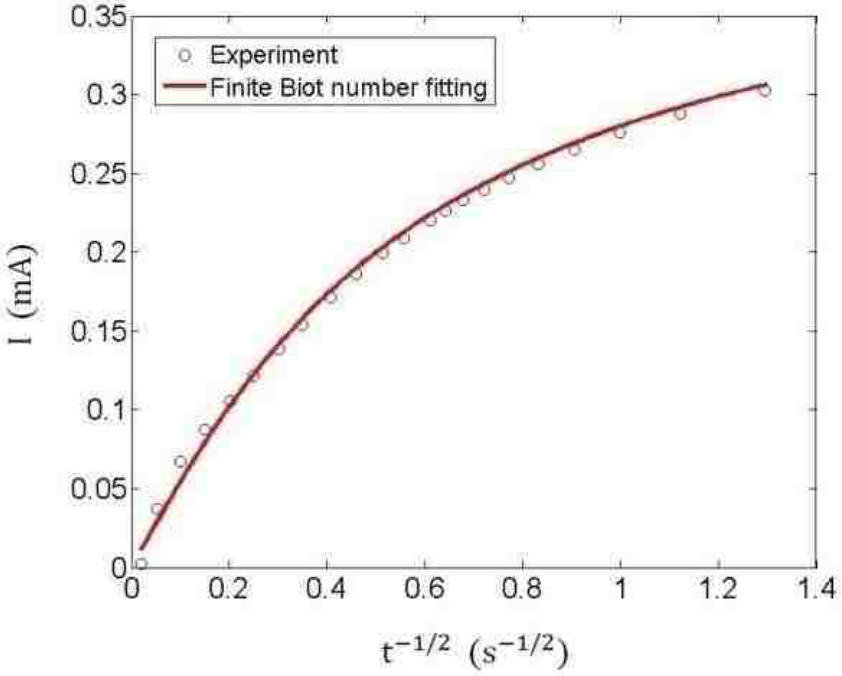

Fig. 7.6 Plot of transient current vs. $t^{-1/2}$ at short times.

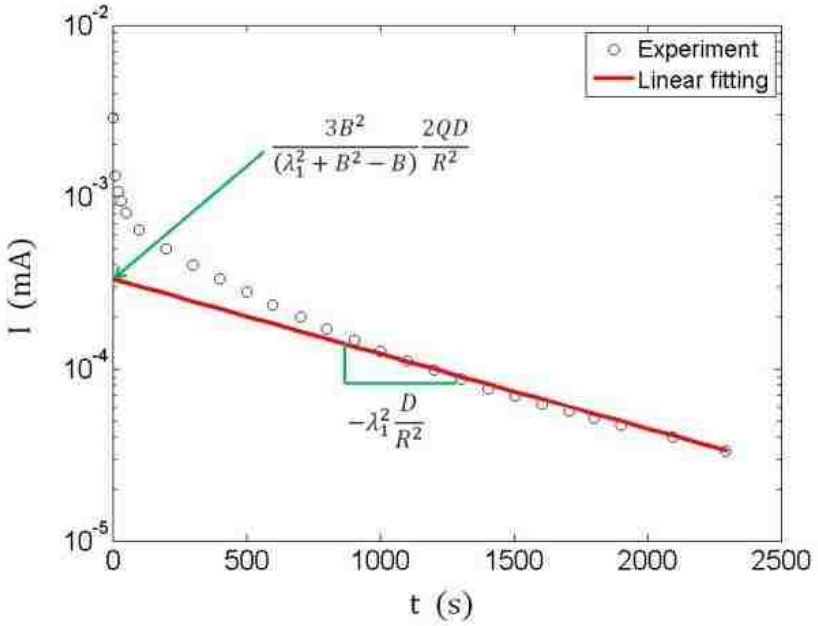

Fig. 7.7 Exponential dependence of current on time at long times.

Table 7.1 Diffusion coefficient and interfacial kinetics of Li in MCMB (LiC_{12}) obtained from modified PITT.

Method	D ($cm^2\ s^{-1}$)	B	i_0 ($mA\ cm^{-2}$)
Short times ($Dt/R^2 \ll 1$), Eq. (7.7)	1.6×10^{-10}	62.8	0.75
Long times ($Dt/R^2 \gg 1$), Eq. (7.12)	1.8×10^{-10}	53.4	0.78

Chapter 8 Conclusions and Future Work

8.1 Conclusions

Current commercial lithium-ion batteries (LIBs) do not meet the requirement of energy storage for several fast growing products, especially hybrid and pure electric vehicles. LIB electrodes with higher capacity, energy density, and cycle life are required. High capacity negative LIB electrodes usually undergo large volume expansion and contraction upon cycling. The associated large diffusion-induced stresses cause cracking of the electrode materials, which further leads to loss of conduction and capacity fading. In this dissertation, I focus on understanding the mechanical behavior of high-capacity LIB negative electrodes and searching for strategies to avoid mechanical degradation. Additionally, an electro-analytical technique (modified PITT) was proposed to measure interfacial reaction kinetics and diffusion coefficients, which are essential for understanding the effects of surface modification on LIB electrodes.

Tin (Sn) is a candidate material for negative electrodes of lithium-ion batteries (LIBs) because of its high theoretical energy capacity. In Chapter 3, we study the behavior of Sn thin-film electrodes, and show Sn-whisker growth on Sn thin-film electrodes after lithiation and de-lithiation. The compressive stress generated by electrochemical lithiation of the Sn-thin films, which is about 700 MPa, is likely the driving force for the growth of the Sn whiskers. Similar to the phenomena of Li dendrite formation, Sn whiskers may penetrate through the separator, and short-circuit the electrochemical cell. As a result, attention should be paid to the issue of whisker growth in Sn-based electrodes and other electrodes containing low melting point elements.

In Chapter 4, we study the fracture behavior and cracking patterns in amorphous silicon (Si) thin film electrodes with thickness ranging from 100 to 1000 nm as a result of electrochemical cycling. A modified spring-block model is shown to capture the essential features of cracking patterns of electrode materials, including self-similarity. Cracks generated in thick films are straight with a few sharp direction changes and the area

separated by cracks is large. For thin films cracks show more wiggles and the average area divided by cracks is small. After primary cracks form, crack patterns do not change further with electrochemical cycling, while the surface becomes rougher. As the thickness of film decreases, the average size of islands separated by cracks decreases. A critical thickness bellow which material would not crack is found for amorphous Si films. The experimental and simulation results suggest two directions of designing electrodes which do not crack: (1) patterning the electrodes in which the pattern size is smaller than the average cracked size for that specific film thickness, and (2) reducing the film thickness to less than the critical thickness of cracking, which is between 100 and 200 nm for amorphous Si on stainless steel substrate.

In Chapter 5, we propose a new strategy to achieve high capacity and long durability of LIB electrodes. We demonstrate the concept of using low-melting point metal/alloys as self-healing LIB electrodes. The liquid metal gallium (Ga) electrode undergoes crystallization upon lithiation and transforms to a solid electrode. During delithiation the solid phases are transformed to the liquid state. Cracks formed in the electrode mostly during delithiation can be self-healed by the solid-to-liquid transformation. This work indicates that cracking as a failure mode can be remedied using liquid metal electrodes. Since many low melting point alloys exist and can potentially store large quantities of Li, the liquid metal approach demonstrated by liquid Ga may be generalized to many systems of technological significance.

The Potentiostatic Intermittent Titration Technique (PITT) is one of the widely used methods for determining the diffusion coefficient in electrochemical materials, such as lithium diffusion in lithium-ion battery electrodes. The conventional PITT analysis neglects interfacial resistance and assumes the system is diffusion controlled. For actual electrode systems, however, surface reaction, as well as diffusion, may be rate limiting. In Chapters 6 and 7, we derive modified PITT as an electro-analytical technique to quantify the interfacial reaction kinetics as well as diffusion coefficients. For small amplitude potential steps, we obtain analytic solutions for the measured transient current associated with PITT, taking into account the effects of finite surface reaction rates. By

fitting experimental data with the analytic solutions, the diffusion coefficient, surface reaction rate, and the exchange current density can be determined simultaneously. An example of lithium diffusion in amorphous silicon thin-film electrodes is used to demonstrate the modified PITT approach for slab geometry (Chapter 6), and an example of lithium diffusion in graphite (mesocarbon microbeads, MCMB) is used to demonstrate the modified PITT for spherical geometry (Chapter 7). The modified PITT is applicable to LIB electrodes, as well as other electrochemical systems wherein the measurement of diffusion and kinetic parameters (e.g., the exchange current density) are of interest.

8.2 Future Work

During the period of the author's Ph.D. study, making better lithium-ion batteries becomes a hot topic and draws attentions from researchers with a variety of backgrounds. Each week there are about 50 to 200 new journal publications on the topic of lithium-ion batteries. Though highly intensively researched, there is still no perfect method to overcome some of the issues related to mechanical degradation of LIB electrodes. Thus, there is plenty of room to improve lithium ion batteries in aspects of capacity, power, cycling performance, power performance, safety, and cost.

In particular, future researchers are encouraged to (1) study cracking patterns or networks in powder-shaped electrode materials, and extend the spring-block simulation model to 3-D to predict cracking behavior in particles. (2) It is also interesting to investigate the cracking behavior of low melting point electrode materials (such as Sn and Ga), and analyze the differences from high melting point electrode materials (such as Si). (3) The electroanalytical technique, modified PITT, can be used to quantify the effect of surface modifications and coatings, and thus to help design ideal surface modification strategies and to optimize the performance of LIB electrodes.

References

1. J.M. Tarascon and M. Armand, Issues and Challenges Facing Rechargeable Lithium Batteries. *Nature*, 414(6861): 359-367. (2001)

2. M. Armand and J.M. Tarascon, Building Better Batteries. *Nature*, 451(7179): 652-657. (2008)

3. R.A. Huggins, *Advanced Batteries: Materials Science Aspects*. 2009: Springer.

4. Y. Itou and Y. Ukyo, Performance of $LiNiCoO_2$ Materials for Advanced Lithium-Ion Batteries. *Journal of Power Sources*, 146(1-2): 39-44. (2005)

5. H. Li, Z.X. Wang, L.Q. Chen, and X.J. Huang, Research on Advanced Materials for Li-ion Batteries. *Advanced Materials*, 21(45): 4593-4607. (2009)

6. J.B. Goodenough and Y. Kim, Challenges for Rechargeable Li Batteries. *Chemistry of Materials*, 22(3): 587-603. (2010)

7. T. Ohzuku, Y. Iwakoshi, and K. Sawai, Formation if Lithium-Graphite Intercalation Compounds in Nonaqueous Electrolytes and their Application as a Negative Electrode for a Lithium Ion (Shuttlecock) Cell. *Journal of the Electrochemical Society*, 140(9): 2490-2498. (1993)

8. J.R. Dahn, T. Zheng, Y.H. Liu, and J.S. Xue, Mechamisms for Lithium Insertion in Carbonaceous Materials. *Science*, 270(5236): 590-593. (1995)

9. M. Winter, J.O. Besenhard, M.E. Spahr, and P. Novak, Insertion Electrode Materials for Rechargeable Lithium Batteries. *Advanced Materials*, 10(10): 725-763. (1998)

10. R.A. Huggins, Lithium Alloy Negative Electrodes. *Journal of Power Sources*, 81: 13-19. (1999)

11. U. Kasavajjula, C.S. Wang, and A.J. Appleby, Nano- and Bulk-Silicon-Based Insertion Anodes for Lithium-Ion Secondary Cells. *Journal of Power Sources*, 163(2): 1003-1039. (2007)

12. J.O. Besenhard, J. Yang, and M. Winter, Will Advanced Lithium-Alloy Anodes Have A Chance in Lithium-Ion Batteries? *Journal of Power Sources*, 68(1): 87-90. (1997)

13. I.A. Courtney, J.S. Tse, O. Mao, J. Hafner, and J.R. Dahn, *Ab initio* Calculation of the Lithium-Tin Voltage Profile. *Physical Review B*, 58(23): 15583-15588. (1998)

14. B. Laforge, L. Levan-Jodin, R. Salot, and A. Billard, Study of Germanium as Electrode in Thin-Film Battery. *Journal of the Electrochemical Society*, 155(2): A181-A188. (2008)

15. L. Baggetto and P.H.L. Notten, Lithium-Ion (De)Insertion Reaction of Germanium Thin-Film Electrodes: An Electrochemical and In Situ XRD Study. *Journal of the Electrochemical Society*, 156(3): A169-A175. (2009)

16. Z.G. Yang, D. Choi, S. Kerisit, K.M. Rosso, D.H. Wang, J. Zhang, G. Graff, and J. Liu, Nanostructures and Lithium Electrochemical Reactivity of Lithium Titanites and Titanium Oxides: A Review. *Journal of Power Sources*, 192(2): 588-598. (2009)

17. T. Nagaura and K. Tozawa, *Progress in Batteries and Solar Cells*. Vol. 9. 1990.

18. M. Winter and J.O. Besenhard, Electrochemical Lithiation of Tin and Tin-Based Intermetallics and Composites. *Electrochimica Acta*, 45(1-2): 31-50. (1999)

19. K. Sato, M. Noguchi, A. Demachi, N. Oki, and M. Endo, A Mechamism of Lithium Storage in Disordered Carbons. *Science*, 264(5158): 556-558. (1994)

20. A. Mukhopadhyay, A. Tokranov, K. Sena, X.C. Xiao, and B.W. Sheldon, Thin Film Graphite Electrodes with Low Stress Generation during Li-Intercalation. *Carbon*, 49(8): 2742-2749. (2011)

21. V.A. Sethuraman, M.J. Chon, M. Shimshak, V. Srinivasan, and P.R. Guduru, *In situ* Measurements of Stress Evolution in Silicon Thin Films during Electrochemical Lithiation and Delithiation. *Journal of Power Sources*, 195(15): 5062-5066. (2010)

22. S.K. Soni, B.W. Sheldon, X.C. Xiao, and A. Tokranov, Thickness Effects on the Lithiation of Amorphous Silicon Thin Films. *Scripta Materialia*, 64(4): 307-310. (2011)

23. M.N. Obrovac and L. Christensen, Structural Changes in Silicon Anodes during Lithium Insertion/Extraction. *Electrochemical and Solid State Letters*, 7(5): A93-A96. (2004)

24. D. Larcher, S. Beattie, M. Morcrette, K. Edstroem, J.C. Jumas, and J.M. Tarascon, Recent Findings and Prospects in the Field of Pure Metals as Negative Electrodes for Li-Ion Batteries. *Journal of Materials Chemistry*, 17(36): 3759-3772. (2007)

25. N. Takami, H. Inagaki, T. Kishi, Y. Harada, Y. Fujita, and K. Hoshina, Electrochemical Kinetics and Safety of 2-Volt Class Li-Ion Battery System Using Lithium Titanium Oxide Anode. *Journal of the Electrochemical Society*, 156(2): A128-A132. (2009)

26. N. Takami, K. Hoshina, and H. Inagaki, Lithium Diffusion in $Li_{4/3}Ti_{5/3}O_4$ Particles during Insertion and Extraction. *Journal of the Electrochemical Society*, 158(6): A725-A730. (2011)

27. T.D. Hatchard and J.R. Dahn, *In situ* XRD and Electrochemical Study of the Reaction of Lithium with Amorphous Silicon. *Journal of the Electrochemical Society*, 151(6): A838-A842. (2004)

28. G.R. Goward, N.J. Taylor, D.C.S. Souza, and L.F. Nazar, The True Crystal Structure of $Li_{17}M_4$ (M=Ge, Sn, Pb)-Revised from $Li_{22}M_5$. *Journal of Alloys and Compounds*, 329(1-2): 82-91. (2001)

29. C.M. Park, J.H. Kim, H. Kim, and H.J. Sohn, Li-Alloy Based Anode Materials for Li Secondary Batteries. *Chemical Society Reviews*, 39(8): 3115-3141. (2010)

30. H. Kim, M. Seo, M.H. Park, and J. Cho, A Critical Size of Silicon Nano-Anodes for Lithium Rechargeable Batteries. *Angewandte Chemie-International Edition*, 49(12): 2146-2149. (2010)

31. L.Y. Beaulieu, K.W. Eberman, R.L. Turner, L.J. Krause, and J.R. Dahn, Colossal Reversible Volume Changes in Lithium Alloys. *Electrochemical and Solid State Letters*, 4(9): A137-A140. (2001)

32. M.N. Obrovac and L.J. Krause, Reversible Cycling of Crystalline Silicon Powder. *Journal of the Electrochemical Society*, 154(2): A103-A108. (2007)

33. M. Wachtler, M. Winter, and J.O. Besenhard, Anodic Materials for Rechargeable Li-Batteries. *Journal of Power Sources*, 105: 151-160. (2002)

34. J.P. Maranchi, A.F. Hepp, and P.N. Kumta, High Capacity, Reversible Silicon Thin-Film Anodes for Lithium-Ion Batteries. *Electrochemical and Solid State Letters*, 6(9): A198-A201. (2003)

35. J. Graetz, C.C. Ahn, R. Yazami, and B. Fultz, Highly Reversible Lithium Storage in Nanostructured Silicon. *Electrochemical and Solid State Letters*, 6(9): A194-A197. (2003)

36. C.K. Chan, H.L. Peng, G. Liu, K. McIlwrath, X.F. Zhang, R.A. Huggins, and Y. Cui, High-Performance Lithium Battery Anodes using Silicon Nanowires. *Nature Nanotechnology*, 3(1): 31-35. (2008)

37. S.M. Paek, E. Yoo, and I. Honma, Enhanced Cyclic Performance and Lithium Storage Capacity of SnO_2/Graphene Nanoporous Electrodes with Three-Dimensionally Delaminated Flexible Structure. *Nano Letters*, 9(1): 72-75. (2009)

38. S. Nakade, S. Kambe, T. Kitamura, Y. Wada, and S. Yanagida, Effects of lithium ion density on electron transport in nanoporous TiO_2 electrodes. *Journal of Physical Chemistry B*, 105(38): 9150-9152. (2001)

39. X. Xiao, P. Liu, M.W. Verbrugge, H. Haftbaradarab, and H. Gao, Improved Cycling Stability of Solicon Thin Film Electrodes through Patterning for High Energy Density Lithium Batteries. *Journal of Power Sources*, 196(3): 1409-1416. (2010)

40. R.B. Lewis, A. Timmons, R.E. Mar, and J.R. Dahn, *In Situ* AFM Measurements of the Expansion and Contraction of Amorphous Sn-Co-C Films Reacting with Lithium. *Journal of the Electrochemical Society*, 154(3): A213-A216. (2007)

41. L. Bazin, S. Mitra, P.L. Taberna, P. Poizot, M. Gressier, M.J. Menu, A. Barnabe, P. Simon, and J.M. Tarascon, High rate capability pure Sn-based nano-architectured electrode assembly for rechargeable lithium batteries. *Journal of Power Sources*, 188(2): 578-582. (2009)

42. X.L. Wang, W.Q. Han, H.Y. Chen, J.M. Bai, T.A. Tyson, X.Q. Yu, X.J. Wang, and X.Q. Yang, Amorphous Hierarchical Porous GeO_x as High-Capacity Anodes for Li Ion Batteries with Very Long Cycling Life. *Journal of the American Chemical Society*, 133(51): 20692-20695. (2011)

43. S.K. Soni, B.W. Sheldon, X.C. Xiao, M.W. Verbrugge, D. Ahn, H. Haftbaradaran, and H.J. Gao, Stress Mitigation during the Lithiation of Patterned Amorphous Si Islands. *Journal of the Electrochemical Society*, 159(1): A38-A43. (2012)

44. Y.T. Cheng and M.W. Verbrugge, The influence of surface mechanics on diffusion induced stresses within spherical nanoparticles. *Journal of Applied Physics*, 104(8). (2008)

45. R. Deshpande, Y.T. Cheng, and M.W. Verbrugge, Modeling diffusion-induced stress in nanowire electrode structures. *Journal of Power Sources*, 195(15): 5081-5088. (2010)

46. D. Aurbach, Review of selected electrode-solution interactions which determine the performance of Li and Li ion batteries. *Journal of Power Sources*, 89(2): 206-218. (2000)

47. M. Winter, The Solid Electrolyte Interphase - The Most Important and the Least Understood Solid Electrolyte in Rechargeable Li Batteries. *Zeitschrift Fur Physikalische Chemie-International Journal of Research in Physical Chemistry & Chemical Physics*, 223(10-11): 1395-1406. (2009)

48. P. Verma, P. Maire, and P. Novak, A review of the features and analyses of the solid electrolyte interphase in Li-ion batteries. *Electrochimica Acta*, 55(22): 6332-6341. (2010)

49. T.D. Hatchard and J.R. Dahn, Electrochemical reaction of the SiAg binary system with li. *Journal of the Electrochemical Society*, 152(7): A1445-A1451. (2005)

50. S.W. Song, K.A. Striebel, R.P. Reade, G.A. Roberts, and E.J. Cairns, Electrochemical studies of nanoncrystalline Mg_2Si thin film electrodes prepared by pulsed laser deposition. *Journal of the Electrochemical Society*, 150(1): A121-A127. (2003)

51. S.W. Song, K.A. Striebel, X.Y. Song, and E.J. Cairns, Amorphous and nanocrystalline Mg_2Si thin-film electrodes. *Journal of Power Sources*, 119: 110-112. (2003)

52. J. Wolfenstine, $CaSi_2$ as an anode for lithium-ion batteries. *Journal of Power Sources*, 124(1): 241-245. (2003)

53. C.S. Wang, G.T. Wu, X.B. Zhang, Z.F. Qi, and W.Z. Li, Lithium insertion in carbon-silicon composite materials produced by mechanical milling. *Journal of the Electrochemical Society*, 145(8): 2751-2758. (1998)

54. G.X. Wang, J.H. Ahn, J. Yao, S. Bewlay, and H.K. Liu, Nanostructured Si-C composite anodes for lithium-ion batteries. *Electrochemistry Communications*, 6(7): 689-692. (2004)

55. G.X. Wang, J. Yao, and H.K. Liu, Characterization of nanocrystalline Si-MCMB composite anode materials. *Electrochemical and Solid State Letters*, 7(8): A250-A253. (2004)

56. T.D. Hatchard, M.N. Obrovac, and J.R. Dahn, Electrochemical reaction of the $Si_{1-x}Zn_x$ binary system with Li. *Journal of the Electrochemical Society*, 152(12): A2335-A2344. (2005)

57. Y.L. Kim, H.Y. Lee, S.W. Jang, S.H. Lim, S.J. Lee, H.K. Baik, Y.S. Yoon, and S.M. Lee, Electrochemical characteristics of Co-Si alloy and multilayer films as anodes for lithium ion microbatteries. *Electrochimica Acta*, 48(18): 2593-2597. (2003)

58. M.D. Fleischauer, M.N. Obrovac, and J.R. Dahn, Simple model for the capacity of amorphous silicon-aluminum-transition metal negative electrode materials. *Journal of the Electrochemical Society*, 153(6): A1201-A1205. (2006)

59. M.D. Fleischauer, M.N. Obrovac, J.D. McGraw, R.A. Dunlap, J.M. Topple, and J.R. Dahn, Al-M (M = Cr, Fe, Mn, Ni) thin-film negative electrode materials. *Journal of the Electrochemical Society*, 153(3): A484-A491. (2006)

60. J.B. Kim, H.Y. Lee, K.S. Lee, S.H. Lim, and S.M. Lee, Fe/Si multi-layer thin film anodes for lithium rechargeable thin film batteries. *Electrochemistry Communications*, 5(7): 544-548. (2003)

61. J.B. Kim, S.H. Lim, and S.M. Lee, Structural change in si phase of Fe/Si multilayer thin-film anodes during Li insertion/extraction reaction. *Journal of the Electrochemical Society*, 153(3): A455-A458. (2006)

62. M. Miyachi, H. Yamamoto, H. Kawai, T. Ohta, and M. Shirakata, Analysis of SiO anodes for lithium-ion batteries. *Journal of the Electrochemical Society*, 152(10): A2089-A2091. (2005)

63. M. Miyachi, H. Yamamoto, and H. Kawai, Electrochemical properties and chemical structures of metal-doped SiO anodes for Li-ion rechargeable batteries. *Journal of the Electrochemical Society*, 154(4): A376-A380. (2007)

64. Y. Idota, T. Kubota, A. Matsufuji, Y. Maekawa, and T. Miyasaka, Tin-based amorphous oxide: A high-capacity lithium-ion-storage material. *Science*, 276(5317): 1395-1397. (1997)

65. I.A. Courtney and J.R. Dahn, Electrochemical and In Situ X-Ray Diffraction Studies of the Reaction of Lithium with Tin Oxide Composites. *Journal of the Electrochemical Society*, 144(6): 2045-2052. (1997)

66. W.F. Liu, X.J. Huang, Z.X. Wang, H. Li, and L.Q. Chen, Studies of stannic oxide as an anode material for lithium-ion batteries. *Journal of the Electrochemical Society*, 145(1): 59-62. (1998)

67. T. Morita and N. Takami, Nano Si cluster-SiO_x-C composite material as high-capacity anode material for rechargeable lithium batteries. *Journal of the Electrochemical Society*, 153(2): A425-A430. (2006)

68. J.H. Kim, H.J. Sohn, H. Kim, G. Jeong, and W. Choi, Enhanced cycle performance of SiO-C composite anode for lithium-ion batteries. *Journal of Power Sources*, 170(2): 456-459. (2007)

69. C.H. Doh, C.W. Park, H.M. Shin, D.H. Kim, Y.D. Chung, S.I. Moon, B.S. Jin, H.S. Kim, and A. Veluchamy, A new SiO/C anode composition for lithium-ion battery. *Journal of Power Sources*, 179(1): 367-370. (2008)

70. J. Li, R.B. Lewis, and J.R. Dahn, Sodium carboxymethyl cellulose - A potential binder for Si negative electrodes for Li-ion batteries. *Electrochemical and Solid State Letters*, 10(2): A17-A20. (2007)

71. M. Mancini, F. Nobili, R. Tossici, M. Wohlfahrt-Mehrens, and R. Marassi, High performance, environmentally friendly and low cost anodes for lithium-ion battery based on TiO(2) anatase and water soluble binder carboxymethyl cellulose. *Journal of Power Sources*, 196(22): 9665-9671. (2011)

72. D. Munao, J.W.M. van Erven, M. Valvo, E. Garcia-Tamayo, and E.M. Kelder, Role of the binder on the failure mechanism of Si nano-composite electrodes for Li-ion batteries. *Journal of Power Sources*, 196(16): 6695-6702. (2011)

73. S.K. Martha, J. Nanda, G.M. Veith, and N.J. Dudney, Electrochemical and rate performance study of high-voltage lithium-rich composition: $Li_{1.2}Mn_{0.525}Ni_{0.175}Co_{0.1}O_2$. *Journal of Power Sources*, 199: 220-226. (2012)

74. L. Zou, R.T. Lv, F.Y. Kang, L. Gan, and W.C. Shen, Preparation and application of bamboo-like carbon nanotubes in lithium ion batteries. *Journal of Power Sources*, 184(2): 566-569. (2008)

75. I. Belharouak, C. Johnson, and K. Amine, Synthesis and electrochemical analysis of vapor-deposited carbon-coated $LiFePO_4$. *Electrochemistry Communications*, 7(10): 983-988. (2005)

76. Z.H. Chen and J.R. Dahn, Reducing carbon in $LiFePO_4$/C composite electrodes to maximize specific energy, volumetric energy, and tap density. *Journal of the Electrochemical Society*, 149(9): A1184-A1189. (2002)

77. Q. Cao, H.P. Zhang, G.J. Wang, Q. Xia, Y.P. Wu, and H.Q. Wu, A novel carbon-coated $LiCoO_2$ as cathode material for lithium ion battery. *Electrochemistry Communications*, 9(5): 1228-1232. (2007)

78. J. Gao, H.P. Zhang, L.J. Fu, T. Zhang, Y.P. Wu, T. Takamura, H.Q. Wu, and R. Holze, Suppressing propylene carbonate decomposition by coating graphite electrode foil with silver. *Electrochimica Acta*, 52(17): 5417-5421. (2007)

79. F. Nobili, M. Mancini, P.E. Stallworth, F. Croce, S.G. Greenbaum, and R. Marassi, Tin-coated graphite electrodes as composite anodes for Li-ion batteries. Effects of tin coatings thickness toward intercalation behavior. *Journal of Power Sources*, 198: 243-250. (2012)

80. M. Shafiei and A.T. Alpas, Electrochemical performance of a tin-coated carbon fibre electrode for rechargeable lithium-ion batteries. *Journal of Power Sources*, 196(18): 7771-7778. (2011)

81. Z.H. Chen and J.R. Dahn, Studies of $LiCoO_2$ coated with metal oxides. *Electrochemical and Solid State Letters*, 6(11): A221-A224. (2003)

82. Y.K. Sun, Y.S. Lee, M. Yoshio, and K. Amine, Synthesis and electrochemical properties of ZnO-coated $LiNi_{0.5}Mn_{1.5}O_4$ spinel as 5 V cathode material for lithium secondary batteries. *Electrochemical and Solid State Letters*, 5(5): A99-A102. (2002)

83. X.C. Xiao, P. Lu, and D. Ahn, Ultrathin Multifunctional Oxide Coatings for Lithium Ion Batteries. *Advanced Materials*, 23(34): 3911-+. (2011)

84. Y. Kim, G.M. Veith, J. Nanda, R.R. Unocic, M.F. Chi, and N.J. Dudney, High voltage stability of $LiCoO_2$ particles with a nano-scale Lipon coating. *Electrochimica Acta*, 56(19): 6573-6580. (2011)

85. Y. Wu, A.V. Murugan, and A. Manthiram, Surface modification of high capacity layered $Li(Li_{0.2}Mn_{0.54}Ni_{0.13}Co_{0.13})O_2$ cathodes by $AlPO_4$. *Journal of the Electrochemical Society*, 155(9): A635-A641. (2008)

86. Y.K. Sun, S.W. Cho, S.W. Lee, C.S. Yoon, and K. Amine, AlF_3-coating to improve high voltage cycling performance of Li $Ni_{1/3}Co_{1/3}Mn_{1/3}$ O cathode materials for lithium secondary batteries. *Journal of the Electrochemical Society*, 154(3): A168-A172. (2007)

87. J. Hassoun, S. Panero, P. Simon, P.L. Taberna, and B. Scrosati, High-Rate, Long-Life Ni-Sn Nanostructured Electrodes for Lithium-Ion Batteries. *Advanced Materials*, 19(12): 1632-1635. (2007)

88. J. Hassoun, G. Derrien, S. Panero, and B. Scrosati, A nanostructured Sn-C composite lithium battery electrode with unique stability and high electrochemical performance. *Advanced Materials*, 20(16): 3169-3175. (2008)

89. H. Wu, G. Chan, J.W. Choi, I. Ryu, Y. Yao, M.T. McDowell, S.W. Lee, A. Jackson, L. Hu, and Y. Cui, Six Thousand Electrochemical Cycles of Double-Walled Silicon Nanotube Anodes for Lithium Ion Batteries. *Nano Letters*: In press. (2012)

90. Y.T. Cheng and M.W. Verbrugge, Diffusion-Induced Stress, Interfacial Charge Transfer, and Criteria for Avoiding Crack Initiation of Electrode Particles. *Journal of the Electrochemical Society*, 157(4): A508-A516. (2010)

91. K.E. Aifantis and J.P. Dempsey, Stable Crack Growth in Nanostructured Li-Batteries. *Journal of Power Sources*, 143(1-2): 203-211. (2005)

92. F.Q. Yang, Criterion for insertion-induced microcracking and debonding of thin films. *Journal of Power Sources*, 196(1): 465-469. (2011)

93. K.D. Kepler, J.T. Vaughey, and M.M. Thackeray, Copper-Tin Anodes for Rechargeable Lithium Batteries: An Example of the Matrix Effect in an Intermetallic System. *Journal of Power Sources*, 81: 383-387. (1999)

94. W.H. Pu, X.M. He, J.G. Ren, C.R. Wan, and C.Y. Jiang, Electrodeposition of Sn-Cu Alloy Anodes for Lithium Batteries. *Electrochimica Acta*, 50(20): 4140-4145. (2005)

95. A.D.W. Todd, R.E. Mar, and J.R. Dahn, Combinatorial Study of Tin-Transition Metal Alloys as Negative Electrodes for Lithium-Ion Batteries. *Journal of the Electrochemical Society*, 153(10): A1998-A2005. (2006)

96. L.B. Wang, S. Kitamura, T. Sonoda, K. Obata, S. Tanase, and T. Sakai, Electroplated Sn-Zn Alloy Electrode for Li Secondary Batteries. *Journal of the Electrochemical Society*, 150(10): A1346-A1350. (2003)

97. J.J. Zhang and Y.Y. Xia, Co-Sn Alloys as Negative Electrode Materials for Rechargeable Lithium Batteries. *Journal of the Electrochemical Society*, 153(8): A1466-A1471. (2006)

98. N. Tamura, Y. Kato, A. Mikami, M. Kamino, S. Matsuta, and S. Fujitani, Study on Sn-Co Alloy Anodes for Lithium Secondary Batteries I. Amorphous System. *Journal of the Electrochemical Society*, 153(8): A1626-A1632. (2006)

99. H. Li, L.H. Shi, Q. Wang, L.Q. Chen, and X.J. Huang, Nano-Alloy Anode for Lithium Ion Batteries. *Solid State Ionics*, 148(3-4): 247-258. (2002)

100. J. Yang, M. Winter, and J.O. Besenhard, Small Particle Size Multiphase Li-Alloy Anodes for Lithium-Ion-Batteries. *Solid State Ionics*, 90(1-4): 281-287. (1996)

101. S.D. Beattie, T. Hatchard, A. Bonakdarpour, K.C. Hewitt, and J.R. Dahn, Anomolous, High-Voltage Irreversible Capacity in Tin Electrodes for Lithium Batteries. *Journal of the Electroceramical Society*, 18(8): A701-A705. (2003)

102. W. Choi, J.Y. Lee, B.H. Jung, and H.S. Lim, Microstructure and Electrochemical Properties of a Nanometer-Scale Tin Anode for Lithium Secondary Batteries. *Journal of Power Sources*, 136(1): 154-159. (2004)

103. J.W. Osenbach, J.M. DeLucca, B.D. Potteiger, A. Amin, R.L. Shook, and F.A. Baiocchi, Sn Corrosion and its Influence on Whisker Growth. *IEEE Transactions on Electronics Packaging Manufacturing*, 30(1): 23-35. (2007)

104. C.C. Chen, Y. Bisrat, Z.P. Lu, R.E. Schaak, C.G. Chao, and D.C. Lagoudas, Fabrication of Single-Crystal Tin Nanowires by Hydraulic Pressure Injection. *Nanotechnology*, 17(2): 367-374. (2006)

105. F.Q. Yang, Analysis of the Lattice Diffusion-Controlled Growth of Metallic Whiskers. *Journal of Physics D-Applied Physics*, 40(13): 4034-4038. (2007)

106. F.Q. Yang and Y. Li, Indentation-Induced Tin Whiskers on Electroplated Tin Coatings. *Journal of Applied Physics*, 104(11): 113512. (2008)

107. K.N. Tu and J.C.M. Li, Spontaneous Whisker Growth on Lead-Free Solder Finishes. *Materials Science and Engineering A-Structural Materials Properties Microstructure and Processing*, 409(1-2): 131-139. (2005)

108. B.Z. Lee and D.N. Lee, Spontaneous Growth Mechanism of Tin Whiskers. *Acta Materialia*, 46(10): 3701-3714. (1998)

109. K.N. Tu, Irreversible-Process of Spontaneous Whisker Growth in Bimetallic Cu-Sn Reactions. *Physical Review B*, 49(3): 2030-2034. (1994)

110. M. Sobiech, M. Wohlschlogel, U. Welzel, E.J. Mittemeijer, W. Hugel, A. Seekamp, W. Liu, and G.E. Ice, Local, Submicron, Strain Gradients as the Cause of Sn Whisker Growth. *Applied Physics Letters*, 94(22): 221901. (2009)

111. Y.T. Cheng, A.M. Weiner, C.A. Wong, M.P. Balogh, and M.J. Lukitsch, Stress-Induced Growth of Bismuth Nanowires. *Applied Physics Letters*, 81(17): 3248-3250. (2002)

112. Renzong Hu, Hui Liu, Meiqin Zeng, and M. Zhu, Effect of Aging Time on the Tin Film and its Anode Behavior in Lithium Ion Batteries, in *International Meeting on Lithium Batteries IMLB*. 2010: Montreal, Canada.

113. C.M. Lopez, J.T. Vaughey, and D.W. Dees, Morphological Transitions on Lithium Metal Anodes. *Journal of the Electrochemical Society*, 156(9): A726-A729. (2009)

114. C. Brissot, M. Rosso, J.N. Chazalviel, and S. Lascaud, *In situ* Concentration Cartography in the Neighborhood of Dendrites Growing in Lithium/polymer-Electrolyte/Lithium Cells. *Journal of the Electrochemical Society*, 146(12): 4393-4400. (1999)

115. F.Q. Yang and J.C.M. Li, Deformation Behavior of Tin and Some Tin Alloys. *Journal of Materials Science-Materials in Electronics*, 18(1-3): 191-210. (2007)

116. D.E. Newton, *The Chemical Elements*. 1994, New York: Franklin Watts.

117. Y.T. Cheng and M.W. Verbrugge, Evolution of Stress within a Spherical Insertion Electrode Particle under Potentiostatic and Galvanostatic Operation. *Journal of Power Sources*, 190(2): 453-460. (2009)

118. J.P. Maranchi, A.F. Hepp, A.G. Evans, N.T. Nuhfer, and P.N. Kumta, Interfacial Properties of the a-Si/Cu: Active-Inactive Thin-Film Anode System for Lithium-Ion Batteries. *Journal of the Electrochemical Society*, 153(6): A1246-A1253. (2006)

119. J. Chen, S.J. Bull, S. Roy, H. Mukaibo, H. Nara, T. Momma, T. Osaka, and Y. Shacham-Diamand, Mechanical Analysis and *in situ* Structural and Morphological Evaluation of Ni-Sn Alloy Anodes for Li Ion Batteries. *Journal of Physics D-Applied Physics*, 41(2). (2008)

120. M. Kodaira, M. Seido, and G. Sasaki, Deformation Behavior of Copper Foil Collectors with Ni_3Sn_4 Film During the Charge-Discharge of Lithium Ion Secondary Cells on the Basis of an Optical Cantilever Method. *Electrochemistry*, 78(5): 409-412. (2010)

121. J. Kim, D. Inns, and D.K. Sadana, Investigation on Critical Failure Thickness of Hydrogenated/Nonhydrogenated Amorphous Silicon Films. *Journal of Applied Physics*, 107(7). (2010)

122. S. Nag, S. Sinha, S. Sadhukhan, T. Dutta, and S. Tarafdar, Crack Patterns in Desiccating Clay-Polymer Mixtures with Varying Composition. *Journal of Physics-Condensed Matter*, 22(1): 015402. (2010)

123. T. Ishii and M. Matsushita, Fragmentation of Long Thin Glass Rods. *Journal of the Physical Society of Japan*, 61(10): 3474-3477. (1992)

124. H.N. Iben and J.F. O'Brien, Generating Surface Crack Patterns. *Graphical Models*, 71(1-6): 198-208. (2009)

125. K.-T. Leung and Z. Neda, Pattern Formation and Selection in Quasistatic Fracture. *Physical Review Letters*, 85(3): 662-665. (2000)

126. G. Valette, S. Prevost, L. Lucas, and J. Leonard, A Dynamic Model of Cracks Development Based on a 3D Discrete Shrinkage Volume Propagation. *Computer Graphics Forum*, 27(1): 47-62. (2008)

127. S. Sadhukhan, S.R. Majumder, D. Mal, T. Dutta, and S. Tarafdar, Desiccation Cracks on Different Substrates: Simulation by a Spring Network Model. *Journal of Physics-Condensed Matter*, 19(35). (2007)

128. M. Müller and M. Gross, Interactive virtual materials, in *Proceedings of Graphics Interface*. 2004.

129. J.F.O'Brien, A. Bargteil, and J. Hodgins, Graphical modeling and animation of ductile fracture, in *Proceedings of ACM SIGGRAPH*. 2002.

130. A. Timmons and J.R. Dahn, Isotropic Volume Expansion of Particles of Amorphous Metallic Alloys in Composite Electrodes for Li-Ion Batteries. *Journal of Electroceramical Society*, 154(5): A444-A448. (2007)

131. Y.T. Cheng and M.W. Verbrugge, Application of Hasselman's Crack Propagation Model to Insertion Electrodes. *Electrochemical and Solid State Letters*, 13(9): A128-A131. (2010)

132. H. Ma, F.Y. Cheng, J. Chen, J.Z. Zhao, C.S. Li, Z.L. Tao, and J. Liang, Nest-Like Silicon Nanospheres for High-Capacity Lithium Storage. *Advanced Materials*, 19(22): 4067-4070. (2007)

133. W.R. Liu, Z.Z. Guo, W.S. Young, D.T. Shieh, H.C. Wu, M.H. Yang, and N.L. Wu, Effect of Electrode Structure on Performance of Si Anode in Li-Ion Batteries: Si Particle Size and Conductive Additive. *Journal of Power Sources*, 140(1): 139-144. (2005)

134. R. Huang and J. Zhu, Silicon Nanowire Array Films as Advanced Anode Materials for Lithium-Ion Batteries. *Materials Chemistry and Physics*, 121(3): 519-522. (2010)

135. Q.Y. Li and K.S. Kim, Micromechanics of Friction: Effects of Nanometre-Scale Roughness. *Proceedings of the Royal Society A - Mathematical Physical and Engineering Sciences*, 464(2093): 1319-1343. (2008)

136. D. Gross and T. Seelig, *Fracture Mechanics*. 2006, New York: Springer.

137. V.B. Shenoy, P. Johari, and Y. Qi, Elastic Softening of Amorphous and Crystalline Li-Si Phases with Increasing Li Concentration: a First-Principles Study. *Journal of Power Sources*, 195(19): 6825-6830. (2010)

138. Y.Y. Xia, T. Sakai, T. Fujieda, M. Wada, and H. Yoshinaga, Flake Cu-Sn alloys as Negative Electrode Materials for Rechargeable Lithium Batteries. *Journal of the Electrochemical Society*, 148(5): A471-A481. (2001)

139. A.D.W. Todd, R.E. Mar, and J.R. Dahn, Tin-Transition Metal-Carbon Systems for Lithium-Ion Battery Negative Electrodes. *Journal of the Electrochemical Society*, 154(6): A597-A604. (2007)

140. J. Hassoun, S. Panero, and B. Scrosati, Electrodeposited Ni-Sn Intermetallic Electrodes for Advanced Lithium Ion Batteries. *Journal of Power Sources*, 160(2): 1336-1341. (2006)

141. G. Armstrong, A.R. Armstrong, P.G. Bruce, P. Reale, and B. Scrosati, TiO_2(B) Nanowires as An Improved Anode Material for Lithium-Ion Batteries Containing

$LiFePO_4$ or $LiNi_{0.5}Mn_{1.5}O_4$ Cathodes and A Polymer Electrolyte. *Advanced Materials*, 18(19): 2597-2600. (2006)

142. H.C. Shin, J. Dong, and M.L. Liu, Porous Tin Oxides Prepared using an Anodic Oxidation Process. *Advanced Materials*, 16(3): 237-240. (2004)

143. S.J. Bao, Q.L. Bao, C.M. Li, and Z.L. Dong, Novel Porous Anatase TiO_2 Nanorods and their High Lithium Electroactivity. *Electrochemistry Communications*, 9(5): 1233-1238. (2007)

144. C.J. Wen and R.A. Huggins, Electrochemical Investigation of the Lithium-Gallium System. *Journal of the Electrochemical Society*, 128(8): 1636-1641. (1981)

145. J. Saint, M. Morcrette, D. Larcher, and J.M. Tarascon, Exploring the Li-Ga Room Temperature Phase Diagram and the Electrochemical Performances of the Li_xGa_y Alloys vs. Li. *Solid State Ionics*, 176(1-2): 189-197. (2005)

146. K.T. Lee, Y.S. Jung, J.Y. Kwon, J.H. Kim, and S.M. Oh, Role of Electrochemically Driven Cu Nanograins in $CuGa_2$ Electrode. *Chemistry of Materials*, 20(2): 447-453. (2008)

147. K.T. Lee, Y.S. Jung, T. Kim, C.H. Kim, J.H. Kim, J.Y. Kwon, and S.M. Oh, Liquid Gallium Electrode Confined in Porous Carbon Matrix as Anode for Lithium Secondary Batteries. *Electrochemical and Solid State Letters*, 11(3): A21-A24. (2008)

148. B. Predel, *Group IV Physical Chemistry - Phase Equilibria, Crystallographic and Thermodynamic Data of Binary Alloys*. Electronic Materials and Semiconductors. Vol. 5. 1998: Springer.

149. C.J. Wen, C. Ho, B.A. Boukamp, I.D. Raistrick, W. Weppner, and R.A. Higgins, Use of Electrochemical Methods to Determine Chemical-Diffusion Coefficients in Alloys: Application to 'LiAl'. *International Metals Reviews*, 5: 253-268. (1981)

150. C.J. Wen, B.A. Boukamp, R.A. Huggins, and W. Weppner, Thermodynamic and Mass-Transport Properties of LiAl. *Journal of the Electrochemical Society*, 126(12): 2258-2266. (1979)

151. M.D. Levi and D. Aurbach, Diffusion Coefficients of Lithium Ions during Intercalation into Graphite Derived from the Simultaneous Measurements and Modeling of Electrochemical Impedance and Potentiostatic Intermittent Titration Characteristics of Thin Graphite Electrodes. *Journal of Physical Chemistry B*, 101(23): 4641-4647. (1997)

152. M.D. Levi, E. Markevich, and A. Aurbach, The Effect of Slow Interfacial Kinetics on the Chronoamperometric Response of Composite Lithiated Graphite Electrodes and on the Calculation of the Chemical Diffusion Coefficient of Li Ions in Graphite. *Journal of Physical Chemistry B*, 109(15): 7420-7427. (2005)

153. S. Patoux and C. Masquelier, Chemical and Electrochemical Insertion of Iithium into Two Allotropic Varieties of $NbPO_5$. *Chemistry of Materials*, 14(5): 2334-2341. (2002)

154. F. Artuso, F. Decker, A. Krasilnikova, M. Liberatore, A. Lourenco, E. Masetti, A. Pennisi, and F. Simone, Indium-Vanadium Oxides Deposited by Radio Frequency Sputtering: New Thin Film Transparent Materials for Li-Insertion Electrochemical Devices. *Chemistry of Materials*, 14(2): 636-642. (2002)

155. C. Delacourt, P. Poizot, M. Morcrette, J.M. Tarascon, and C. Masquelier, One-Step Low-Temperature Route for the Preparation of Electrochemically Active $LiMnPO_4$ Powders. *Chemistry of Materials*, 16(1): 93-99. (2004)

156. J. Xie, N. Imanishi, T. Zhang, A. Hirano, Y. Takeda, and O. Yamamoto, Li-ion Diffusion Kinetics in $LiFePO_4$ Thin Film Prepared by Radio Frequency Magnetron Sputtering. *Electrochimica Acta*, 54(20): 4631-4637. (2009)

157. Y.I. Jang, B.J. Neudecker, and N.J. Dudney, Lithium Diffusion in $LixCoO_2$ ($0.45 < x < 0.7$) Intercalation Cathodes. *Electrochemical and Solid State Letters*, 4(6): A74-A77. (2001)

158. M.D. Levi, G. Salitra, B. Markovsky, H. Teller, D. Aurbach, U. Heider, and L. Heider, Solid-State Electrochemical Kinetics of Li-Ion Intercalation into $Li_{1-x}CoO_2$: Simultaneous Application of Electroanalytical Techniques SSCV, PITT, and EIS. *Journal of the Electrochemical Society*, 146(4): 1279-1289. (1999)

159. C. Delacourt, M. Ati, and J.M. Tarascon, Measurement of Lithium Diffusion Coefficient in LiyFeSO4F. *Journal of the Electrochemical Society*, 158(6): A741-A749. (2011)

160. E. Markevich, M.D. Levi, and D. Aurbach, Comparison between Potentiostatic and Galvanostatic Intermittent Titration Techniques for Determination of Chemical Diffusion Coefficients in Ion-Insertion Electrodes. *Journal of Electroanalytical Chemistry*, 580(2): 231-237. (2005)

161. M.D. Levi, C. Wang, and D. Aurbach, Two Parallel Diffusion Paths Model for Interpretation of PITT and EIS Responses from Non-Uniform Intercalation Electrodes. *Journal of Electroanalytical Chemistry*, 561(1-2): 1-11. (2004)

162. M.D. Levi, E. Markevich, and D. Aurbach, Comparison between Cottrell Diffusion and Moving Boundary Models for Determination of the Chemical

Diffusion Coefficients in Ion-Insertion Electrodes. *Electrochimica Acta*, 51(1): 98-110. (2005)

163. C. Montella, Discussion of the Potential Step Method for the Determination of the Diffusion Coefficients of Guest Species in Host Materials Part I. Influence of Charge Transfer Kinetics and Ohmic Potential Drop. *Journal of Electroanalytical Chemistry*, 518(2): 61-83. (2002)

164. M.A. Vorotyntsev, M.D. Levi, and D. Aurbach, Spatially Limited Diffusion Coupled with Ohmic Potential Drop and/or Slow Interfacial Exchange: A New Method to Determine the Diffusion Time Constant and External Resistance from Potential Step (PITT) Experiments. *Journal of Electroanalytical Chemistry*, 572(2): 299-307. (2004)

165. M.D. Levi, R. Demadrille, A. Pron, M.A. Vorotyntsev, Y. Gofer, and D. Aurbach, Application of a Novel Refinement Method for Accurate Determination of Chemical Diffusion Coefficients in Electroactive Materials by Potential Step Technique. *Journal of the Electrochemical Society*, 152(2): E61-E67. (2005)

166. A.V. Churikov, A.V. Ivanishchev, I.A. Ivanishcheva, V.O. Sycheva, N.R. Khasanova, and E.V. Antipov, Determination of Lithium Diffusion Coefficient in $LiFePO_4$ Electrode by Galvanostatic and Potentiostatic Intermittent Titration Techniques. *Electrochimica Acta*, 55(8): 2939-2950. (2010)

167. J. Newman and K.E. Thomas-Alyea, *Electrochemical Systems*. 3rd Edition. 2004, Hoboken: Wiley.

168. A.J. Bard and L.R. Faulkner, *Electrochemical Methods & Applications*. 2nd Edition. 2000, New York: Wiley.

169. J.S. Chen, J.P. Diard, R. Durand, and C. Montella, Hydrogen insertion reaction with restricted diffusion .1. Potential step-EIS theory and review for the direct insertion mechanism. *Journal of Electroanalytical Chemistry*, 406(1-2): 1-13. (1996)

170. D.R. Baker and M.W. Verbrugge, An Analytic Solution for the Microdisk Electrode and Its Use in the Evaluation of Charge-Transfer Rate Constants. *Journal of the Electrochemical Society*, 137(12): 3836-3845. (1990)

171. M.W. Verbrugge and B.J. Koch, Modeling lithium intercalation of single-fiber carbon microelectrodes. *Journal of the Electrochemical Society*, 143(2): 600-608. (1996)

172. M.W. Verbrugge, D.R. Baker, and J. Newman, Dependent-Variable Transformation for the Treatment of Diffusion, Migration, and Homogeneous

Reactions - Application to a Corroding Pit. *Journal of the Electrochemical Society*, 140(9): 2530-2537. (1993)

173. H.S. Carslaw and J.C. Jaeger, *Conduction of Heat in Solids*. Second Edition. 1959, New York: Oxford University Press.

174. J. Crank, *The Mathematics of Diffusion*. 1975, London: Oxford University Press.

175. M.W. Verbrugge and B.J. Koch, Electrochemical Analysis of Lithiated Graphite Anodes. *Journal of the Electrochemical Society*, 150(3): A374-A384. (2003)

176. C. Montella, Apparent diffusion coefficient of intercalated species measured with PITT - A simple formulation. *Electrochimica Acta*, 51(15): 3102-3111. (2006)

177. J.C. Li, A.K. Dozier, Y.C. Li, F.Q. Yang, and Y.T. Cheng, Crack Pattern Formation in Thin Film Lithium-Ion Battery Electrodes. *Journal of the Electrochemical Society*, 158(6): A689-A694. (2011)

178. J. Xie, N. Imanishi, T. Zhang, A. Hirano, Y. Takeda, and O. Yamamoto, Li-Ion Diffusion in Amorphous Si Films Prepared by RF Magnetron Sputtering: A Comparison of Using Liquid and Polymer Electrolytes. *Materials Chemistry and Physics*, 120(2-3): 421-425. (2010)

179. H. Xia, S.B. Tang, and L. Lu, Properties of Amorphous Si Thin Film Anodes Prepared by Pulsed Laser Deposition. *Materials Research Bulletin*, 42(7): 1301-1309. (2007)

180. T.L. Kulova, A.M. Skundin, Y.V. Pleskov, E.I. Terukov, and O.I. Kon'kov, Lithium Insertion into Amorphous Silicon Thin-Film Electrodes. *Journal of Electroanalytical Chemistry*, 600(1): 217-225. (2007)

181. M.W. Verbrugge and B.J. Koch, Electrochemistry of Intercalation Materials - Charge-Transfer Reaction and Intercalate Diffusion in Porous Electrodes. *Journal of the Electrochemical Society*, 146(3): 833-839. (1999)

182. W.C. West, J. Soler, M.C. Smart, B.V. Ratnakumar, S. Firdosy, V. Ravi, M.S. Anderson, J. Hrbacek, E.S. Lee, and A. Manthiram, Electrochemical Behavior of Layered Solid Solution Li(2)MnO(3)-LiMO(2) (M = Ni, Mn, Co) Li-Ion Cathodes with and without Alumina Coatings. *Journal of the Electrochemical Society*, 158(8): A883-A889. (2011)

183. J. Xie, N. Imanishi, T. Zhang, A. Hirano, Y. Takeda, and Y. Yamamoto, Li-ion diffusion kinetics in LiCoPO(4) thin films deposited on NASICON-type glass ceramic electrolytes by magnetron sputtering. *Journal of Power Sources*, 192(2): 689-692. (2009)

184. M. Jiang, B. Key, Y.S. Meng, and C.P. Grey, Electrochemical and Structural Study of the Layered, "Li-Excess" Lithium-Ion Battery Electrode Material Li Li(1/9)Ni(1/3)Mn(5/9) O(2). *Chemistry of Materials*, 21(13): 2733-2745. (2009)

185. M.C. Yang, B. Xu, J.H. Cheng, C.J. Pan, B.J. Hwang, and Y.S. Meng, Electronic, Structural, and Electrochemical Properties of LiNi(x)Cu(y)Mn(2-x-y)O(4) ($0 < x < 0.5$, $0 < y < 0.5$) High-Voltage Spinel Materials. *Chemistry of Materials*, 23(11): 2832-2841. (2011)

186. E. Deiss, Spurious potential dependence of diffusion coefficients in Li+ insertion electrodes measured with PITT. *Electrochimica Acta*, 47(25): 4027-4034. (2002)

187. J. Li, X. Xiao, F. Yang, M.W. Verbrugge, and Y.-T. Cheng, Potentiostatic Intermittent Titration Technique for Electrodes Governed by Diffusion and Interfacial Reaction. *Journal of Physical Chemistry C*, 116(1): 1472-1478. (2012)

188. M.W. Verbrugge, B.J. Koch, and E.W. Schneider, Mass transport in lithium-battery solvents. *Journal of Applied Electrochemistry*, 30(3): 269-275. (2000)

189. H. Yang, H.J. Bang, and J. Prakash, Evaluation of electrochemical interface area and lithium diffusion coefficient for a composite graphite anode. *Journal of the Electrochemical Society*, 151(8): A1247-A1250. (2004)

190. M.D. Levi, E.A. Levi, and D. Aurbach, The Mechanism of Lithium Intercalation in Graphite Film Electrodes in Aprotic Media. 2. Potentiostatic Intermittent Titration and *in situ* XRD Studies of the Solid-State Ionic Diffusion. *Journal of Electroanalytical Chemistry*, 421(1-2): 89-97. (1997)

191. D.R. Baker and M.W. Verbrugge, Intercalate Diffusion in Multiphase Electrode Materials and Application to Lithiated Graphite. *Journal of The Electrochemical Society*: in press. (2012)

Vita

Juchuan Li was born on January 23rd, 1985 in Xiaxian County, Shanxi Province, P. R. China.

EDUCATION

M.Eng., MSE, Tsinghua University, Beijing, 2007.
B.Eng., MSE, University of Science and Technology Beijing, Beijing, 2005

PROFESSIONAL AFFILIATIONS

Student Member, MRS, 2009-present
Student Member, ECS, 2010-present
Student Member, ASM International, 2011-present

AWARDS RECEIVED

Travel Grant for 220th ECS meeting, ECS Battery Division, Boston, MA, 10/2011
Travel Grant for 219th ECS meeting, ECS Battery Division, Montréal, Canada, 05/2011
Graduate Student Travel Scholarship, UK, 05/2011
First Place in Poster Category, UK CeNSE Annual Nanotechnology Contest, 12/2010
Graduate Student Travel Scholarship, UK, 04/2010
Excellent Final Thesis Award, USTB, 2005

PROFESSIONAL SERVICE

Session Co-Chair, "Microstructure, Mechanisms, and Modeling of Battery Materials", 219th ECS Meeting, Montréal, Canada, 05/2011

Secretary, MRS University of Kentucky Chapter, 2010-2011

PATENTS

1. Rutooj D. Deshpande, Juchuan Li, and Yang-Tse Cheng. "Using Liquid Metal as Lithium-Ion Battery Electrodes", provisional patent filed, 04/2011.

PUBLICATIONS

1. Qing Liu Wu, Juchuan Li, Rutooj D. Deshpande, Navaladian Subramanian, Stephen E. Rankin, Fuqian Yang, and Yang-Tse Cheng. "Aligned TiO_2 Nanotube Arrays as Durable Lithium-Ion Battery Negative Electrodes", submitted to *J. Phys. Chem. C*. (Joint first-author with Q.L.W. and R.D.D.)

2. Juchuan Li, Xingcheng Xiao, Fuqian Yang, Mark W. Verbrugge, and Yang-Tse Cheng. "Potentiostatic Intermittent Titration Technique (PITT) for Spherical Particles with Finite Interfacial Kinetics", submitted to *Electrochimica Acta*.

3. Rituraj Borgohain, Juchuan Li, John P. Selegue, and Yang-Tse Cheng. "Synthesis and Electrochemical Study of Ruthenium Oxide-Modified Carbon Nano-Onions for High-Performance Supercapacitor Electrodes", submitted to *J. Phys. Chem. C*..

4. Juchuan Li, Xingcheng Xiao, Fuqian Yang, Mark W. Verbrugge, and Yang-Tse Cheng. "Potentiostatic Intermittent Titration Technique for Electrodes Governed by Diffusion and Interfacial Reaction", *J. Phys. Chem. C*., 116 (1): 1472-1478 (2012).

5. Mark W. Verbrugge, Rutooj D. Deshpande, Juchuan Li, and Yang-Tse Cheng. "The Search for High Cycle Life, High Capacity, Self Healing Negative Electrodes for Lithium Ion Batteries and a Potential Solution Based on Lithiated Gallium", *2011 MRS Spring Meeting Proceedings*, in press.

6. Rutooj D. Deshpande, Juchuan Li, Yang-Tse Cheng, and Mark W Verbrugge. "Liquid Metal Alloys as Self-Healing Negative Electrodes for Lithium Ion Batteries", *J. Electrochem. Soc.*, 158 (8): A845-A849 (2011).

7. Juchuan Li, Alan K. Dozier, Yunchao Li, Fuqian Yang, and Yang-Tse Cheng. "Cracking Pattern Formation in Thin Film Lithium-Ion Battery Electrodes", *J. Electrochem. Soc.*, 158 (6): A689-A694 (2011).

8. Juchuan Li, Fuqian Yang, Jia Ye, and Yang-Tse Cheng. "Whisker Formation on a Thin Film Tin Lithium-Ion Battery Anode", *J. Power Sources*, 196 (3): 1474-1477 (2011).

9. Ju-Chuan Li, Jia-Lin Gu, and Chong-Lin Jia. "Effect of Heating Temperature on Microstructure and Properties of Fe-Cr-Co Martensite Heat-Resistant Steel", *Heat Treatment of Metals*, 32 (9): 1-4 (2007).

CONFERENCE PRESENTATIONS

1. Oral presentation, "Aligned TiO_2 Nanotubes as Long Durability Anodes for Lithium-Ion Batteries", *MS&T'11*, Columbus, OH, 2011.

2. Oral presentation, "Liquid Metal Alloys as Self-Healing Negative Electrodes for Lithium Ion Batteries", *220th ECS Meeting*, Boston, MA, 10/2011.

3. Oral presentation, "Cracking Pattern Formation in Thin Film Lithium-Ion Battery Electrodes", *219th ECS Meeting*, Montréal, Canada, 2011.

4. Poster, "Cracking and Whisker Formation in Thin Film Lithium-Ion Battery Anodes", *2011 KY Renewable Energy and Energy Efficiency Workshop*, Louisville, KY, 2011.

5. Poster, "Whisker Formation on a Thin Film Tin Lithium-Ion Battery Anode", *Symposium on Energy Storage beyond Lithium Ion: Materials Perspectives*, Oak Ridge, TN, 2010.

6. Oral presentation, "*In-situ* Mass and Stress Measurement during Sn Electrodeposition using an Electrochemical Double Quartz Crystal Microbalance (E-DQCM) Technique", *217th ECS Meeting*, Vancouver, Canada, 2010.

7. Poster, "Tin (Sn) Whiskers and Nanowires as Negative Electrodes for Li-Ion Batteries", *2009 MRS Fall Meeting*. Boston, MA, 2009.

8. Poster, "Stress-Induced Sn Whiskers Growth", *5th Kentucky Innovation and Entrepreneurship Conference*, Louisville, KY, 2009.